Istituto Nazionale di Fisica Nucleare
LABORATORI NAZIONALI DI FRASCATI

FRASCATI PHYSICS SERIES

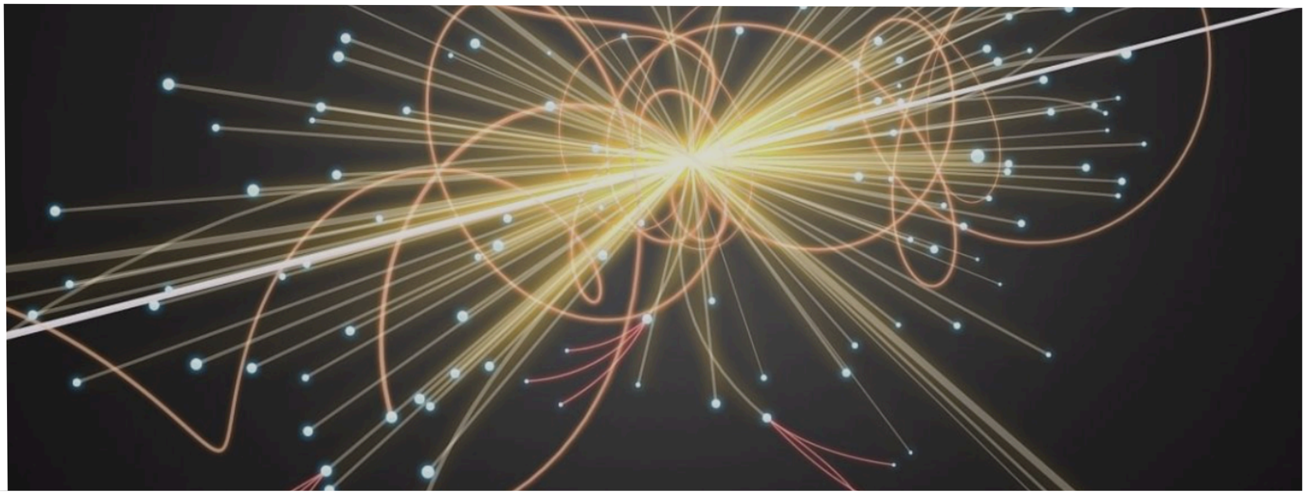

Eighth Young Researchers' Workshop

Physics Challenges in the LHC Era

2024

EDITORS:

F. Arias Aragón, E. Bagnaschi, G. Corcella, E. Nardi,
A. Paoloni, S. Pisano, D. Sengupta, M. Testa

FRASCATI PHYSICS SERIES

Series Editor
Antonella Antonelli

Technical Editor
Lia Sabatini

Cover by Elisa Santinelli

Volume LXXVI

Istituto Nazionale di Fisica Nucleare – Laboratori Nazionali di Frascati
Divisione Ricerca
Ufficio Biblioteca e Pubblicazioni Scientifiche
P.O. Box 13, I-00044 Frascati Roma Italy
email: library@lists.lnf.infn.it

ISBN 978-88-86409-78-0

8th Young Researchers' Workshop
Physics Challenges in the LHC Era
2024

CONTENTS

PREFACE

The Eighth Young Researchers' Workshop 'Physics Challenges in the LHC Era' took place on May 13th and 17th, 2024, as part of the program of the XXI edition of the Spring School 'Bruno Touschek' in Nuclear, Subnuclear and Astroparticle Physics, which took place at INFN, Laboratori Nazionali di Frascati (LNF).

Such workshops began in 2009 and have now become a regular appointment which gives graduate students in theoretical and experimental physics a chance to present their thesis work in front of other young fellows, as well as senior lecturers and spring school organizers. The environment has always been pretty informal, with open discussions which keep going even during the social events.

In particular, the 2024 eighth edition featured talks of very high standards. We had experimental presentations on calorimeters for the Mu2e experiment and future muon collider, searches for magnetic monopoles, leptoquarks and the X17 particle. Furthermore, we heard of new forces between the third quark generation, jets in high-energy collisions, investigation of multi-top events with machine learning algorithms, CP properties and couplings of the Higgs boson, double-Higgs production, novel detectors for the LHC high-luminosity phase, exploration of kaonic atoms, nuclear astrophysics reactions. The theory talks were instead on new scalars in W-pair production at LHC, models for pentaquarks, nucleon electromagnetic form factors, skyrmion-based logic gates, metrics in Lyra's geometry.

The present volume collects summaries of most of the talks and it is also a unique opportunity for the school participants to have a peer-reviewed publication, which is often the first one in their careers.

Having said this, let me warmly thank all co-organizers, the school secretary, the lecturers, the discussion leaders and, above all, the fellows who attended the lectures, gave outstanding presentations and livened up the XXI 'Bruno Touschek' Spring School.

Frascati, December 2, 2024

Gennaro Corcella
(Chair of the Spring School and of the 8th Young Researchers' Workshop)

Frascati Physics Series Vol. 76 (2024)
8th young researchers' workshop 'Physics Challenges in the LHC Era'
May 13 and 16, 2024

CHARACTERIZATION AND IRRADIATION STUDY FOR THE CRILIN ELECTROMAGNETIC CALORIMETER

Vittoria Ludovica Ciccarella
INFN, Laboratori Nazionali di Frascati, Via E. Fermi 54, 00044, Frascati, Italy

Abstract

The Crilin calorimeter is an innovative calorimetric system, specifically designed and optimized for use in the environment of a future Muon Collider. It employs a unique semi-homogeneous architecture, consisting of stackable and interchangeable matrices of lead fluoride (PbF_2) crystals, which serve as high density Cherenkov radiators. These crystals are read out by surface-mount UV-extended Silicon Photomultipliers (SiPMs). This design enables the discrimination of beam-induced backgrounds (BIB) present at a Muon Collider from genuine physics events by leveraging the excellent time resolution (below 50 ps), longitudinal segmentation, and high granularity. The paper describes Crilin and its timing performance for its latest prototype, Proto-1, based on a beam test conducted at CERN-H2 with 120 GeV electrons. Additionally, the results from a recent beam test at the LNF Beam Test Facility with 450 MeV electrons are presented, focusing on measurements of light yield losses due to γ-ray irradiation.

1 Introduction

The Muon Collider 1), proposed by the International Muon Collider Collaboration (IMCC), is a next-generation particle accelerator aimed at exploring high-energy physics. By colliding muons, it offers advantages over traditional electron-positron and hadron colliders. Unlike protons, muons are point-like particles, so there is no presence of quantum chromodynamics backgrounds; also, their larger mass implies that there are less synchrotron radiation losses compared to the electrons case. This enables higher collision energies in a compact design, ideal for probing new energy scales. A multi-TeV Muon Collider would enable the study of Higgs interactions, dark matter, and allow for unprecedented precision testing of the Standard Model.

Despite these promising prospects, the Muon Collider faces several challenges. In terms of detectors, the primary concern is beam-induced backgrounds (BIB), which consist of secondary and tertiary particles produced by interactions between muon decay products and machine elements. Specifically, for each bunch crossing, the electromagnetic calorimeter (ECAL) experiences a BIB flux of 300 particles per cm^2, primarily consisting of photons (96%) with an average energy of 1.7 MeV, and neutrons (4%). This background not only affects the detector's energy resolution but, over years of operation, can cause damage to the ECAL itself. A FLUKA simulation at $\sqrt{s} = 1.5$ TeV $^{2)}$ estimated the Total Ionizing Dose (TID) and neutron fluence levels across the detector interface, predicting a yearly neutron fluence of 10^{14} n_{1MeV}/cm^2 and a TID of 1 kGy/year for the ECAL barrel region.

A CALICE-like tungsten-silicon (W-Si) sampling calorimeter $^{3)}$ was initially considered as the baseline ECAL design, however this technology, though beneficial, is complex and costly. This paper presents an alternative: the Crilin electromagnetic calorimeter $^{4)}$, featuring a longitudinally-segmented, semi-homogeneous design based on PbF_2 Cherenkov crystals read out by UV-extended SiPMs. This design allows for achieving fine granularity (with $1{\times}1$ cm^2 cells), excellent timing (below 50 ps), good pileup capability, and improved radiation resistance.

2 Crilin Calorimeter Design and Performance

The Crilin calorimeter employs a modular architecture consisting of stackable and interchangeable submodules, composed of matrices of high density crystals. Each crystal is independently read out by two electronics channels, consisting of a series of two UV-extended surface mount SiPMs.

This semi-homogeneous design combines the benefits of homogeneous calorimeters, particularly their improved energy resolution, with the addition of longitudinal segmentation and greater flexibility.

2.1 Design Features

In order to meet the Muon Collider's requirements, Crilin needs to achieve a timing resolution of under 100 ps. This is crucial for separating fake showers caused by BIB from actual physics signals, for which the time of arrival on the ECAL surface is synchronous with respect to bunch crossing. Its fine granularity, with a cell size of $10{\times}10$ mm^2, helps separate the energy deposited by BIB from that deposited by high-energy particles by reducing the number of hits in each cell. The overall design includes five layers, each 45 mm long (comprising 40 mm crystals and 5 mm for the readout), providing longitudinal segmentation that is essential for identifying and rejecting fake showers caused by BIB.

In order to have a compact geometry and to achieve fast light response, the design employs dense Cherenkov radiators, i.e. PbF_2 $^{5)}$, or alternatively $PbWO_4$-UF $^{6)}$ scintillating crystals. These materials have shown good radiation resistance, with no significant losses in transmittance after exposure to TID of up to 350 kGy (PbF_2) and 2 MGy ($PbWO_4$-UF) $^{7)}$. Additionally, the chosen SiPM model (Hamamatsu S14160-3010PS, 10 μm pixel size) has been validated for TID up to 10 kGy and neutron fluence up to 10^{14} n_{1MeVeq}/cm^2 $^{7)}$.

Compared to the 40 layers found in a W-Si calorimeter, Crilin's design is expected to utilize just five layers: this drastically reduces the number of readout channels and overall costs by about 90%. The significant reduction in complexity and expense, along with its design flexibility, makes Crilin an appealing alternative for use in future collider experiments.

2.2 Performance Evaluation

The Crilin design has been extensively tested through simulations and experiments, demonstrating highly promising performances.

Proto-1, which consists of two layers of 3×3 crystal matrices with 36 readout channels in total, showed excellent timing resolution and strong agreement with Monte Carlo simulations in terms of energy deposition. For research and development purposes, Proto-1 tested two different methods of connecting the readout channels for each crystal: in the first layer, the SiPMs were connected in series, and in the second layer, they were connected in parallel. Both layers were read out using custom Front End Electronics. In August 2023, the timing performance of Proto-1 was evaluated at CERN's SPS H2 beamline using a 120 GeV electron beam. The time differences between the two channels of the same crystal were measured, focusing on the central crystal - which experiences the highest energy deposits - for each layer. For both the series and parallel connections (fig.1), the time resolution was less than 40 ps for energy deposits exceeding 1 GeV, demonstrating performance well within the Muon Collider's stringent requirements.

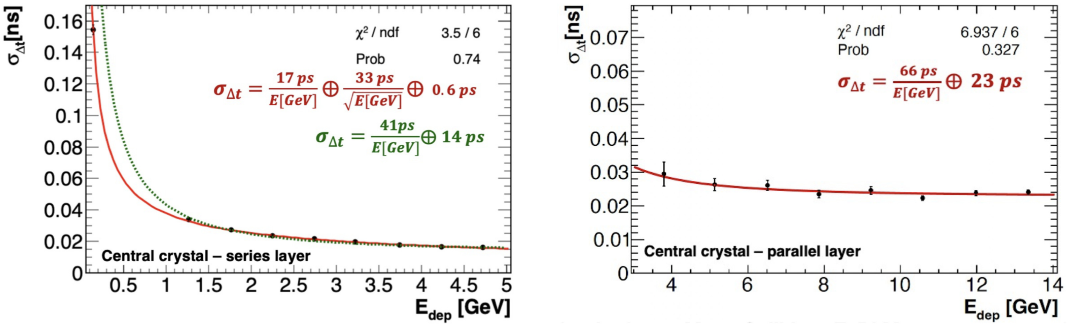

Figure 1: *Proto-1 time resolution as a function of the energy deposit in the most energetic crystal of the layer, for the series read-out module (left panel) and the parallel read-out module (right panel). For the series layer, a time resolution measurement with a 450 MeV electron beam was added and included in the solid-red line fit.*

2.3 Radiation Resistance Evaluation

In April 2024 a final test beam on Proto-1 was performed at the Frascati Beam Test Facility (BTF), in order to observe light yield loss due to exposure to high levels of ionising γ-ray radiation. The chosen TID of 80 kGy corresponds to about eight times the total expected ionising dose for the full duration of the Muon Collider experiment. The choice of such a high radiation rate was made in order to test the limits of the Crilin technology within a large safety margin.

The BTF 450 MeV electron beam (with particle multiplicity per bunch set to 1) was fired on each crystal of the series layer, before and after irradiation from a ^{60}Co source, studying the light response in terms of charge. Crystals were individually wrapped in a reflective material (both Teflon and Mylar were tested). The experimental steps are reported in tab.1.

The light yield loss was evaluated by looking at the variation in charge and number of photoelectrons:

$$N_{pe} = \frac{Q}{e \cdot G_{FEE} \cdot G_{SiPMs}}, \tag{1}$$

where e is the fundamental charge and G_{FEE} and G_{SiPMs} are the gain of the Front End Electronics and the SiPMs, respectively. The results in terms of N$_{pe}$ variation are summarized in fig.2.

Table 1: *Beam test experimentation steps for radiation resistance evaluation. For each of these steps, the charge response for each crystal was evaluated.*

Step	Wrapping	TID on PbF_2 [kGy]	TID on SiPMs [kGy]
I	Teflon	-	-
II	Teflon	80	80
III	Mylar	-	80
IV	Mylar	10	90
V	Mylar	80	160

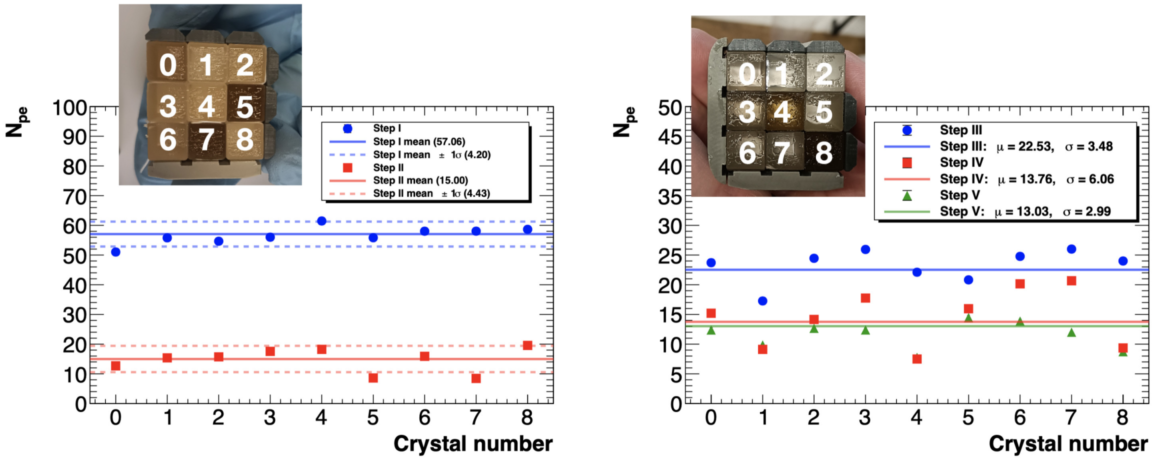

Figure 2: *Left panel: number of photo-electrons estimated for each crystal in the runs with Teflon wrapping (steps I and II). Right panel: number of photo-electrons estimated for each crystal in the runs with Mylar wrapping (steps III, IV and V). The* μ *and* σ *of the distributions were obtained by a Gaussian fit of the data points. For both cases, a picture of the crystal matrix after the test was included to show the visible transmittance loss and the crystal enumeration choice.*

In addition to demonstrating adequate operation at lower energies after exposure to extreme TID, this test revealed several noteworthy characteristics of the prototype's components. One key finding was the significant variation in the crystals' response to TID, despite the manufacturer's claim of using high-purity ($> 99.9\%$) PbF_2 powders in the crystal growth process. Additionally, the Teflon wrapping around the crystals showed signs of damage, becoming brittle over time, which led to the decision to switch to Mylar wrapping, even if it is less effective at reflecting UV light produced by Cherenkov radiation. Lastly, the SiPM dark current increased substantially with the absorbed radiation dose, as illustrated in fig.3, indicating that the radiation had a non negligible effect on the SiPMs' performance.

Further testing is required to gain a clearer understanding of these effects, which cannot be only attributed to the crystals' transmittance loss. Future irradiation sessions will involve closely monitoring the crystal-SiPM systems and the SiPMs individually using a blue laser. This approach will help to distinguish between two key factors: the Photon Detection Efficiency degradation in the SiPMs and the reduction in transmittance through the crystals. By isolating these contributions, the tests aim to better identify the root causes of performance decline and determine how each component is affected by radiation.

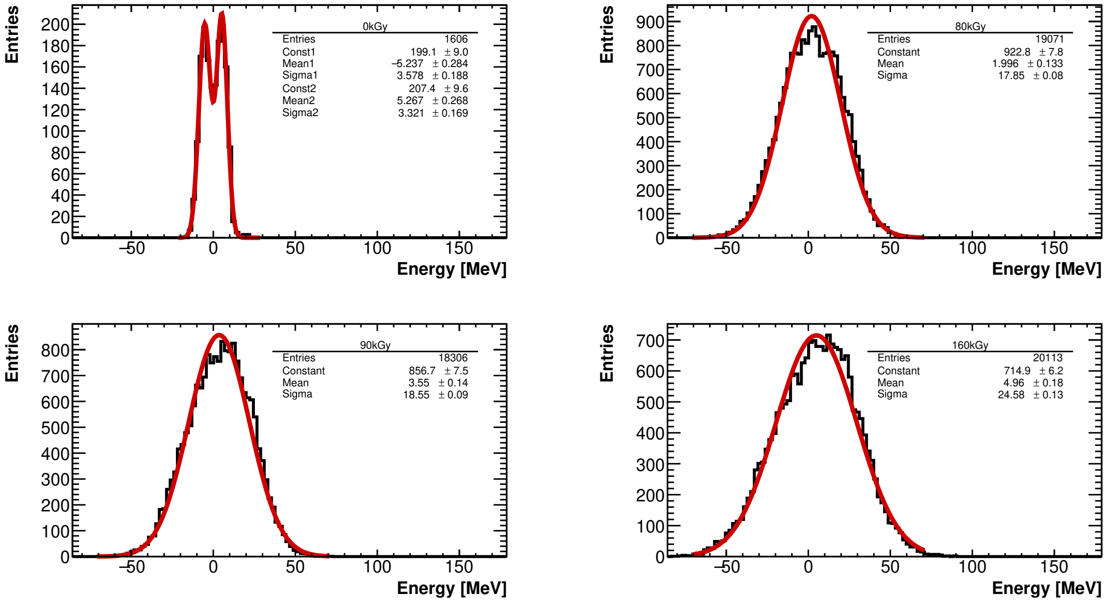

Figure 3: *SiPMs pedestals for read-out channel 11 for different datasets: step I (top left), step II (top right), step IV (bottom left) and step V (bottom right). The dose rates reported in the histograms refer to the SiPM board. The widening of the energy distribution is associated with the increase in SiPM dark counts as the absorbed radiation dose increases.*

3 Conclusions

The Crilin calorimeter offers a promising alternative to traditional sampling calorimeters for the future Muon Collider, effectively addressing the challenges posed by BIB while providing enhanced performance and cost efficiency. Its innovative semi-homogeneous design, consisting of high density crystal matrices read out by SiPMs, has demonstrated impressive time resolution and accurate energy measurements in both simulations and experimental tests.

In recent tests, Proto-1, the two-layer prototype of the Crilin calorimeter, achieved time resolutions better than 40 ps for energy deposits above 1 GeV. Additionally, the latest radiation resistance studies conducted on the prototype have revealed areas requiring further investigation, particularly concerning light yield reduction in the crystals due to TID. Variability in crystal performance, deterioration of the Teflon wrapping, and increased dark counts in the SiPMs were all observed, underscoring the need for additional studies to fully understand and mitigate these issues.

Overall, Crilin marks an advancement in calorimeter technology, offering a high-performance and cost-effective solution for future collider experiments. A key milestone is set for 2025, with the development of a significantly larger prototype that will cover 2 Molière radii and 22 radiation lengths, representing a further step for the calorimeter's R&D.

4 Acknowledgements

This work was developed within the framework of the International Muon Collider Collaboration (`https://muoncollider.web.cern.ch`), where the Physics and Detector Group aims to evaluate potential de-

tector R&D to optimize experiment design in the multi-TeV energy regime. This work was supported by the EU Horizon 2020 Research and Innovation Programme under Grant Agreements No. 101006726 and No. 101004761.
The author thanks the LNF Division Research and ENEA NUC-IRAD-GAM Laboratory (Casaccia R.C.) for their technical and logistic support. They also thank the BTF staff for providing the beam time and helping them get a smooth running period. In the end, the author thanks their thesis advisors Ivano Sarra and Elisa Di Meco as well as the organizers of the LNF 'Bruno Touschek' Summer School for the opportunity to present this work.

References

1. C. Accettura *et al*, Eur. Phys. J. C **83**, 864 (2023).
2. F. Collamati *et al*, JINST **16**, P11009 (2021).
3. L. Linssen *et al*, Physics and detectors at CLIC: CLIC conceptual design report (2012).
4. S. Ceravolo *et al*, JINST **17**, P09033 (2022).
5. A. Cemmi *et al*, JINST **17**, T05015 (2022).
6. M. Korzhik *et al*, Nucl. Instrum. Meth. A **1034**, 166781 (2022).
7. C. Cantone *et al*, IEEE Transactions on Nuclear Science **71**, 1116-1123 (2024).

Frascati Physics Series Vol. 76 (2024)
8th young researchers' workshop 'Physics Challenges in the LHC Era'
May 13 and 16, 2024

THE SEARCH OF MAGNETIC MONOPOLES WITH MISSING TRANSVERSE ENERGY TRIGGERS WITH THE CMS EXPERIMENT

Thales Menezes de Oliveira
Centro Brasileiro de Pesquisas Físicas

Abstract

The magnetic monopoles in the CMS Experiment could be studied as a long-lived particle by the reconstruction of the trajectory of a highly ionizing particle in the tracking system with a dedicated algorithm called TrackCombiner, and the expected shower shapes in the ECAL crystals. The Drell-Yan mechanism was used for the production of magnetic monopoles in particle colliders, with the production of mass points between 1000 GeV and 4500 GeV. The development of an alternative analysis strategy based on Missing Transverse Energy is also in development for the search of such particle in the CMS Experiment.

1 Introduction

The existence of a magnetically charged particle would add symmetry to the Maxwell's equations and could provide an explanation about the quantization of the electric charge in Nature, as proposed by Paul Dirac $^{1)}$, where the Dirac quantization condition implies the fundamental magnetic charge of the monopole (g_D) to be:

$$g_D = \frac{\hbar c}{2e} = \frac{e}{2\alpha} \approx 68.5e \tag{1}$$

where g_D is the Dirac charge, e is the proton charge and α is the fine-structure constant.

Because of the (g_D) large value, a monopole can induce ionization in matter thousands of times higher than a particle carrying the elementary electric charge. The existence of the monopoles as a topological solution for theories of forces unification has been subsequently suggested by 't Hooft and Polyakov $^{2,\ 3)}$. For unification theories involving symmetry-breaking scales $^{4)}$ monopoles of lower masses can arise, the electroweak monopole $^{5)}$, proposed as an hybrid between the Dirac and 't Hooft-Polyakov monopoles having a mass potentially accessible at the LHC.

2 The CMS Experiment

The CMS detector 6) consists in a superconducting solenoid of 6 m of internal diameter, providing a magnetic field of 3.8 T. Within the solenoid volume are a silicon pixel and strip tracker, a lead tungstate crystal electromagnetic calorimeter (ECAL), and a brass and scintillator hadron calorimeter, each composed of a barrel and two endcap sections. Forward calorimeters, made of steel and quartz-fibers, extend the pseudorapidity (η) coverage provided by the barrel and endcap detectors. The muon system consists of gas-ionization detectors embedded in the steel flux-return yoke outside the solenoid. A representation of the CMS Experiment could be observed in the figure 1.

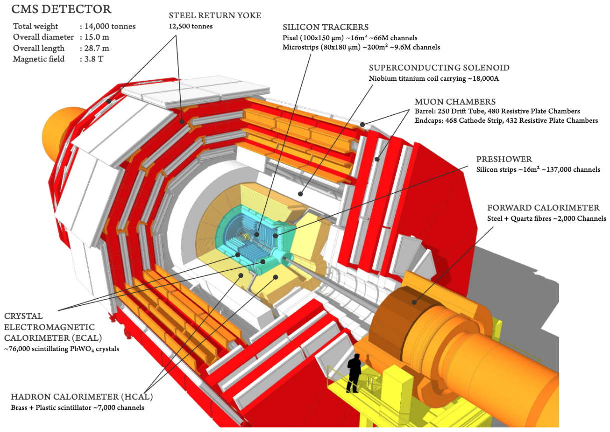

Figure 1: *The CMS Experiment.*

3 Analysis Strategy

The analysis strategy consists in the reconstruction of the magnetic monopole based on its signature in the CMS detector, where two discriminant parameters are defined. The consideration of the highly ionizing track from the monopole leads to the derivation of the $dE/dx_{\text{significance}}$ variable for the fraction of saturated strips. The topological cluster shape variable $f51$ is defined as a fraction of the energy in the central strip of the ECAL cluster, due to the narrow and concentrated energy deposits of the monopole, with little to no associated leakage in the HCAL.

3.1 Tracking Combining Algorithm

It is expected that a magnetic monopole candidate has a curved trajectory in the opposite direction of the magnetic field produced in the CMS solenoid, due to its magnetic charge. This peculiar behaviour yields the standard CMS track reconstruction algorithm inefficient for the reconstruction of the monopole track. The *Track Combiner* algorithm combines the tracks from the standard tracking algorithm into sets of track segments that could have been originated from a magnetically charged particle, using two different fits.

The first fit consists in a parabola in the ρ-z plane, where z is the direction of the magnetic field, to account for the possible curvature of the monopole track. The second fit is a circle in the x-y plane, which is the projection of the helical track to account for the possible electrically charged monopole candidates, where x and y correspond to the x-y plane of the coordination. Both fits equations are described by (2), while the fits on the trajectories for the MC monopole candidates with the cross-check with the simulated trajectory in Geant4 can be observed in the figure 2.

$$\begin{gathered} z = d + f\rho + g\rho^2 \\ y = a + sign(c)\sqrt{c^2 - (x-b)^2 - c} \end{gathered} \tag{2}$$

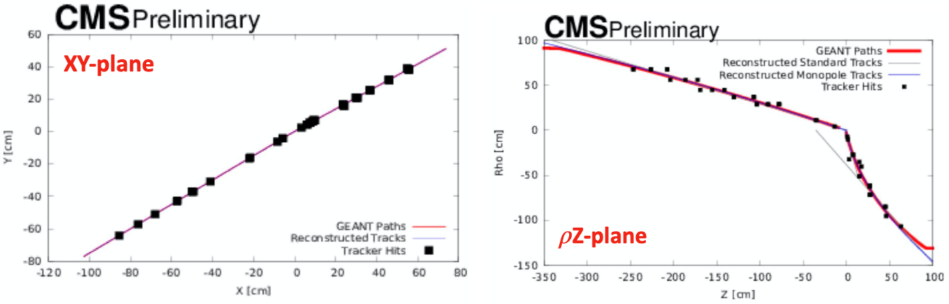

Figure 2: *The actual and fitted monopole trajectories. Left: The circular fit in the x-y plane. Right: The parabolic fit in the ρ-z plane.*

3.2 Track Ionization

Once the track of the monopole candidate is established, the measurement of its ionization can be performed. When a high ionized and energetic particle traverses the silicon tracker strips, the energy loss from the particle, excites a charge current in the silicon, where they became saturated for an energy loss higher than a certain threshold. For monopole candidates an average fraction around 0.7 of the strips are saturated due to its high ionization capacity, while for the minimum ionizing background this fraction is about 0.07. Thus, a significant variable $dE/dx_{\text{significance}}$ is developed using the binominal statistics to estimate the probability of occurrence of the strip saturation, described by (3). The left on figure 3 shows the fraction of strips versus the total number of strips for a monopole candidate with a mass of 1000GeV with the 2018 blinded data, without the evaluation of the analysis Signal Region.

$$\mathrm{dE/dX_{significance}} = \sqrt{-\log(\mathrm{BinomialI}(0.07, \mathrm{TotalStrips}, \mathrm{SaturatedStrips}))} \tag{3}$$

3.3 ECAL Cluster finding

The magnetic monopole's charge is equivalent to the charge of about 5000 electrons, it deposits all its kinetic energy in very few or even one crystal of the ECAL, generating the characteristic "spike"-like signature in the ECAL, as can be observed in the right on figure 3. Hence, a topological cluster variable f_{51}, defined by equation (4), is defined as the ratio of the energy aligned in 5 × 1 (η-ϕ) crystals by the energy deposited in a cluster of 5 × 5 crystals. The expected value of this ratio for the monopole candidates is around 1, due to its narrow deposit pattern, with little to no activity in the HCAL

$$f51 = \frac{E_{5\text{x}1}}{E_{5\text{x}5}} \tag{4}$$

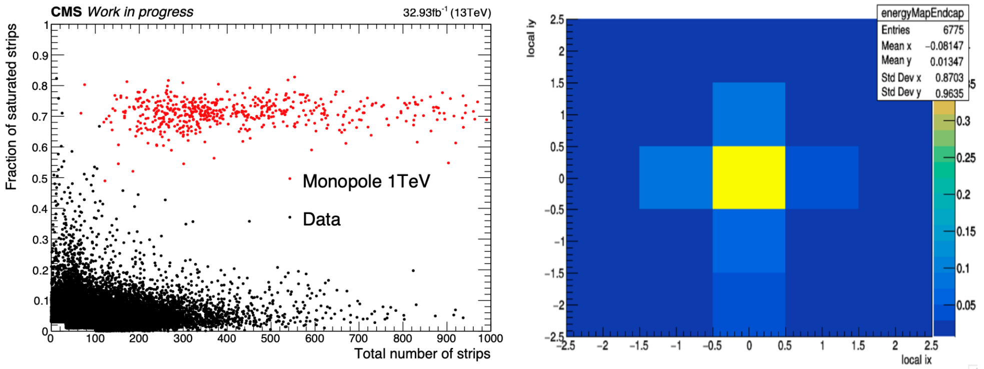

Figure 3: *Left: The fraction of saturated strips for a monopole candidate with 1000 GeV mass and the 2018 blinded data. Right: The average* $E_{crystal}/E_{5\times5}$ *for monopole candidates with mass of 1000 GeV, in the barrel region of the CMS ECAL.*

4 Data and Event Selection

4.1 Triggers

The analysis uses an unprescaled single photon trigger path, for 2016 the HLT_Photon175_v* was used while for 2017 and 2018, the HLT_Photon200_v*, which have E_T cuts of 175 GeV and 200 GeV, respectively. The energy deposition of a monopole and a photon carries some differences. However, due to the presence of the *strip Fine-Grained Veto Bit* (sFGVB) employed in both L1 and HLT levels to prevent the spikes from making large transverse energy in the reconstruction, this analysis can only considers a photon-like monopole, which doesn't deposit all of its energy in the central crystal.

4.2 Monopole Identification

The monopole reconstruction depends on the track fit parameters, track ionization and the ECAL cluster matching, which are combined to build the event selection criteria. Table 1 shows the preselection while the table 2 presents the discriminant variables. The monopoles are reconstructed from the extrapolation of the track to the ECAL, which is matched with the nearest ECAL cluster. The distance requirement between the monopole track and the ECAL cluster is required to satisfy $\Delta R = \sqrt{\phi^2 + \eta^2} < 0.5$.

Pre-selections	Parameters	Cuts
Circular fit parameters	$\lvert\text{XYPar0}\rvert \rightarrow d_0 = \sqrt{(a-c)^2 + b^2} - \lvert c\rvert$ $\lvert\text{XYPar2}\rvert \rightarrow$ radius of the circle	< 0.6 cm > 1000 cm
Parabola fit parameters	$\lvert\text{RZPar0}\rvert \rightarrow Z_0 = \lvert d\rvert$ $\lvert\text{RZPar1}\rvert \rightarrow \eta_0 = \lvert f\rvert$ $\lvert\text{RZPar2}\rvert \rightarrow \rho - Z$ curvature $= \lvert g\rvert$	< 10 cm < 999 $< 0.005\ \text{cm}^{-1}$
Matching parameters	$\Delta R = \sqrt{\eta^2 + \phi^2}$ HCAL Energy	< 0.5 < 10 GeV

Table 1: Pre-selections cuts applied to perform the monopole mathcing. The parameters are extracted from the circular and parabolic fits and the matching parameters.

Identification selection	Parameters	Cuts
Trigger Selection	HLT_Photon200_v*(2017,2018) HLT_Photon175_v*(2016)	
Energy Variables	$E_{5\times5}$ (2017,2018)	> 200 GeV
	$E_{5\times5}$ (2016)	> 175 GeV
	HCAL Energy	< 10 GeV
Significant Variables	$dE/dX_{\text{significance}}$	> 9
	$f51$	> 0.85

Table 2: Analysis discrimininant variables and their cuts applied for the identification of the monopole candidate.

4.3 Signal and Relative Efficiencies

The signal Monte Carlo sample for the full Run 2 for mass points from 1000 GeV to 4500 GeV were generated for the study of the signal efficiency, defined as (5).

$$\epsilon_{\text{sig}} = \frac{\text{no. of events after the selections}}{\text{no. of generated events}} \tag{5}$$

For this analysis, the trigger selection, the loose pre-selections and energy cut were applied first and later the candidates were sorted and the selection of the one with the highest $dE/dX_{\text{significance}}$ value was made. At last the tighter selection of the $dE/dX_{\text{significance}}$ and f_{51} are applied for the identification of the monopole candidates.

The signal efficiency after the application of the pre-selection and discriminant cuts is around 3% for the HLT_Photon_* paths, while it reaches 10% for the HLT_PFMET_* paths, which motivates the development of an alternative analysis strategy based on the MET information.

The largest source of inefficiency of the analysis is the trigger selection, due to the spike-killer algorithm, as shown on right of figure 3, which corresponds to the relative efficiency described by (6). For events passing the trigger selection, the monopole identification is relatively efficient.

$$\epsilon_{\text{rel}} = \frac{\text{no. of events after selection}}{\text{no. of events of the previous selection}} \tag{6}$$

5 Background Estimation

For this analysis the data driven two-dimensional side-band method Double ABCD is used. From two independent variables 9 regions are defined. The loose values of the independent variables define the regions 5, 6 and 8 as the Cross-check Regions (CR), while the region 9 is the Signal Region (SR), discriminated by tight cut values in the final selection of the analysis. A scheme of the region can be observed in figure 4.

The expected background in the CR are calculated with the regions 1, 2, 3 and 4, as (7). When the event number in the CRs have a good agreement with the actual number in the data, the expected background in the SR can be obtained as (8).

$$\mathrm{N}_5 = \frac{\mathrm{N}_2 \times \mathrm{N}_4}{\mathrm{N}_1}, \mathrm{N}_6 = \frac{\mathrm{N}_3 \times \mathrm{N}_4}{\mathrm{N}_1}, \mathrm{N}_8 = \frac{\mathrm{N}_2 \times \mathrm{N}_7}{\mathrm{N}_1} \tag{7}$$

$$\mathrm{N}_9 = \frac{(\mathrm{N}_3 + \mathrm{N}_6)(\mathrm{N}_7 + \mathrm{N}_8)}{\mathrm{N}_1 + \mathrm{N}_2 + \mathrm{N}_4 + \mathrm{N}_5}, \tag{8}$$

Figure 4: *Scheme for the Double ABCD method regions definitions and the calculation of the expected values for the cross-check and signal regions.*

6 Results and Conclusion

The experiment sensitivity can be determined in terms of the upper limit over the cross-section, where its limits are obtained using the frequentist method. With the CMS statistical analysis tool COMBINE 7), the preliminary results for the cross-section limit with the integrated luminosity scaled to 33 fb^{-1} to account for the 2016 Run II data taking period with $\sqrt{s} = 13$ TeV pp-collision is shown in the figure 5.

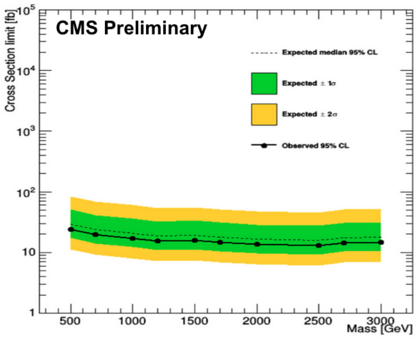

Figure 5: *The preliminary expected 95% CL upper limits with an integrated luminosity scaled to 33 fb^{-1} on the cross-section for the Drell-Yan spin-1/2 monopole.*

References

1. P.A.M. Dirac, Quantised singularities in the electromagnetic field, in: Proc. R. Soc. Lond A13360–72 (1931)
2. G. 't Hooft, Magnetic Monopoles in Unified Gauge Theories, Nucl. Phys. **B79**, 276 (1974)
3. A.M. Polyakov, Particle Spectrum in Quantum Field Theory, JETP Lett. **20** ,194 (1974)
4. G.Lazarides and Q.Shafi, The Fate of Primordial Magnetic Monopoles, Phys. Lett. **94B**, 149 (1980)
5. Y.M. Cho and D.Maison, Monopole configuration in Weinberg-Salam model, Phys. Lett. **B391**, 360 (1997)
6. CMS Collaboration, JINST **3** S08004 (2008)
7. CMS Collaboration, The CMS statistical analysis and combination tool: COMBINE, arXiv:2404.06614, (2024)

Frascati Physics Series Vol. 76 (2024)
8TH YOUNG RESEARCHERS' WORKSHOP 'PHYSICS CHALLENGES IN THE LHC ERA'
May 13 and 16, 2024

Probing New Forces Among 3rd Generation Quarks in the CMS Experiment

Maryam Shooshtari
Austrian Academy of Sciences (AT)

Abstract

The focus of this analysis is on probing new forces among 3rd generation quarks by investigating the production of four top quarks (4-top production) at the Large Hadron Collider (LHC) with the CMS detector. This analysis uses Effective Field Theory (EFT) to parameterize possible deviations from the Standard Model (SM) and explores potential new physics scenarios, including new scalar sectors, and top-philic resonances. We present an overview of the methodology, including analysis channels, machine learning techniques, and challenges in distinguishing signal from background. No final results are provided as the analysis is ongoing.

1 Introduction

The LHC, located at CERN, is currently the only collider capable of producing top quarks. With its high-energy proton collisions, it serves as a powerful tool to explore both Standard Model (SM) and Beyond Standard Model (BSM) physics. The CMS experiment is one of two major detectors at the LHC capable of identifying top quarks and their decay products.

Top quarks, the heaviest known particles in the SM, have a substantial Yukawa coupling, making them essential in understanding electroweak symmetry breaking and the Higgs mechanism. Their short lifetimes prevent them from forming bound states, allowing direct study of their decay products.

2 Motivation

This study focuses on the rare production of four top quarks ($t\bar{t}t\bar{t}$), which is the most energetic SM process observed. Due to its rarity and complexity, 4-top production is a valuable probe for new physics, as it can reveal deviations in the SM predictions.

We can explore several potential BSM scenarios, including:

- Extended scalar sectors (e.g., two Higgs doublet models from supersymmetry),
- High-mass vector bosons (Z', W'),

- Chiral colored force carriers (axigluons),
- Composite sectors with bound states mixing with the SM particles (e.g., right-handed top quark or Higgs compositeness).

3 Analysis Strategy

In this analysis, 4-top events are studied in final states with two same-sign leptons (2LSS), three leptons (3L) and four lepton (4L). The analysis uses advanced machine learning techniques, including multivariable classifiers (MVA), boosted decision trees (BDT), and top-quark tagging algorithms, to enhance signal-background separation.

Key challenges in the analysis include:

- The overwhelming $t\bar{t}$+heavy quarks background,
- Controlling uncertainties in jet multiplicities and b-jet tagging,
- Identifying signal characteristics in high jet multiplicity environments.

Figure 1 shows the distribution of events post-fit from Ref. $^{1)}$. Our analysis is a BSM interpretation of this paper.

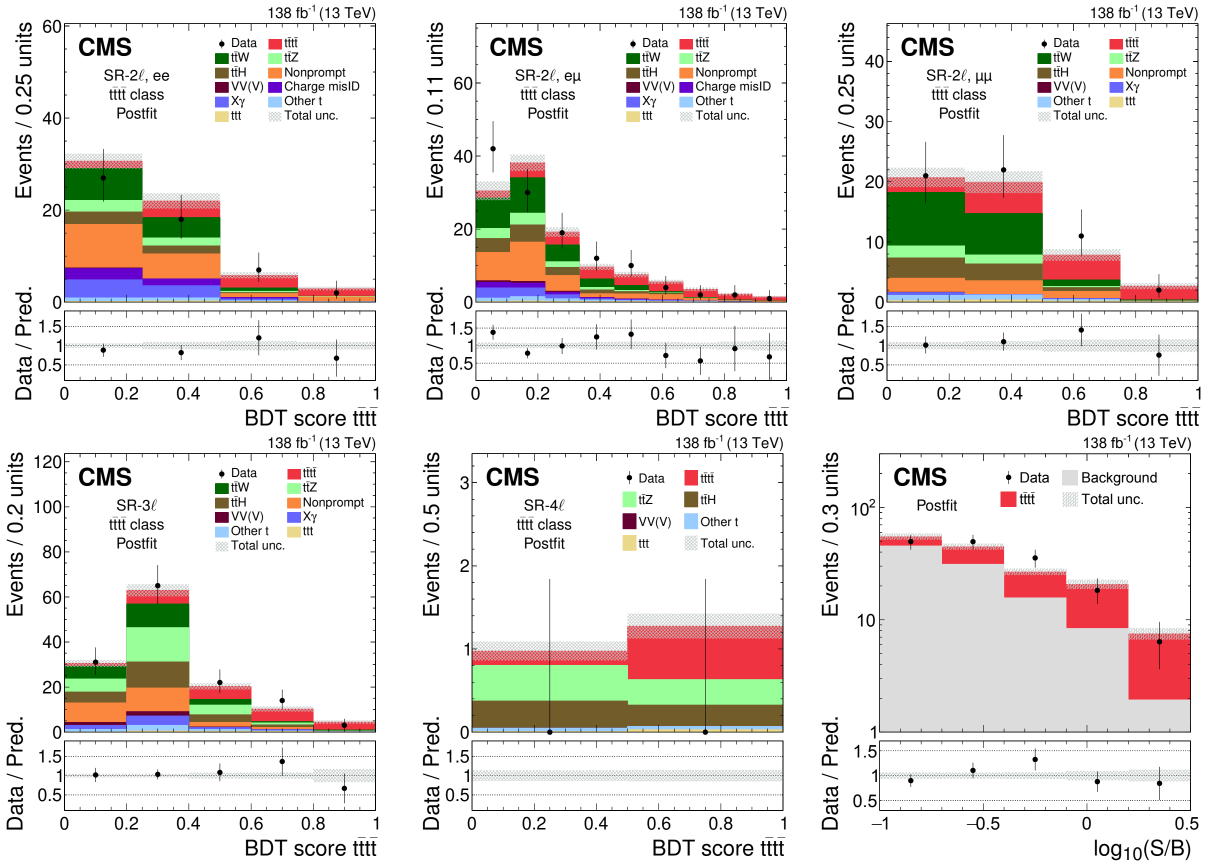

Figure 1: *Distribution of events in some of the signal regions used for the observation of* $t\bar{t}t\bar{t}$ *at CMS.*

4 Effective Field Theory

The EFT framework provides a model-independent approach to parameterizing new physics contributions to top-quark interactions. By adding higher-dimensional operators to the Standard Model Lagrangian, we can describe potential deviations from the Standard Model predictions. The dimension-6 operators of interest in this analysis primarily involve four-heavy-quark interactions.

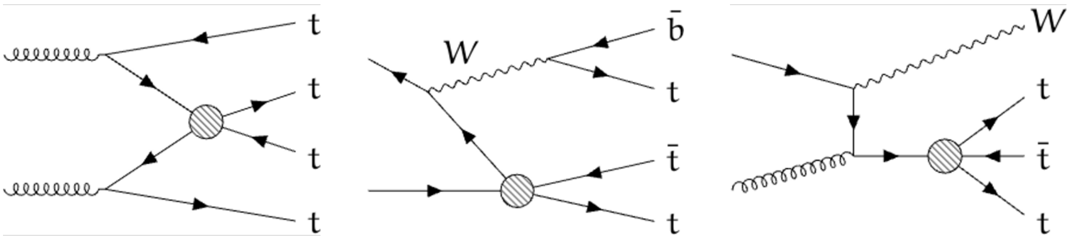

Figure 2: *Example diagrams of how the EFT operators can modify $t\bar{t}t\bar{t}$ and ttt events.*

The general form of the EFT Lagrangian is:

$$\mathcal{L}_{\text{EFT}} = \mathcal{L}_{\text{SM}}^{(4)} + \sum_i \frac{C_i}{\Lambda^2}\mathcal{O}_i, \tag{1}$$

where C_i are the Wilson coefficients and Λ is the scale of new physics. The operators $\mathcal{O}_i$ modify the interactions between top quarks and other particles, potentially leading to observable deviations in $t\bar{t}t\bar{t}$ or ttt production cross-sections. In table 1, operators included in this study are listed. Four of these operators are four-heavy-quark interactions, while the final operator allows us to study the top Yukawa coupling. This last operator has a complex Wilson coefficient, which probes both the CP-even and CP-odd sectors. Figure 2 shows some of the feynman diagrams through which these operators can modify $t\bar{t}t\bar{t}$ and ttt events. We simulated how each of these operators separately modifies SM distribution of events. This can be seen in figure 3. As expected, effect of four-heavy-quark operators is more pronounced in the tail of the distribution which shows higher energy events.

WC	**Operator**	**Definition**
c_{QQ}^1	$\mathcal{O}_{QQ}^1$	$\frac{1}{2}(\bar{Q}\gamma_\mu Q)(\bar{Q}\gamma^\mu Q)$
c_{tt}	$\mathcal{O}_{tt}$	$(\bar{t}\gamma_\mu t)(\bar{t}\gamma^\mu t)$
c_{Qt}^1	$\mathcal{O}_{Qt}^1$	$(\bar{Q}\gamma_\mu Q)(\bar{t}\gamma^\mu t)$
c_{Qt}^8	$\mathcal{O}_{Qt}^8$	$(\bar{Q}\gamma_\mu T^A Q)(\bar{t}\gamma^\mu T^A t)$
c_{tH}	$\mathcal{O}_{t\phi}$	$(\phi^\dagger\phi)\bar{Q}t\tilde{\phi}$

Table 1: *List of Wilson coefficients (WC), their corresponding operators, and definitions. Four of the operators are four-heavy-quark interactions, while the last operator is used to study the top Yukawa coupling, probing both CP-even and CP-odd sectors.*

5 Top Yukawa Coupling

$t\bar{t}t\bar{t}$ production can be used to extract the top quark Yukawa coupling in a way complementary to direct measurements, such as from $t\bar{t}H$ production. The sensitivity to Yukawa modifications arises because about 5% of the $t\bar{t}t\bar{t}$ cross-section stems from electroweak contributions, which depend on the top Yukawa coupling. Variations in the Yukawa coupling lead to shape differences in the kinematic distributions of $t\bar{t}t\bar{t}$ events. Modifications to the Yukawa coupling show up in the following Lagrangian terms :

$$\mathcal{L}_{eff} = \mathcal{L}_{SM}^{(4)} + \bar{Q}_L Y_t t\phi + h.c. \tag{2}$$

In order to probe this effects, we use a parametrization of the Yukawa coupling's effect on the $t\bar{t}t\bar{t}$ cross-section as follows:

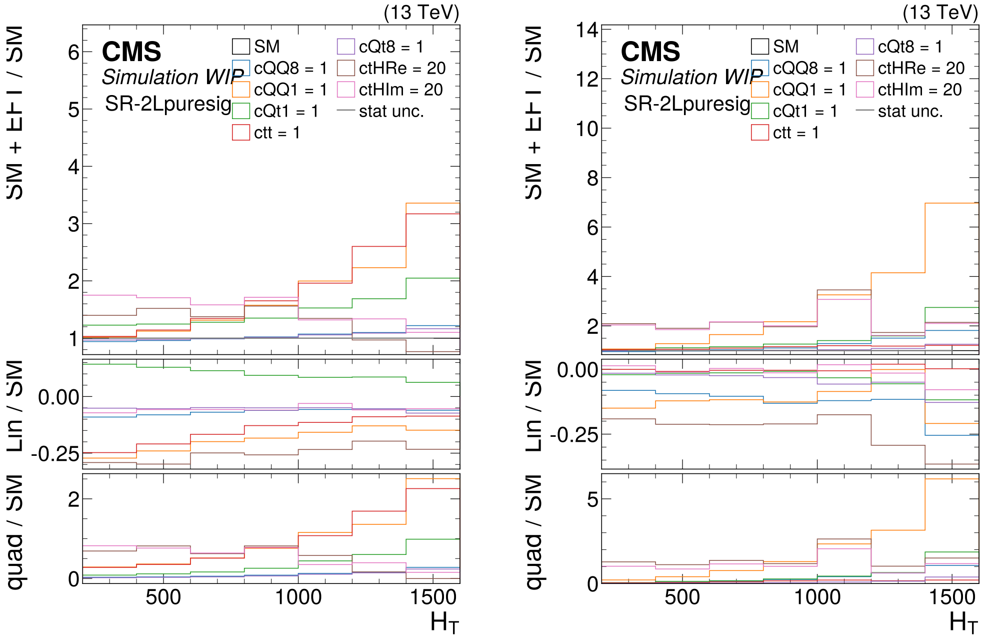

Figure 3: *Modification of distribution of events in H_T, which is the scalar sum of jet p_Ts, with respect to the SM value in $t\bar{t}t\bar{t}$ events (left) and ttt events (right).*

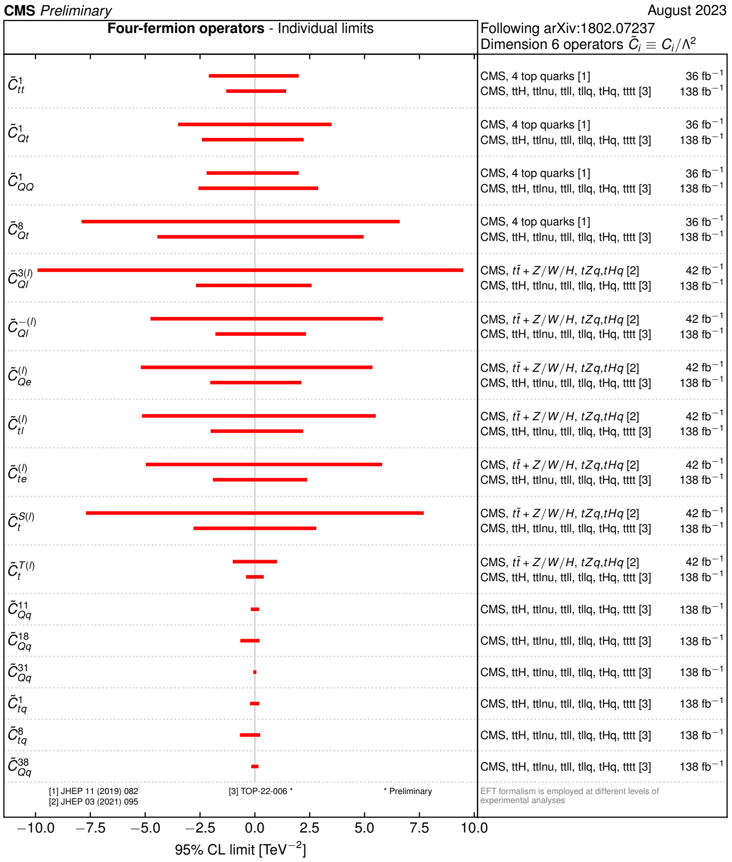

Figure 4: *Summary of results for limits on EFT operator values measured in several previous CMS analyses.*

$$\mathcal{L}_{ttH} = -\frac{m_t}{v}\phi\bar{t}(\kappa_{Htt}\cos\alpha + i\kappa_{Att}\sin\alpha\gamma_5)t \tag{3}$$

where κ_{Htt} is the CP-even coupling strength modifier, κ_{Att} is the CP-odd coupling strength modifier, and α is the mixing angle. Using this parametrization, we can probe the CP structure of the top Yukawa coupling. Figure 5 shows the result of a similar study in Atlas experiment.

Further, contributions from ttH an ttt processes are included in the analysis, providing additional sensitivity to deviations in the Yukawa coupling.

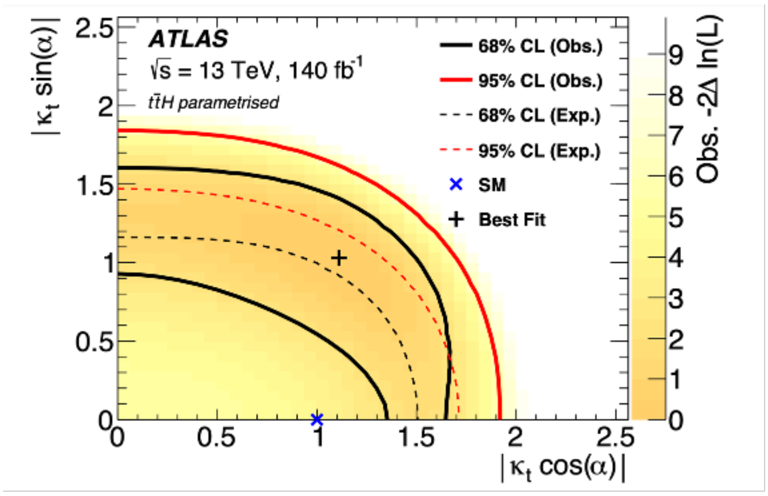

Figure 5: *CP structure of top Yukawa coupling extracted in Ref.* $^{2)}$ *. The x-axis shows the value for the CP-even, and the y-axis shows the value for the CP-odd part of the Yukawa coupling.*

6 Top-philic Resonances

In the search for top-philic resonances, we explore new bosons coupling predominantly to top quarks. Six models are considered, including scalar, pseudoscalar, and vector bosons in both color-singlet and color-octet representations. These resonances would produce distinctive signatures in $t\bar{t}t\bar{t}$ events, either through pair production or associated production mechanisms. Figure 6 shows some of the feynman diagrams through which these bosons can affect $t\bar{t}t\bar{t}$ production. According to Ref. $^{7)}$, new physics contributions to the Lagrangian from scalar singlet and octet scenarios look like this:

$$\mathcal{L}_{S_1} = \frac{1}{2}\partial_\mu S_1 \partial^\mu S_1 - \frac{1}{2}m_{S_1}^2 S_1^2 + y_1 \bar{t} S_1 t, \tag{4}$$

$$\mathcal{L}_{S_8} = \frac{1}{2}D_\mu S_8^A D^\mu S_8^A - \frac{1}{2}m_{S_8}^2 S_8^A S_8^A + y_8 \bar{t} T^A S_8^A t. \tag{5}$$

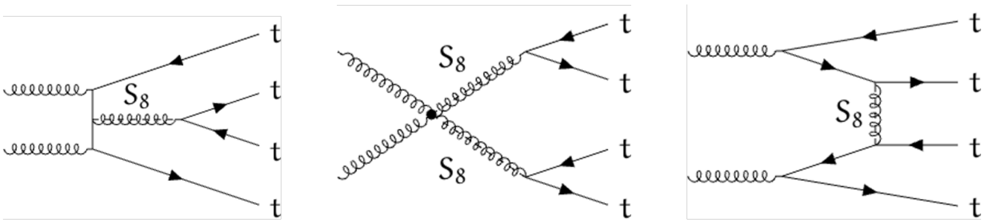

Figure 6: *Examples of diagrams where a scalar octet boson couples to $t\bar{t}$ pairs and modifies $t\bar{t}t\bar{t}$ production*

We simulate the production of these hypothetical particles and their potential impact on the $t\bar{t}t\bar{t}$ kinematics. Reweighting techniques are applied to probe different coupling strengths and mass points of these new particles. Figure 7 shows the predicted upper limit for two the boson scenarios studied in Ref. 6).

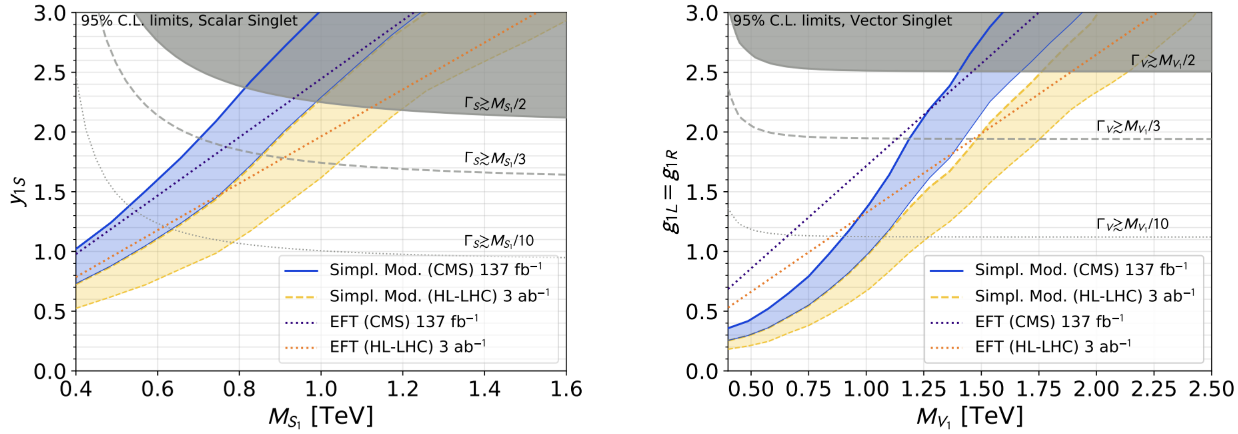

Figure 7: *Examples of 95% confidence limits for a scalar singlet (left), and vector singlet (right) model presented for different masses as a function of the coupling.*

7 Conclusions

This analysis presents a comprehensive approach to probing new physics using 4-top production at CMS. The challenges in isolating signal from background are significant, but advancements in machine learning and tagging techniques offer promising improvements. Future work will focus on tightening constraints on EFT operators and exploring new physics models in greater detail.

References

1. CMS Collaboration, "Measurement of the four-top quark production cross section in proton-proton collisions at sqrt(s) = 13 TeV," arXiv:2305.13439.
2. ATLAS Collaboration, "Observation of four-top-quark production in the multilepton final state in proton-proton collisions at sqrt(s) = 13 TeV," arXiv:2303.15061.
3. R. Aoude, H. El Faham, F. Maltoni and E. Vryonidou, "Complete SMEFT predictions for four top quark production at hadron colliders," JHEP **10** (2022), 163 doi:10.1007/JHEP10(2022)163 [arXiv:2208.04962 [hep-ph]].
4. Q.-H. Cao, S.-L. Chen, Y. Liu, Y. Wang, "Limiting top quark-Higgs boson interaction and Higgs-boson width from multitop productions," Phys. Rev. D 99 (2019) 113003, arXiv:1901.04567.
5. Q. H. Cao, S. L. Chen and Y. Liu, "Probing Higgs Width and Top Quark Yukawa Coupling from $t\bar{t}H$ and $t\bar{t}t\bar{t}$ Productions," Phys. Rev. D **95** (2017) no.5, 053004 doi:10.1103/PhysRevD.95.053004 [arXiv:1602.01934 [hep-ph]].
6. L. Darmé, B. Fuks, and F. Maltoni, "Top-philic heavy resonances in four-top final states and their EFT interpretation," JHEP 09 (2021) 143, arXiv:2104.09512.
7. L. Darmé, B. Fuks, H. L. Li, M. Maltoni, O. Mattelaer and J. Touchèque, "Boosting Beyond: A Novel Approach to Probing Top-Philic Resonances at the LHC," [arXiv:2404.14482 [hep-ph]].

Frascati Physics Series Vol. 76 (2024)
8th young researchers' workshop 'Physics Challenges in the LHC Era'
May 13 and 16, 2024

SEARCH FOR EMERGING JETS WITH THE ATLAS DETECTOR

Thomas Wojtkowski
Laboratoire de Physique Subatomique & Cosmologie, Université Grenoble Alpes, Grenoble

Abstract

The Standard Model of particle physics cannot explain the composition of Dark Matter in the Universe. Some Beyond the Standard Model theories predict the existence of a dark sector which contains new hypothetical particles : stable particles in this sector are Dark Matter candidates. The new particles could weakly interact with Standard Model ones through a new interaction, and thus could be produced in proton-proton collisions at the LHC. In the search for emerging jets, we are looking for invisible particles from this sector decaying to Standard Model particles with a certain lifetime, producing displaced signals in the detector called emerging jets. The challenge of this analysis is to be able to detect these very rare interactions among the LHC Run 3 data, by understanding the signature of such particles and by selecting a maximum of events that may contain emerging jets while rejecting background events.

1 Introduction

The Standard Model of particle physics that describes efficiently the elementary particles and their interactions is not fully complete because it is unable to explain some physical observations. For example, several cosmological measurements, like the galaxy rotation curves, indicate that there may exist a non standard invisible matter called dark matter, interacting gravitationally with visible matter. Observations suggest that dark matter accounts for 26 % of the energy-mass in the Universe, while the visible matter represents only 5 %.

The nature of dark matter is still unknown and its detection is very difficult. Several hypotheses are trying to explain its composition : it could be made of new massive and stable particles, interacting with visible particles through very rare processes. A possibility is that these particles belong to a hidden sector that would be connected to the Standard Model, and in this way, the investigation of this sector could be possible at colliders.

2 The ATLAS detector

The ATLAS detector 1) is one of the detectors present at the Large Hadron Collider (LHC). It is made up of several complementary sub-detectors organized in concentric layers around the interaction point. The first layer the emitted particles cross is the inner detector, that measures a track for each charged particle that is curved by a solenoidal magnet, allowing to measure their momentum transverse to the beam (p_T). Particles then enter the calorimeters where they (except for muons and neutrinos) are stopped, depositing all their energies in groups of nearby calorimeter cells called clusters. The last layer is the muon spectrometer which, thanks to the magnetic field produced by toroidal magnets, allows to reconstruct the muons trajectory and momentum.

ATLAS also relies on a trigger system, allowing to select and store potentially interesting events for future various physics analysis. An offline event reconstruction is performed on the recorded events to convert detected signals into physical objects like jets, leptons, photons, etc.

3 The hadronic jets

During proton-proton collisions, the partons composing the protons interact and can cause the emission of high transverse momentum partons. Through QCD interactions, the emitted partons radiate other gluons or produce quark - anti-quark pairs, creating what is called a parton shower. Along this parton shower, the strong interaction coupling effectively increases, leading to the hadronization process in which the partons gathers to form colorless hadrons. It results in the formation of a cone containing hadrons which is carrying information about the original parton (Figure 1). These hadronic jets are highly common due to the high cross section of the QCD interactions.

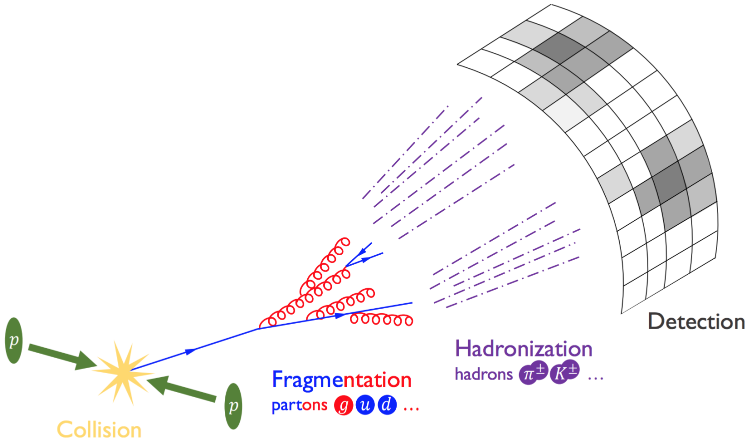

Figure 1: *Scheme of the jet production process in proton-proton collision* 2)

In ATLAS, different methods can be used to reconstruct the jets in a collision event. In a first step, the jet constituents are reconstructed : they represent the momentum of the emitted particles and can be built from calorimeter clusters only or from more complex combination of inner detector tracks and calorimeter measurements. The constituents are then grouped by a jet algorithm (parametrized by a tunable radius in the angular plan), based on their transverse momentum and spatial proximity.

4 The Dark sector

To explain and describe dark matter, a dark sector, corresponding to an extension of the Standard Model, can be considered. In such models, new quantum fields associated to new hypothetical particles with interactions analogous to QCD are introduced : they can be called dark quarks q_d and dark gluons g_d, and the Lagrangian describing their interaction can be written as :

$$\mathscr{L}_d = \bar{q}'_i(i\not{D} - m_{q'_i})q'_i - \frac{1}{4}G'^{\mu\nu}G'_{\mu\nu} \tag{1}$$

where q'_i and $G'^{\mu\nu}$ represent respectively the dark quark field and the dark gluon gauge field, and D accounts for the gauge covariant derivative of the new SU(N_d) gauge group that is introduced 3). Because of the analogy between this Lagrangian and the QCD one, an energetic dark parton can undergo a parton shower and a hadronization in this dark sector, and then produce a jet containing invisible dark hadrons (which would correspond to the lightest mesons). The stable dark hadrons in this sector can be dark matter candidates.

To be able to investigate this dark sector in collider experiments, a new interaction between Standard Model quarks and dark particles has to be introduced. This allows to model the production of dark quarks at the LHC and the decay of unstable dark hadrons to Standard Model quarks which would then result in detectable jets. Two main parameters can describe the possible jet signature : the percentage of stable dark hadrons in the jet and the lifetime of the unstable dark hadrons (Figure 2). Dark sector jets with prompt dark mesons decays and low invisibility fraction are called dark jets, while those with higher fraction of invisible particules are named semi-visible jets. The jets containing dark hadrons decaying to visible particules with a non negligible lifetime (but still in the detector) are called emerging jets. In the case where the jets contain only stable dark hadrons or if their lifetime multiplied by Lorentz factor γ is greater than the detector size, no signal can be detected, and the signature is similar to the pair-production of 'Weakly Interacting Massive Particles' : mono-jet search can investigate this type of model by considering the emission of radiation in the initial state.

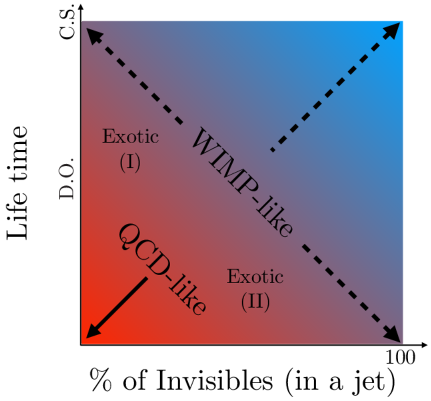

Figure 2: *Dark sector jets parametrization. D.O. and C.S. mean respectively 'displaced objects' and 'collider stable'. Exotic(I), Exotic(II) and QCD-like represent respectively emerging jet, semi-visible jet and dark jet* 3).

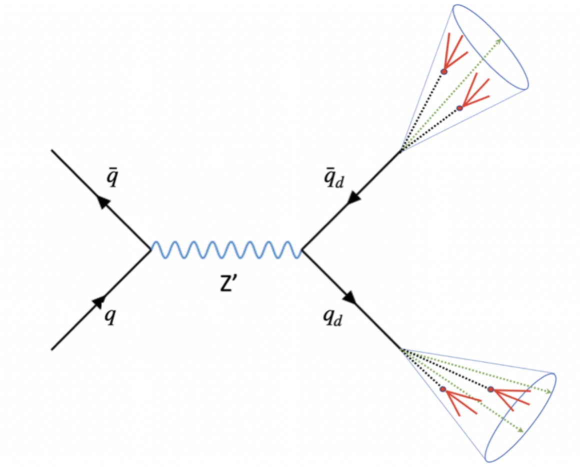

Figure 3: *Diagram of the considered dark quark pair production process*

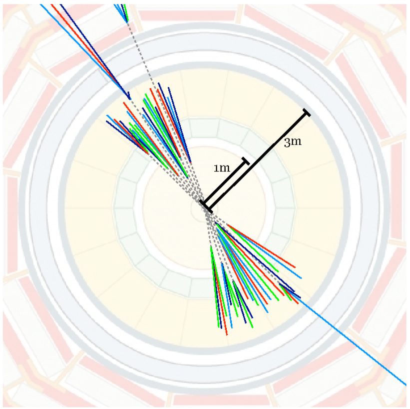

Figure 4: *Production of a pair of emerging jets. The dotted lines represent invisible dark mesons, while the colored lines are visible particles* 4).

5 Emerging jet analysis

5.1 Investigated models

In this analysis, the dark quark production is made possible through a new Z' massive boson that produces a dark quark - anti-dark quark pair from a Standard Model quark - anti-quark initial state (Figure 3). The Lagrangian describing this interaction is the following :

$$\mathscr{L}_{med} = -\frac{1}{4}Z'^{\mu\nu}Z'_{\mu\nu} - \frac{1}{2}M^2_{Z'}Z'^{\mu}Z'_{\mu} + Z'_{\mu}(g_{q_d}\bar{q}'_i\gamma^{\mu}q'_i + g_q\bar{q}_j\gamma^{\mu}q_j) \tag{2}$$

where q_i represents the Standard Model quark field, and $Z'_{\mu\nu}$ the field corresponding to the Z' boson 3). Its coupling constants to the Standard Model quark g_q and to the dark quarks g_{q_d}, as well as its mass are free parameters of the model.

In this process, each of the two dark quarks produces a jet containing unstable dark mesons ρ_d and π_d. The ρ_d promptly decays into π_d, while this latter decays to Standard Model quarks. The particularity is that the π_d are considered to have a lifetime of some millimeters, producing the emerging jet signature where the detectable signal is not starting at the interaction point (Figure 4) 4). This event topology is yet unexplored at the LHC.

In Table 1, the values of the free parameters used for the generation of signal events are presented. The mass of the ρ_d is fixed to $4m_{\pi_d}$, and the dark sector confinement scale Λ_d is set to $2m_{\pi_d}$.

m_{π_d} (GeV)	5, 10, 20
$c\tau_{\pi_d}$ (mm)	5, 50
$m_{Z'}$ (GeV)	600, 1500, 3000

Table 1: *Free parameters of the model used for the signal event generation*

5.2 Analysis strategy and trigger

Because emerging jets hadronize in both hidden and visible sectors, they are expected to contain more particles and to be larger than usual jets from Standard Model processes. In this analysis, we are looking for events corresponding to a final state with two large and energetic jets which will be associated to displaced tracks starting at secondary vertices.

The dominant background from Standard Model processes are di-jet events from QCD interactions. Indeed, these events are very common at the LHC and they can also in some cases produce a displaced signature in the detector (for example when jets containing neutral B-mesons decay into charged particles and produce displaced tracks, or photons producing electron - positron pairs in dense areas of the detector).

This analysis implements a 'cut-and-count' strategy : the principle is to apply selections on the recorded events by considering discriminating variables between the QCD background and the emerging jet signal in order to reject most events from the former while selecting the latter. First, the choice of the variables and their cut values are determined by considering events from simulation : these cuts define a signal region (SR) in which the signal-to-background ratio is expected to be important. The estimation of the expected background event count in this SR is performed in a blinded way, i.e by using only data events from other regions than the SR. Once it is done, the total number of events from data in the SR is revealed and compared to the Standard Model expectation. Statistical interpretations are then made to determine if the data contains a significant excess. Otherwise, constraints on model parameters are set (such as on the signal cross-sections, the π_d lifetime ...).

The first selection to be applied on data is the trigger. In ATLAS, two potentially interesting triggers are available for this analysis. The first one (called 'high-p_T jet trigger') records events in which a large radius jet with a p_T higher than 460 GeV has been detected. The second one (called 'emerging jet trigger') stores events in which a large radius jet with a p_T higher than 200 GeV and a prompt track p_T fraction (PTF) lower than 0.08 has been detected. The PTF corresponds to the ratio between the sum of the p_T of prompt tracks associated to the jet over the total p_T of the jet, and is expected to be lower for emerging jets compared to QCD ones.

Even if the high-p_T jet trigger has a better efficiency than the emerging jet trigger, both of them are used for the analysis : indeed, the trigger determines the lowest value of $m_{Z'}$ that can be probed, and the emerging jet trigger allows to complement the high-p_T trigger at lower masses.

In consequence, the adopted strategy is the following : two separate event selections are defined, one based on the high-p_T jet trigger, and the other based on the emerging jet trigger to be sensitive to low $m_{Z'}$ signal. The latter will be considered in the following sections of this document.

5.3 Event selection

Before considering discriminating variables, some pre-selections are applied to the events. They must :

- pass the emerging jet trigger,
- have at least two jets,
- satisfy $p_T > 300$ GeV and $PTF < 0.025$ for the leading jet in p_T to only select events passing the trigger with a maximum and constant efficiency,
- and have at least one secondary vertex associated to each of the two leading jets.

Two sorts of jet discriminating variables can be considered in this analysis : track-variables, that exploit the fact that emerging jets are more likely to contain displaced tracks, and substructure variables, that are related to the internal repartition of the energy inside the jet.

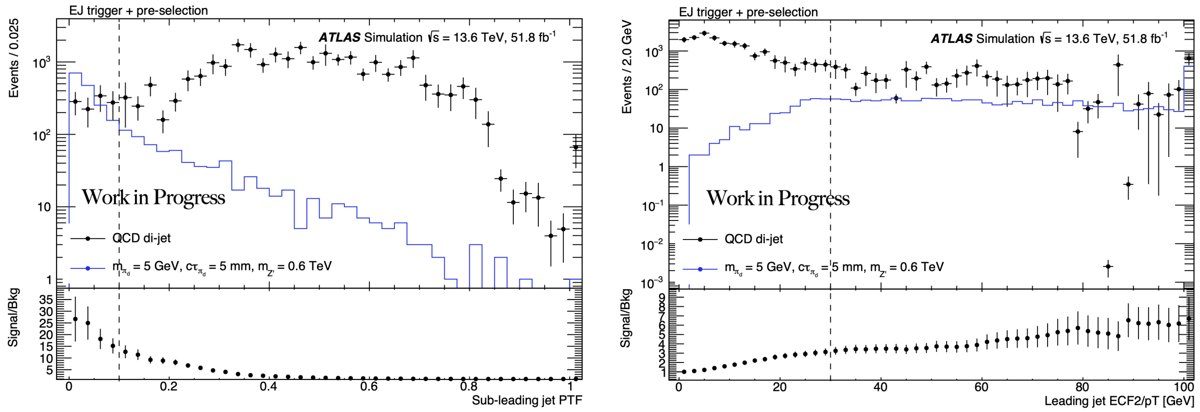

(a) *Sub-leading jet PTF* (b) *Leading jet ECF2/p_T*

Figure 5: *Distributions of the two discriminating variables for background and signal events after preselections. The value of the signal-to-background ratio after a given cut is shown in the bottom panel. The dashed vertical lines show the position of the analysis cut values.*

The PTF is used as track-variable because it has been found to be the most discriminating one ; it is defined as :

$$PTF^{jet} = \frac{\sum_{track \in jet} p_T^{track}(d_0 < 2.5\sigma_{d_0}(p_T))}{p_T^{jet}} \tag{3}$$

where d_0 is the track transverse impact parameter and $\sigma_{d_0}(p_T) = \frac{0.0463}{p_T + 0.0195}$ (with p_T in GeV, and d_0 in mm).

The discriminating substructure variable is called ‘Energy Correlation Factor 2’ (ECF2), and is defined as :

$$ECF2^{jet} = \sum_{i,j \in jet} p_{T_i} p_{T_j} \Delta R_{ij} \tag{4}$$

where the sum is over the constituents of the jets, and ΔR_{ij} represents the angular distance between two constituents 5). $ECF2$ is expected to be higher for emerging jets compared to QCD jets.

Figure 5 shows the distribution of these variables for simulated QCD di-jet events normalized to a luminosity of 51.8 fb^{-1} and for one signal. For the following, the signal region will be defined with these two cuts :

- $PTF < 0.1$ for the sub-leading jet in p_T,
- $\frac{ECF2}{p_T} > 30$ GeV for the leading jet in p_T.

5.4 Background estimation

In this analysis, the background estimation is done with an ‘ABCD method’ 6). With the two cuts on PTF and ECF2/p_T, the events can be distributed in four regions (Figure 6) :

- A (the signal region) : $PTF < 0.1$ and $\frac{ECF2}{p_T} > 30$ GeV,
- B : $PTF \geq 0.1$ and $\frac{ECF2}{p_T} > 30$ GeV,
- C : $PTF < 0.1$ and $\frac{ECF2}{p_T} \leq 30$ GeV,
- and D : $PTF \geq 0.1$ and $\frac{ECF2}{p_T} \leq 30$ GeV.

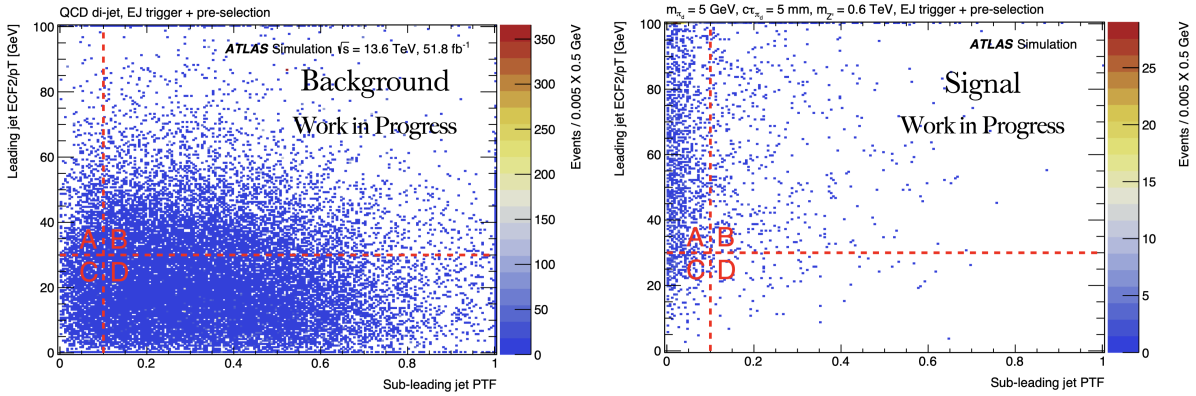

(a) *Background events* (b) *One signal events*

Figure 6: *Distributions of background and signal events in the ABCD plane after pre-selections.*

The method then consists in considering N_B, N_C and N_D, the number of counted data events in region B, C and D, to compute the expected background contribution in the signal region with this formula :

$$N_A^{bkg} = \frac{N_C^{bkg}}{N_D^{bkg}} \times N_B^{bkg} \approx \frac{N_C}{N_D} \times N_B \tag{5}$$

where N_X^{bkg} is the number of background events in the region X. Indeed, the first equality is true if the two variables defining the ABCD plane are perfectly decorrelated for background events, and the second one necessitates a negligible signal presence in B, C and D regions. This sort of background estimation is characterized as 'data driven' : it is necessary in this analysis because the simulated background is not reliable enough to provide a precise background estimation.

QCD di-jet	N_{events} ± statistical uncertainty
A	305 ± 141
B	6324 ± 730
C	818 ± 182
D	17462 ± 1003
$(B \times C)/D$	296 ± 76

Table 2: *Number of simulated background events in A, B, C and D regions and background prediction in the signal region, normalized to an integrated luminosity of 51.8 fb*$^{-1}$.

Verifications of the validity of the method must be performed. The first is to apply it to simulated events (Table 2). The method will also be verified in some validation regions in data. Those are defined in the variable plane, depending on a parameter $X > 0.1$ (Figure 7), such as :

- A' : $0.1 < PTF < X$ and $\frac{ECF2}{p_T} > 30$ GeV,
- B' : $PTF \geq X$ and $\frac{ECF2}{p_T} > 30$ GeV,
- C' : $0.1 < PTF < X$ and $\frac{ECF2}{p_T} \leq 30$ GeV,
- and D' : $PTF \geq X$ and $\frac{ECF2}{p_T} \leq 30$ GeV.

Then, depending on X, the value of $(N_{B'}^{bkg} \times N_{C'}^{bkg})/N_{D'}^{bkg}$ is compared to $N_{A'}^{bkg}$. First verifications are done on simulated background events (Figure 8).

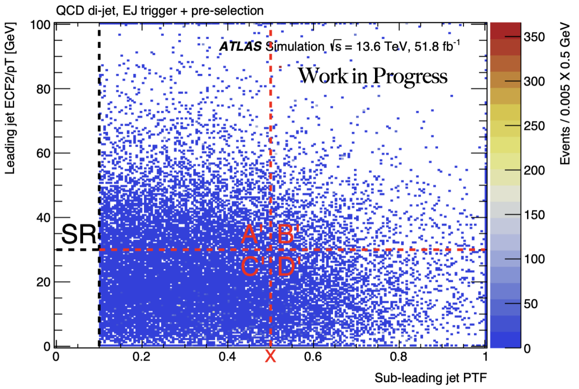

Figure 7: *Background events distribution in the ABCD plane after pre-selections only in validation regions.*

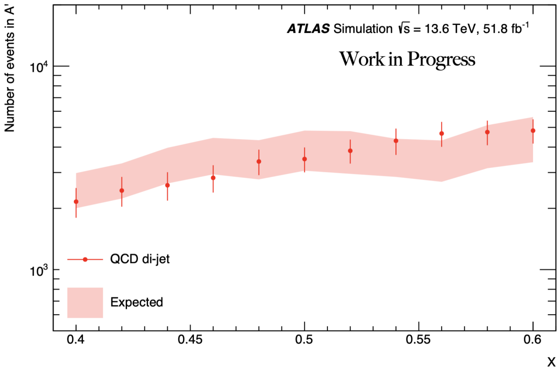

Figure 8: *Comparison between observed and expected number of background events in the region $A^{'}$ depending on X.*

6 Conclusion

In this proceeding, ongoing work on an analysis looking for new long-lived particles that produce an unusual di-jet topology in the ATLAS detector has been presented. The global strategy is to apply cuts on data to reduce background presence while selecting at maximum the emerging jet signal. Additional selections can be also considered, such as extra requirements on the displaced vertices (like their number of associated tracks), or on the di-jet invariant mass in order to target specify range for the $m_{Z'}$ value. ABCD method is used to obtain an estimation of the background from the data without relying on simulation ; it has also to be verified in data events in a blinded way.

References

1. The ATLAS Collaboration. *The ATLAS Experiment at the CERN Large Hadron Collider: A Description of the Detector Configuration for Run 3*. JINST 19 (2024), p.05063. DOI : 10.1088/1748-0221/19/05/p05063. arXiv:2305.16623

2. Eric M. Metodiev. *The Fractal Lives of Jets*. 2020.
URL : https://www.ericmetodiev.com/post/jetformation

3. Park, Myeonghun and Zhang, Mengchao. *Tagging a jet from a dark sector with jet substructures at colliders*. Physical Review D 100.11 (2019), p.115009. DOI : 10.1103/physrevd.100.115009. arXiv:1712.09279 [hep-ph]

4. Schwaller, Pedro and Stolarski, Daniel and Weiler, Andreas. *Emerging jets*. Journal of High Energy Physics 05 (2015), p.059. DOI : 10.1007/jhep05(2015)059. arXiv:1502.05409

5. The ATLAS collaboration. *Measurement of jet-substructure observables in top quark, W boson and light jet production in proton-proton collisions at $\sqrt{s}$ = 13 TeV with the ATLAS detector*. Journal of High Energy Physics 08 (2019), p.033. DOI : 10.1007/jhep08(2019)033. arXiv:1903.02942

6. W. Buttinger. *Background estimation with the ABCD method*. 2018.
URL : `https://twiki.cern.ch/twiki/pub/Main/ABCDMethod/ABCDGuide_draft18Oct18.pdf`

Frascati Physics Series Vol. 76 (2024)
8th young researchers' workshop 'Physics Challenges in the LHC Era'
May 13 and 16, 2024

New experimental approach to probe the X17 existence

Behnam Ali-Mohammadzadeh
Istituto Nazionale di Fisica Nucleare (INFN/Rome)
Evaristo Cisbani
Istituto Nazionale di Fisica Nucleare (INFN/Rome) and Istituto Superiore di Sanità
Carlo Gustavino
Istituto Nazionale di Fisica Nucleare (INFN/Rome)

Abstract

Potential signatures of a new particle, named X17 boson, have been associated to anomalies recently observed in the emission of electron-positron pairs in ^{7}Li(p,e$^-$e$^+$)^{8}Be and ^{3}H(p,e$^-$e$^+$)^{4}He reactions. These observations have triggered new experiments to probe the X17 existence. For such a goal, we propose to search the X17 boson in the decay of excited levels of ^{4}He through the study of the ^{3}He(n,e$^-$e$^+$)^{4}He process and using the n_TOF neutron beam facility. This reaction is conjugate to the ^{3}H(p,e$^-$e$^+$)^{4}He process, and thus provides a complementary experimental approach with respect to the reported experiments in the literature. The prerequisite for this experiment is to prove its experimental feasibility, taking into account the *n_TOF* specificities and using state of the art tracking detector for e$^-$ and e$^+$. In this direction we evaluate and characterize an experimental setup based on the use of μRwell gas detectors used as Time Projection Chambers coupled with a system of scintillation bars. First results of this evaluation are presented in this proceeding.

1 Introduction

The Standard Model of particle physics (SM) cannot be considered such a complete theory since it does not explain neutrino masses, the cosmological baryon asymmetry among other open problems. In particular, Dark Matter (DM) evidence remains unexplained which is considered to be one of the unsolved mysteries in particle physics. In this regard several experimental investigations have been dedicated to search DM light mediators, like axions, dark photons or light Z$'$ 1, 2). A few years ago, the ATOMKI group reported an anomaly in the relative angle between the electron-positron emission for two nuclear processes, namely the $^7Li(p,e^+e^-)^8Be$ and $^3H(p,e^+e^-)^4He$ reactions 3). For both reactions the anomaly consists of an excess of pairs emitted with a large relative angle. This excess is kinematically compatible with the creation of a new particle with mass of about 17 MeV/c^2 (hereafter the X17 boson) 3), rapidly decaying into e^+e^-. This boson could be a mediator for a fifth force as well as a portal to the DM sector. The ATOMKI experimental setup used for the $^3H(p, e^+e^-)^4He$ reaction consisted of a tritium target absorbed on Ti layer which was bombarded with a proton beam with a current of about 1 μA. The beam line was surrounded by a 1 mm thick carbon tube. The detection of ejectiles is provided by six modules placed around the target. Each module consists of a set of stereo silicon strips facing the target, providing the impact point of ejectiles (and therefore the angular aperture between them). Silicon strips are backed by a thick plastic scintillator to measure the total kinetic energy of electrons and positrons. The $^3H(p, e^+e^-)^4He$ reaction is allowed in the Standard Model, in which a virtual photon is converted into an electron-positron pair (Internal Pair Conversion, IPC). The opening angle of IPC distribution is sharply peaked at low values of Θ and fall smoothly monotonically for increasing values of Θ. This is not what is seen in the $^4He^*$ decay. Instead, there are pronounced bumps at $\Theta \simeq 120°$ 4). The bumps are interpreted as the signature of a boson into e^+e^- pairs. As an example, Fig. 2 shows the angular correlation of the e^+e^- pairs coming from the excited ^{8}Be* at E$_t$=18 MeV, assuming the creation of a boson of different mass promptly decaying into e^+e^- pairs. As expected, the excess shown in Fig. 1 shifts towards smaller aperture angle while increasing the excitation energy. Members of our group have proposed to investigate the reaction $^3He(n, e^+e^-)^4He$ using the pulsed neutron beam available at the EAR2 experimental area of the n_TOF CERN facility 10). This approach is complementary to the study of the above mentioned $^3H(p, e^+e^-)^4He$ reaction, using a proton beam. The goal of the experiment is to shed light on the X17 boson claim and to investigate its quantum numbers.

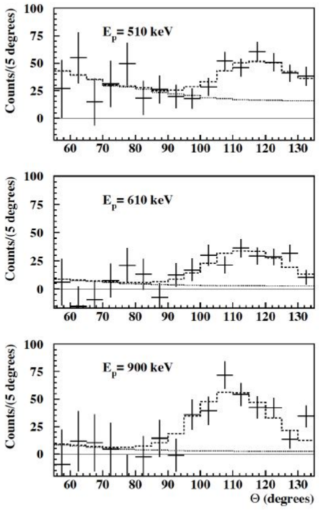

Figure 1: *Angular correlations for the e^+e^- pairs measured in the $^3H(p, e^+e^-)^4He$ reaction at E_p=510, 610, 900 kev.*

2 Proposed experimental setup

The detectors proposed for the experiment at n_TOF are schetched in Fig. 3: the ^{3}He target is surrounded by 4 μRWELL detectors 13, 14) acting as Time Projection Chambers (TPCs), with active surface of about 380 × 460mm^2 each equipped with orthogonal readout strips; the gap between the cathode and the multiplication anode plane is 3 cm. In this way it is possible the 3D reconstruction of the crossing

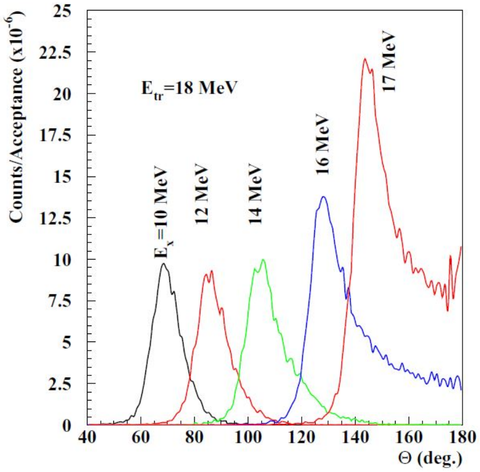

Figure 2: *Simulated angular correlations of* e^+e^- *pairs from the decay of a boson with different masses, as indicated for each curve shown in the plot.*

particles. The trigger of the μRWELL is provided by 4 planes of plastic scintillating bars (SCIONIX EJ-212), in which each plane is made of 32 bars of $3 \times 17 \times 500$ mm^3. In addition, the bars provide the time of flight of the neutrons to deduce their energy. Finally, the target and the active detectors are inserted into a coil with a square section which provides a magnetic field of 500 Gauss.

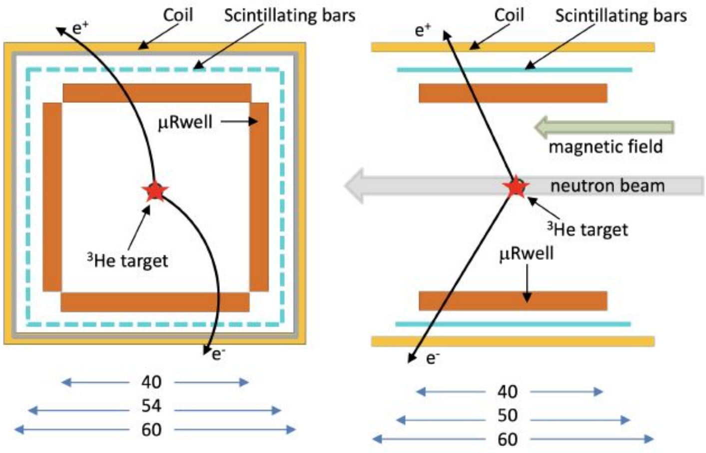

Figure 3: *Sketch of the detector setup for the X17 experiment at n_TOF.*

As shown in Fig. 3, the magnetic field affects the track direction, in such a way the charge and momentum of electron and positron are deduced by the intercept and the slope of tracks inside the active volume. The n_TOF detector has many advantages with respect to the ATOMKI one:

- It has a large detector angular acceptance, to probe the quantum numbers of the X17 Boson 12).
- It provides an adequate charge and particle identification because of its tracking capability and the presence of a magnetic field.

- It is quite insensitive to neutrons and gammas because of the absence of massive scintillators.

Clearly, the proposed detector is well suited also for proton beam experiments, such as the processes studied by the ATOMKI team. The scintillator bars on the other side must be properly coupled to the linear pixelated SiPM and these sensors need adequate readout to minimize the saturation caused by the gamma-flash and a fine characterization in order to use their response times.

2.1 μRWELL

The μRWELL is a recent gaseous detector of the Micro Pattern Gas Detector (MPGD) family [13, 14]; referring to Fig. 4 the μRWELL active volume between the cathode and the multiplication anode layer is filled by an appropriate gas mixture (e.g Ar(45%):CO2(15%):CF4(40%) or more traditional Ar(70%):CO2(30%)). The ionized electrons, drifting toward the anode thanks to an electric field of (few kV/cm), are multipled due to the intense electric field inside the well. The avalanche implies a sudden drop of the electric field inside the well for a time sufficiently long (proportional to the layer resistivity) to prevent self-sustaining discharges. Furthermore, the resistive layer is transparent to transient (avalanche) signals. In this way the signals can be picked-up by external readout electrodes (in our case, orthogonal strips with a pitch of 1.2 mm). The signals from the strip are currently collected by the APV25 based RD51/SRS electronics [15]. The APV25 stores the amplified charge every 25 ns (time sample) that can be readout by the SRS up to 27 consecutive samples, corresponding to a time window of $27 \times 25 = 675$ ns that can be used to reconstruct the track in Time Projection mode. When the μRWELL is invested by the intense gamma-flash, a significant amount of ionization is generated into the chamber gas that activates several strips as shown in the left plot of Fig. 5 which prevents a clean reconstruction. This gamma-flash effect is noticeable in the chamber up to about 2500 ns from its start; the right plot of Fig. 5 presents a typical event at 3000 ns from the start of the gamma-flash, with 5 strips above threshold which can be easily reconstructed. The test performed at the n_TOF has demonstrated that the gamma-flash do not saturate the APV25 electrons, as expected, but present a large, hardly manageable multiplicity of signals for about 1500 ns from its start.

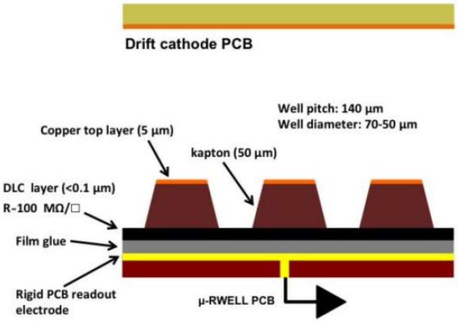

Figure 4: *Layout of the Resistive μRWELL*

2.2 Scintillator Bars and SiPM Characterization

A first characterization of the plastic scintillator bars has been conducted with the use of both SiPM (Hamamatsu S13363-3050NE-16) and more traditional multianod PMT (Hamamatsu H6568); the latter represents the reference optical sensors. Despite the well known disadvantages (larger dark current and

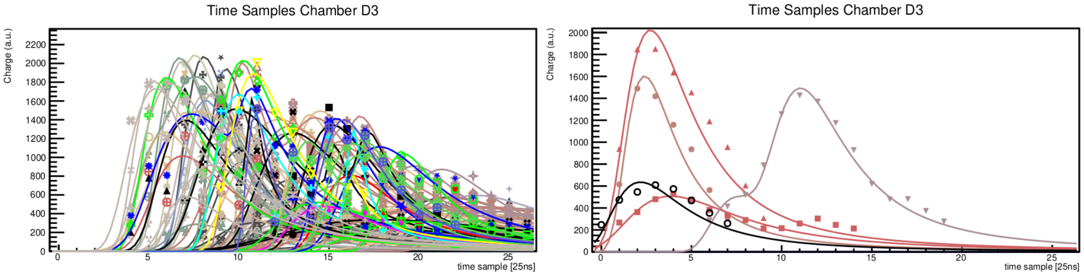

Figure 5: *Time evolution of charge collected from the μRWELL strips at different delay from the gamma-flash; left 0 delay, right 3000 ns delay. The x axis is the time sample of the APV25 in 25 ns unit. Each group of points with the same marker represents he cumulated signal on adjacent strips (cluster of strips); the corresponding curve is a fit of the sum of up to 3 Landau functions. The left plot shows the large signal multiplicity on the μRWELL due to the gamma-flash and the difficulty (impossibility) to clearly distinguish the different clusters.*

the more intricate signal evolution respect to PMT), the SiPM will be adopted in the final detector, being insensitive to the magnetic field and significantly more compact. The implemented configuration is schematically shown in Fig. 6. According to the depicted setup, two photomultiplier tubes (PMT's) have been fixed at the two ends of the bar with a ^{90}Sr radioactive source (electrons) located between them and acquired in different positions, representing the interaction point of the electrons along the bar. The formed coincidence of the signals between the two sensors provided the gate of a TDC (Time to Digit Converter) which measures the arrival times of the two signals; the difference between these two arrival times where collected for each source position, with adequate statistics. The same configuration and measurement has been repeated with PMT's replaced by the SiPM's. Both PMT and SiPM are coupled to the scintillator by a 1.5 mm layer of optical interface EJ-560 from Eljen Technology. The main goal was to compare the response of the SiPM's with PMT's and provide a first characterization of the thin scintillator bar. Fig. 7 reports the time propagation difference distributions for the PMT (left) and SiPM (right) with the radioactive source in the same position in the two configurations. The time difference resolution of about 1 ns corresponding to about 0.7 ns on the single sensor is slightly worse (7%) for the SiPM, but more than acceptable for the foreseen experiment. The plots of Fig. 8 have been produced from all measurements at different source positions; they permit to estimate the speed of light within the scintillator bar and from it the refractive index. These measurements, for both PMT and SiPM provide

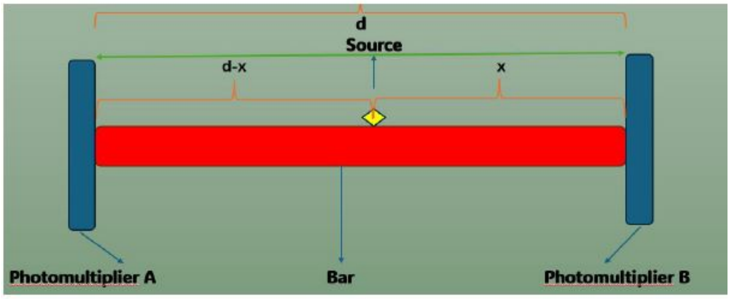

Figure 6: *Configuration of the experimental apparatus, where the scintillator bar ends are coupled to PMTs; the bar long surfaces are aluminized to internally reflect the light. Identical configuration for the SiPM. The length of the scintillator bar (d in fig) is 50 cm.*

very coherent results with a difference between the two determination below 1% in the direction of a substantial equivalence between the two sensors.

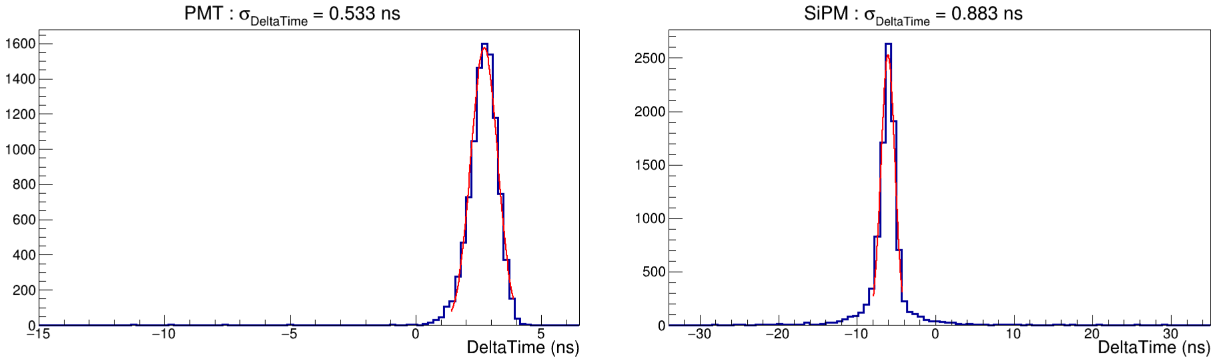

Figure 7: *Propagation time difference distributions for PMT (left) and SiPM (right) time responses with source at 6 cm from one end of the scintillator. The PMTs offer better time resolution than SiPMs; note the x axis ranges are different in the two plots.*

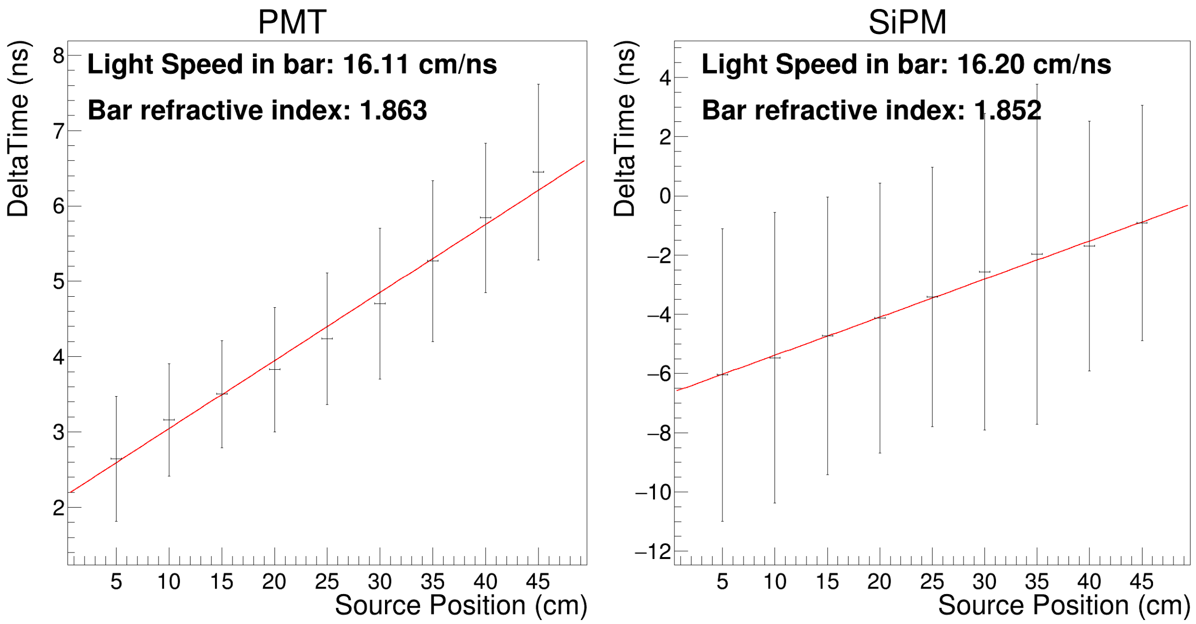

Figure 8: *Propagation time of the light within the scintillator measured by the time difference between the sensors at the two scintillator ends. The PMT configuration on the left plot and the SiPM configuration on the right plot. The error on DeltaTime is the RMS of the corresponding distributions, as in Fig. 7.*

3 Conclusions

Three anomalies have been recently observed in experiments performed at the 2 MeV accelerator of ATOMKI, Debrecen (Hungary). The anomaly consists in an excess of e$^+$e$^-$ pairs at large relative angle in the $^7Li(p, e^+e^-)^8Be$, and $^3H(p, e^+e^-)^4He$ nuclear reactions. These anomalies have been interpreted as the signature of a boson (called X17) with mass M_{X17}=17 MeV which could be a mediator of a fifth force. A complementary experiment has been proposed at the n_TOF facility and its experimental equipment is now under finalization, with state of the art sensors including μRWELL and SiPM coupled to thin scintillator bars. Preliminary characterizations and optimizations of the experimental components are ongoing with promising results.

References

1. W. Ni *et al*, Phys. Rev. Lett. 82 (1999), 2439-2442.
2. B. R. Heckel *et al*, Phys. Rev. Lett. 97 (2006), 021603 [arXiv:hep-ph/0606218].
3. A.J. Krasznahorkay *et al*, arXiv:2104.10075 [nucl-ex]
4. A.J. Krasznahorkay *et al*, Phys. Rev. Lett. 116, 042501 (2016)
5. A. J. Krasznahorkay *et al*, EPJ Web Conf. 137 (2017) 08010.
6. A. J. Krasznahorkay *et al*, PoS BORMIO 2017 (2017) 036.
7. A. J. Krasznahorkay *et al*, J. Phys. Conf. Ser. 1056 (2018) no.1, 012028.
8. A. J. Krasznahorkay *et al*, EPJ Web Conf. 142 (2017) 01019.
9. J. Guly-as *et al*, Nucl. Instrum. Meth. A 808 (2016) 21-28 [arXiv:nucl-ex/1504.00489].
10. n_TOF official web site: https://ntof-exp.web.cern.ch/
11. A. J. Krasznahorkay *et al*, arXiv:1910.10459 [nucl-ex].
12. M. Viviani, *et al*, PRC 105, 014001 (2022).
13. G. Bencivenni *et al*, 2015 JINST 10 P02008.
14. G. Bencivenni *et al*, submitted to Nucl. Instrum. Meth. A (2017).
15. L. Jones, "APV25-S1 User Guide", Verison 2.2, Sep. 2001
    S. Martoiu, et al. J. Instrum. 8 (03) (2013) C03015
16. V.V. Parkhomchuck et al, Nucl. Instrum. Meth. 93 (1971) 269.
17. R. Santonico et al, Nucl. Instrum. Meth. A 187 (1981) 377.
18. M. Anelli *et al*, Nucl. Instrum. Meth. A 300 (1991) 572.

Frascati Physics Series Vol. 76 (2024)
8TH YOUNG RESEARCHERS' WORKSHOP 'PHYSICS CHALLENGES IN THE LHC ERA'
May 13 and 16, 2024

MACHINE LEARNING TECHNIQUES FOR FOUR TOP FINAL STATES EXTRACTION

Cristina Giordano
Institute of High Energy Physics (HEPHY), Austrian Academy Of Sciences (ÖAW),
Technical University of Vienna (TUW), Vienna, Austria

Abstract

The four top discovery reported by both ATLAS and CMS in 2023 represents another confirmation of the Standard Model of particle physics and a possible gateway to physics beyond Standard Model. Because of the high top multiplicity, this rare phenomenon branches out in many final states; one of the channels not included in the observation papers was the final state denoted by the case in which a top and an anti-top decay leptonically, resulting in two leptons having opposite signs (2LOS). The main hardship of this channel is due to the inextricable relation to its main backgrounds, in particular the simultaneous production of a top-antitop pair, commonly referred as $t\bar{t}$. The strategy and development status for a top-tagging approach targeting four top final state in 2LOS is presented.

1 Introduction

The observation of the production of four top quarks, claimed by both ATLAS 1) and CMS 2) in 2023, was an important milestone in understanding the Standard Model (SM) of particle physics, the current best description of three out of the four known fundamental interactions, namely the electromagnetic, the strong and the weak forces.

The SM has a high level of predictivity, and it has been extensively experimentally verified with high precision, and all particles included in its framework have been observed, the last one being the Higgs boson whose discovery was reported by both ATLAS and CMS at the Large Hadron Collider (LHC) in 2012. However, the SM is incomplete, for it does not explain many phenomena, like the existence of Dark Matter and Dark Energy, neutrino masses, the matter-antimatter asymmetry and so on. Many theories Beyond the SM (BSM) have been formulated in order to overcome these shortcomings, and the four top final states is considered in many of these as a promising signature to probe them: this measurement of this production process is statistically limited, it has a distinctive signature, it is sensitive to the top-Higgs

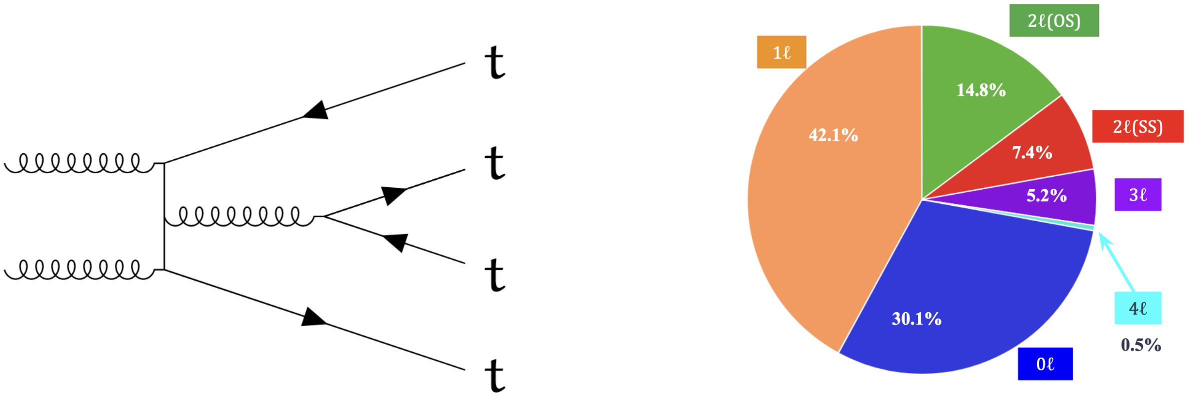

(a) (b)

Figure 1: On the left, an example of a Feynman diagram contributing to four quark production. On the right, pie chart representing the possible final states for four top production: all hadronic decay ($0L$); with one, three or four charged leptons ($1L$, $3L$, $4L$) with two charged leptons of opposite ($2LOS$) or same signs ($2LSS$).

Yukawa coupling and many top-philic heavy resonances, and holds a unique sensitivity to four fermions operators in the context of SM Effective Field Theory (SMEFT). Because of the large number of top quarks being produced, it has many final states with very different branching ratios, as shown in Figure 1. Over the years, many searches across many channels have been performed by both ATLAS 3, 4) and CMS 5, 8). The $2LOS$ final state is one of the most challenging, because it is heavily affected by its main irreducibile background, the production of a top-antitop pair, commonly referred as $t\bar{t}$; in particular, when additional jets are present in the final state, this background process can easily emulate the four top quarks signal, as shown in Figure 2. In the following sections, a Machine Learning approach to

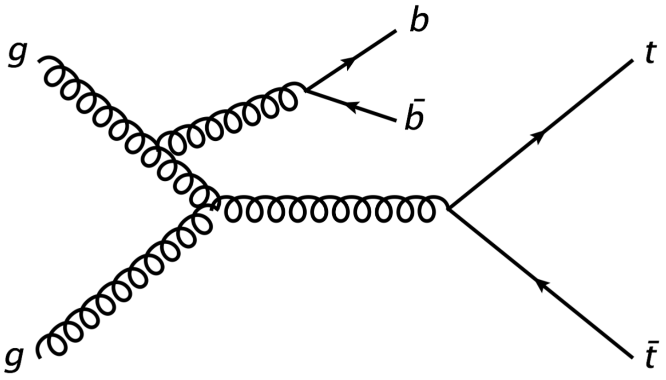

Figure 2: Feynman diagram of the $t\bar{t} + jets$ process, in which the additional jets are coming from the hadronization of 2 bottom quarks.

extract the signal is presented. Two different techniques are described: a Neural Network (NN) trained on event-level information, and an object-level top-tagging approach.

2 Machine Learning approach

This section concerns the use of ML performed to separate the four top signal from the backgrounds in the $2LOS$ final state. NNs are currently being used in two ways: an event-level Multivariate Analysis algorithm (MVA) in order to discriminate the four top signal from the $t\bar{t}$ background by evaluating the information extracted by numerous input features at once; a resolved hadronic top tagger used to gain information on the hadronic component of top quarks present in the signal.

2.1 Event-level MVA

As main background sample, a $t\bar{t}+jets$ is used, and it is separated into different categories according to the flavour of the jets, that is the type of quark that initiated the jet. The NN architecture consists of an input layer, a normalization layer, and 2 dense hidden layers. The output layer is tailored to the regression task, so that the number of outputs corresponds to the number of classes in the training data, namely $t\bar{t}t\bar{t}$, $t\bar{t}b\bar{b}$, $t\bar{t}c\bar{c}$, $t\bar{t}light$. The aim of the network is to classify input data into one of these categories, and to predict the probability of each class. A feedforward NN is built using the Keras [6] package; the number of neurons of the first layer is determined by the number of input features. The first hidden layer has 94 neurons, and the second has 53, in accordance to one of the standard design choices for NNs ($N_{input}*2/N_{input}+5$). The two hidden layers and the output layer of the NN use the sigmoid activation function:

$$\sigma(x)=\frac{1}{1+e^{-x}} \tag{1}$$

In order to minimize the categorical cross-entropy loss function:

$$CE=-\frac{1}{n}\sum_{i}y_i\log(\hat{y}_i(x;\theta)) \tag{2}$$

in which x represents the input feature vector, y_i the target values, $\hat{y}$ the predicted values, and θ the model parameters, the Adam optimizer is used [7]. The training is performed by using 80% of the total dataset, while the remaining 20% is used for the testing process. Table 1 shows the number of entries used during the training. The input features comprehend the kinematic properties of the jets, b-jets, and leptons, the b-tagging scores of the jets, the separations between leptons and/or jets, H_T, and invariant masses and transverse masses of pairs of leptons/jets coming from top quark decays. The model has an early stopping mechanism monitoring the loss over the training; if the loss does not improve for 3 consecutive epochs the training is stopped in order to prevent overfitting and save computational resources. Fig. 3 shows Receiver Operating Characteristic (ROC) curves for each output and their relative area under the ROC curve (AUC) for an inclusive opposite-sign dilepton "signal-like" selection, namely off the Z peak, 4+ jets and 2+ b-tagged jets and a 500 GeV H_T cut.

Category	**Count**
$t\bar{t}t\bar{t}$	1292052
$t\bar{t}light$	890844
$t\bar{t}c\bar{c}$	255187
$t\bar{t}b\bar{b}$	97361

Table 1: Number of entries for each sample.

Furthermore, a Long Short Term Memory layer (LSTM) [9] was added as a strategy to improve the discriminating power of the algorithm. This layer feeds jet features input during the training, in order

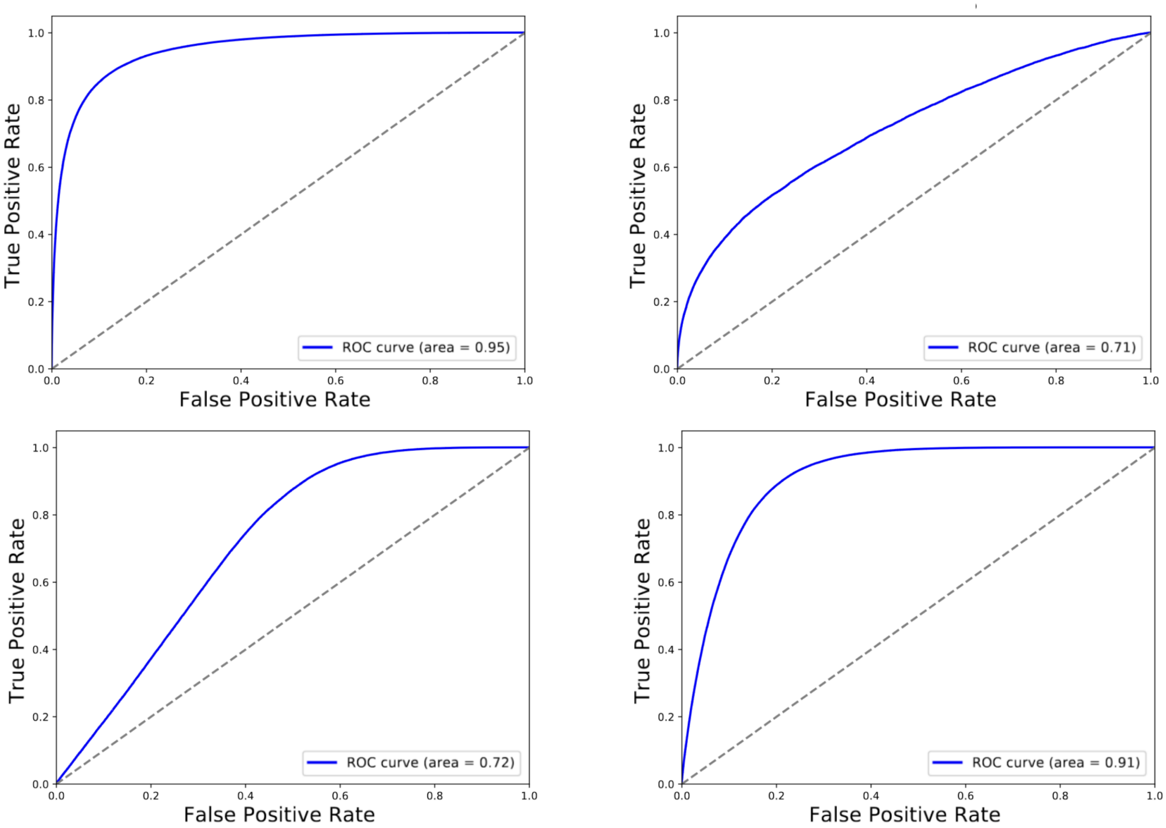

Figure 3: ROC curves for the 4 sample categories; as expected, the score is higher for those categories having a higher number of entries (tttt and ttlight), while the score is relatively low/ biased for the other two

to learn long-term dependencies between the steps; this procedure addresses the recurring problem of vanishing gradients in traditional NNs. The improvement obtained can be seen in Fig.5 . However, in order to extract more information on the hadronic component of the four top process, historically more challenging, a tagging-like strategy is being developed.

2.2 Resolved top tagger

The hadronic top reconstruction was performed for the *resolved* configuration, in which each of the jets (1 b-jet, 2 light jets) emerging from the top quark is matched (or not) to generator level particles. Each triplet of jets that has a match for each and ever one of its components is flagged as a *True* top quark (aka Class 1); on the other hand, those triplets where at least one of the jets is not matched to generator level quarks are flagged as *False* (Class 0). A jet is considered *matched* if the angular distance between the RECO jet and the GenPart quark is below 0.4, namely $\Delta R(j,q) < 0.4$. Two of the most relevant input features to the classifier are shown in Figure 7.

The architecture of the network consists of 2 dense layers with 64 and 32 neurons respectively, that use the ReLU (Rectified Linear Unit) activation function, separated by a Dropout layer, that sets 20% of units to 0 in order to prevent overfitting, and an output layer that uses the Adam optimizer to minimize the binary cross entropy. The input features are standardised using the Robust Scaler from scikit-learn **?**);

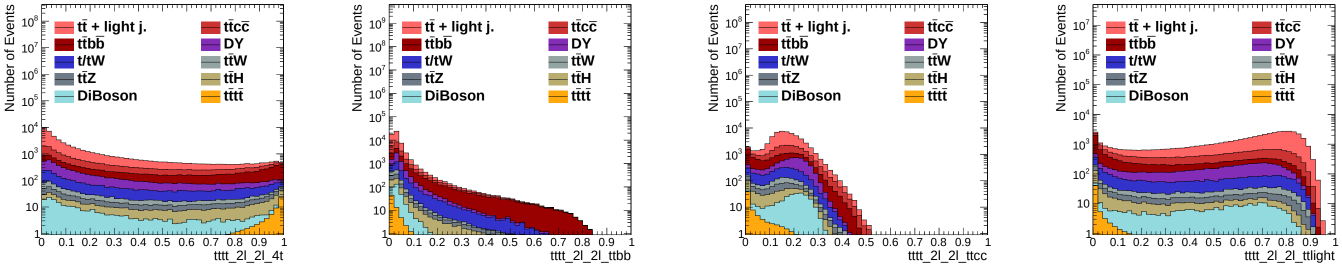

Figure 4: Scores of the event-level MVA for the four classes.

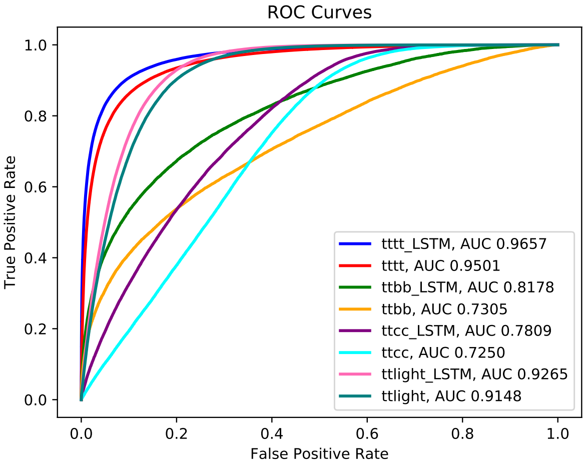

Figure 5: ROCs and AUCs comparisons of the two models (baseline and with the addition of an LSTM layer) for all the categories. The improvement due to the LSTM can be mainly see in the ttbb category.

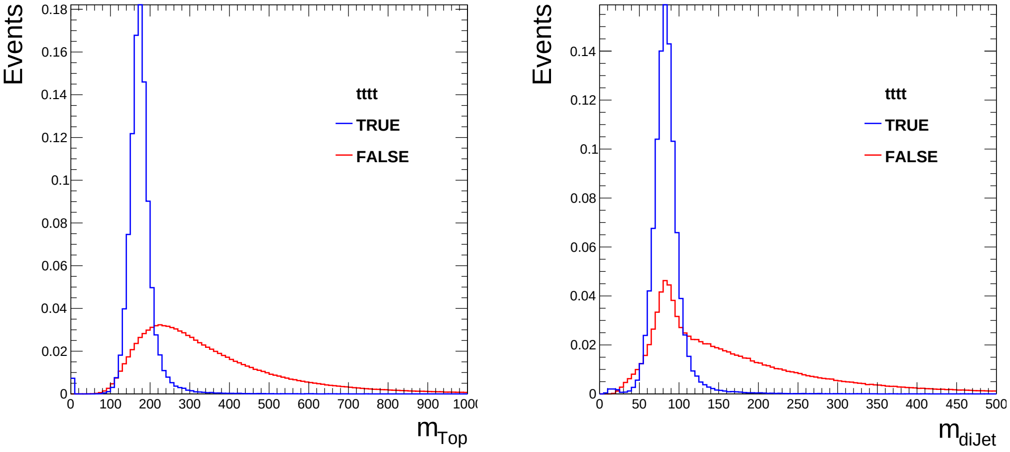

Figure 6: Some input features for the True and Fake top quark categories.

these include the most important kinematic variables for the reconstructed triplets, the W-boson system (i.e. the subsystem reconstructed with the two light jets), the single sub-jets included in the triplets, invariant masses of the many dijet systems, angular separations, and the transverse momentum of the three jets in the top quark centre-of-mass frame. The training was performed with a dataset of 260K entries, equally split between signal and background, obtained from a 2017 four top sample.

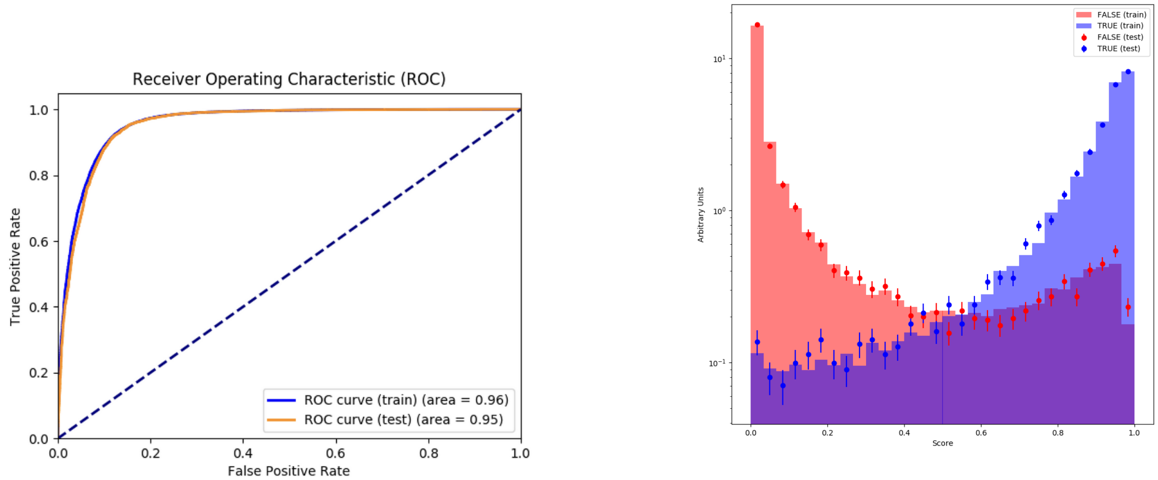

(a) ROC curve for the binary classification of true vs false top quarks

(b) NN score for the signal and background categories

Figure 7: On the left, the ROC AUC scores for the training and test sets, both showing a good behaviour in terms of binary classification; on the right, the score distribution for the two classes; blue represents the signal, while represents the combinatorial background from non-matched triplets.

These studies on this resolved objects seem promising, and the efforts in order to understand how to perform the extraction from the $t\bar{t}$ background are ongoing.

References

1. ATLAS Collaboration, Observation of four-top-quark production in the multilepton final state with the ATLAS detector, Eur. Phys. J. C 83 (2023) 496
2. CMS Collaboration, Observation of four top quark production in proton-proton collisions at $\sqrt{s} = 13$ TeV, Phys. Lett. B 847 (2023) 138290
3. ATLAS Collaboration, Measurement of the tt¯tt¯ production cross section in pp collisions at $\sqrt{s} =$ 13 TeV with the ATLAS detector, JHEP 11 (2021) 118
4. ATLAS Collaboration, Evidence for $t\bar{t}t\bar{t}$ production in the multilepton final state in proton-proton collisions at $\sqrt{s} = 13$ TeV with the ATLAS detector, Eur. Phys. J. C 80 (2020) 1085
5. CMS Collaboration, Evidence for four-top quark production in proton-proton collisions at $\sqrt{s} = 13$ TeV, Phys. Lett. B 844 (2023) 138076
6. Chollet F. et al, Keras, https://github.com/fchollet/keras

7. D. P. Kingma et al., Adam: A Method for Stochastic Optimization, arXiv:1412.6980

8. CMS Collaboration, Search for the production of four top quarks in the single-lepton and opposite-sign dilepton final states in proton-proton collisions at $\sqrt{s} = 13$ TeV, JHEP 11 (2019) 082

9. Hochreiter, S. and Schmidhuber, J.,Long short-term memory, Neural Computing, Vol.9, 1997

Frascati Physics Series Vol. 76 (2024)
8TH YOUNG RESEARCHERS' WORKSHOP 'PHYSICS CHALLENGES IN THE LHC ERA'
May 13 and 16, 2024

SEARCH FOR SIGNATURES OF A NEW NEUTRAL SCALAR IN THE W^+W^- CHANNEL WITH SEMI-LEPTONIC FINAL STATES AT THE LHC

Olimpia Miniati and Stefania De Curtis
Dipartimento di Fisica e Astronomia, Università degli Studi di Firenze, and INFN Sezione di Firenze
Via G. Sansone, 1 - 50019 Sesto Fiorentino (FI)

Abstract

The Standard Model is the theoretical scheme currently adopted for the description of the fundamental interactions. Nevertheless, the desire to achieve a more complete formulation of nature, in which the Standard Model can be embedded, is driven by the presence of observational evidence that is unexplainable within the Standard Model description. Our purpose is to illustrate a method to conduct a phenomenological investigation regarding the existence of an enlarged Higgs sector. The beyond Standard Model contributions that will be considered arise from the presence of an extra scalar, CP-even and heavier with respect to the particle that has been discovered in 2012. The theoretical scheme in which the analysis will be embedded is the Singlet Extension, and the decay channel that will be taken into account will be the W^+W^- with semi-leptonic final states. The possibility of having visible signatures at the LHC will be discussed.

1 Introduction

The Standard Model (SM) has been experimentally proved to be the most successful framework to describe in a unified way the electromagnetic and weak interactions. An important ingredient of such model is the Brout–Englert–Higgs (BEH) mass generation mechanism 1, 2), which predicts the presence of a fundamental massive spin-zero particle in the theory spectrum whose characteristics are compatible with the particle discovered on 2012 by the CMS and ATLAS collaborations at the Large Hadron Collider (LHC) 3, 4). Nevertheless, the currently available measurements for such particle's interactions, both with the SM matter and with itself, are not sufficiently precise to fully validate the SM BEH prediction. This experimental status, along with the presence of physics phenomena that cannot be described in the SM, leave open access to Beyond Standard Model (BSM) theories. Among the physically motivated BSM frameworks that have been proposed, some of them include an enlargement of the Higgs sector.

In the context of New Physics (NP) investigations, phenomenological analyses are of primary importance as they operate as intermediary between the theoretical framework and the experimental measurements by studying how the BSM signals would appear in the detectors. For theories where the new physics contributions arise at the electroweak scale or higher ones, the environment where experimental tests are mainly carried out are the colliders. To perform accurate phenomenological analyses, the high energy physics community relies on the employment of events generators, such as MadGraph5_aMC@NLO 5, 6), that provide the access to the kinematic information of the initial particles and the final products.

The purpose of this phenomenological study is to present a method for the investigation regarding the possible signatures coming from an enlarged Higgs sector that can manifest themselves at the LHC. The NP contribution considered is due to the presence of an extra scalar S, heavier with respect to the 125 GeV particle. The channel exploited for the analysis is the W^+W^- channel with semi-leptonic final states. This scenario was selected because the CMS collaboration observed an upward fluctuation of data compared with the expected background in the search for a high mass Higgs-like scalar boson decaying into a pair of W bosons with fully-leptonic final states 7). This excess has to be confirmed by the new analyses, including those in the same channel with semi-leptonic final states here taken into account.

2 Lagrangian for the enlarged Higgs sector

To consider general models that extend the SM description including the presence of at least one extra scalar in the Higgs sector, the SM Lagrangian must be modified. In particular, we have considered the modifications as additive to the SM, and separated them in two different contributions, as described by the following equations.

$$\mathcal{L}_{BSM} = \mathcal{L}_{SM} + \mathcal{L}_S + \mathcal{L}_{hMOD} \tag{1}$$

$$\begin{aligned}\mathcal{L}_S \;=\; & \frac{1}{2}\partial_\mu S \partial^\mu S \;-\; \frac{1}{2}M_S^2 S^2 \;+\; \frac{2m_W^2}{v}(k_{sww})SW_\mu^+W_-^\mu \;+\; \frac{m_W^2}{v\ cos^2\theta_w}(k_{szz})SZ_\mu Z^\mu + \\ & + \; k_{stt}\ S\bar{t}t \;+\; k_{sbb}\ S\bar{b}b \;+ k_{s\tau\tau}\ S\bar{\tau}\tau \;+ ...\end{aligned} \tag{2}$$

$$\mathcal{L}_{hMOD} = \frac{2m_W^2}{v}(k_{hww})hW_\mu^+W_-^\mu \;+\; \frac{m_W^2}{v\ cos\theta_w^2}(k_{hzz})hZ_\mu Z^\mu - \frac{k_{htt}}{\sqrt{2}}\ h\bar{t}t - \frac{k_{hbb}}{\sqrt{2}}\ h\bar{b}b + ... \tag{3}$$

The term $\mathcal{L}_S$ describes the dynamic and the interactions for the new scalar S, which is a colourless and electromagnetically neutral particle with mass M_S. In equation 2 are reported the terms that allow to describe the two production mechanisms for the extra scalar that are assumed to be the dominant ones, *i.e.* the Gluon Gluon Fusion (GGF) and Vector Boson Fusion (VBF), as well as all the possible leading order two-body decays. Different normalizations for the various couplings have been assumed, for example the vertices involving two massive gauge bosons have been normalized to the SM value for the Higgs' interaction.

The following term, $\mathcal{L}_{hMOD}$, is necessary to describe scenarios where the couplings for the Higgs particle (h) are different with respect to the SM predictions, as occurs when there is a mixing between the interaction eigenstates in the scalar sector. The BSM parameters entering the Lagrangian $\mathcal{L}_{BSM}$, namely the mass for the extra scalar and all the couplings for the vertices in equations 2-3, have been defined to be free and independent. This choice was performed to allow the usage of the aforementioned Lagrangian to describe various BSM scenarios with at least one extra scalar, each of which with a different internal dependence among the free parameters that must be properly stated before the analysis. This procedure will be adopted in section 4, performing the analysis for the Singlet Extension.

The structure of the BSM Lagrangian in equations 1-3 was implemented [1] also in the input file for the event generator, encoded in the *Universal FeynRules Output* (UFO) format 8). Moreover, a peculiar labelling for the BSM interaction vertices allowed us to exploit the Lagrangian to obtain a set of simulated events separately for the signal and the background contributions, as well as to deconstruct the interference contributions between the signal and the SM background, as shown in the following section.

3 SM-like high mass scalar resonance

As illustrative example, we consider a scenario where the two scalars S, h have both SM-like couplings, *i.e.* whose strength is fixed to the value predicted for the SM Higgs. Therefore, the only NP source is represented by the presence of the S particle. It is important to underline that this scenario represents a preliminary test for the analysis procedure that can be used for general BSM frameworks.

Fixing the mass of the extra scalar S to $M_S = 600\text{GeV}$, we checked that the dominant production mechanism is the GGF, so that, in first approximation, we can consider only this one. Therefore, we analysed the behaviour of the signal events, represented by those that have been mediated by an exchange of the S particle in the s-channel, produced via a virtual loop of quarks, and that decays in a couple of W bosons.

Keeping the same initial and final states, *i.e.* two incoming gluons (g) and semi-leptonic final states ($l\nu qq'$) resulting from the decay of a couple of W bosons respectively, our setup allows us to take into account the interference of the signal diagrams with the SM loop-induced source of background in the W^+W^- channel (*Interference s-B*). This contribution can be separated in the interference between signal diagrams and those involving a SM Higgs h exchange (*Interference s-h*) and in the interference between signal diagrams and the loop-induced SM background in the W^+W^- channel without the contributions involving a SM Higgs h exchange (*Interference s-b*). Some of the diagrams involved in the signal and interference contributions for the scattering processes of interest are shown in figure 1.

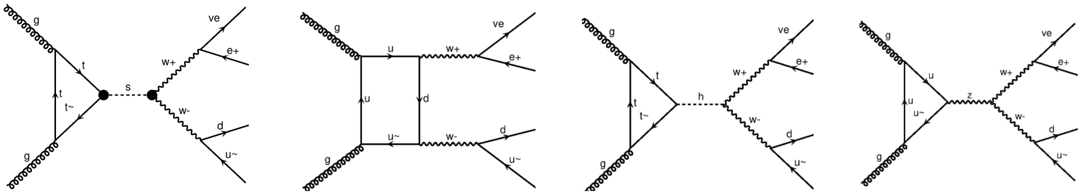

(a) (b) (c) (d)

Figure 1: *Example of a signal diagram* (a), *where the NP vertices are marked with a black dot, and some SM background diagrams at loop-level in the* W^+W^- *channel* (b)-(d).

In figure 2 the signal and interference contributions to the cross section $\sigma(gg \to W^+W^- \to l\nu qq')$ are shown. Here we plot the invariant mass distributions for the four parton-level final products. The simulations were performed mimicking LHC collisions occurring at a $\sqrt{s} = 13$ TeV center of mass energy and the integrated luminosity assumed was 35.9 fb^{-1}: those characteristics are intended to recreate the set of data collected by the CMS collaboration at the LHC during Run-2 in 2016. Moreover, for the W decaying leptonically, we considered only the products coming from the first and second generation.

---

[1] by L. Panizzi (private communication).

The results are obtained assuming two different widths for the extra scalar $\Gamma_S = 300, 400$ GeV. The scenario where the width exceeds the value predicted for SM-like couplings and a mass of $M_S = 600$GeV takes in account, for example, the presence of other BSM particles as possible decay products for S, that will increase its decay probability and, consequently, its width. We see that the two decomposed interference contributions s-h, s-b have a similar behaviour with an opposite sign, switching respectively from destructive to constructive and vice versa. This evolution occurs in correspondence of the scalar S pole mass value. Their combined result is summed to a total constructive contribution s-B.

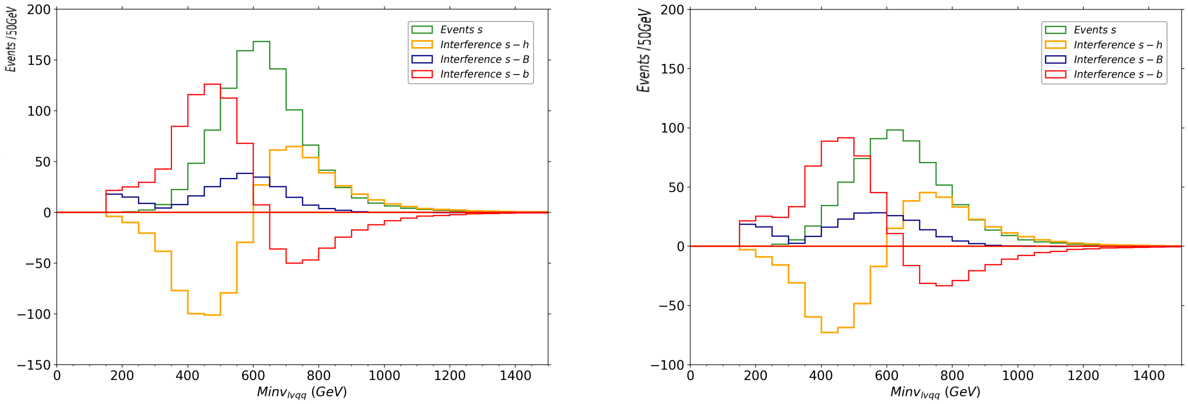

(a) $\Gamma_S = 300$ GeV

(b) $\Gamma_S = 400$ GeV

Figure 2: *GGF parton-level invariant mass distributions for signal events (s) and the various interference contributions: with the SM Higgs in the W^+W^- channel (s-h, yellow), with the SM one-loop background in the W^+W^- channel (s-B, blue) and with SM one-loop background in the W^+W^- channel without the h contributions (s-b, red). Here M_S=600 GeV and Γ_S=300,400 GeV.*

The capability of this deconstructing mechanism, here briefly illustrated, will be fruitful in scenarios where there are different signal contributions. In fact, it will allow to study both the interference between the various source of signal as well as with the SM background.

4 Test of the Singlet Extension

One of the most simple BSM frameworks describing an extra scalar whose parameter space is still partially available is undoubtedly the Singlet Extension (SE) 10, 11).

In this model a new scalar σ, singlet under the gauge interactions, is added to the Lagrangian. It interacts exclusively with the SM Higgs doublet (Φ) through a scalar potential $V(\Phi, \sigma)$. Assuming the presence of an additional $\mathbb{Z}_2$ symmetry which is spontaneously broken by the singlet, the Lagrangian for the Higgs sector is:

$$\mathcal{L}_{Higgs} = (D^\mu \Phi)^\dagger (D_\mu \Phi) + \partial^\mu \sigma \partial_\mu \sigma - V(\Phi, \sigma), \tag{4}$$

$$V(\Phi, \sigma) = -m^2 \Phi^\dagger \Phi - \mu^2 \sigma^2 + \lambda_1 (\Phi^\dagger \Phi)^2 + \lambda_2 \sigma^4 + \lambda_3 \Phi^\dagger \Phi \sigma^2. \tag{5}$$

In the scenario were both the doublet and the singlet acquire a non-zero Vacuum Expectation Value (VEV), defined as $v \sim 246$GeV for the doublet and a free-valued v_s for the singlet, their expression in the unitary gauge is:

$$\Phi = \begin{pmatrix} 0 \\ \frac{\phi_0+v}{\sqrt{2}} \end{pmatrix} \qquad \sigma = \frac{\phi_s + v_s}{\sqrt{2}}. \tag{6}$$

The diagonalization of the squared mass matrix arising from the potential in equation 5 allows the identification of the mass eigenstates $(h,\ S)$ that are obtainable from the gauge eigenstates (ϕ_0, ϕ_s) through a rotation matrix defined by the mixing angle α, satisfying the relation:

$$\phi_0 = \cos\alpha\ h + \sin\alpha\ S. \tag{7}$$

The hierarchy between the physical masses is $m_h^2 \leq M_S^2$, and the the picture where h represents the discovered LHC particle, which we will adopt for the following discussion, corresponds to the *small mixing angle scenario* ($\sin\alpha \to 0$). From equation 7 it is also possible to describe the interactions with the SM particles that the two mass eigenstates will inherit from the gauge eigenstate ϕ_0: the strength for each coupling involving one $h(S)$ field will be suppressed with respect to the SM value by a factor $\cos\alpha(\sin\alpha)$. Therefore, the majority of the BSM coupling won't be all independent, being a combined function of the SM value and the mixing angle.

This framework can be tested with our previously described method. Fixing the values for m_h and v, the SE free parameters are only three 11): the mixing angle α, the ratio between the VEVs $\tan\beta = v/v_s$ and the mass of the heavy scalar M_S. To consider a BSM theory as a viable candidate to describe the fundamental interactions some theoretical and experimental bounds must be satisfied, and this constrains the possible values for the free parameters of the theory. For the SE, the bounds that must be satisfied are:

- Perturbativity of the couplings entering the scalar potential, tree-level perturbative unitarity for 2→2 scattering processes and condition for the scalar potential to be bounded from below 11);
- Compatibility of the loop corrections to the gauge bosons' vacuum polarization with the current measured values for the electroweak precision observables (EWPO).
- Compatibility of the SE signal predictions with the exclusion limits resulting from additional scalar searches carried out at colliders and with the measurements of the 125 GeV Higgs properties. Those can be tested using the public code `HiggsTools` 15).

The resulting parameter space is quite constrained, in particular only small values for $\sin\alpha$ are allowed. This is justified by the current measured precision for the interaction strengths of the LHC Higgs with a couple of massive vector bosons. For the SE those measurements constraint $\cos\alpha$ according to equation 7 and, consequently, the value of $\sin\alpha$.

For example, some allowed values are $\sin\alpha = 0.1$, $\tan\beta = 0.1$ and four different mass hypotheses $M_S = 200, 650, 1000, 1500$ GeV. For those scenarios, the expected distributions for the NP signal can be studied, defining it to be generated by all the diagrams mediated by an s-channel exchange of the S particle produced via GGF [2]. To investigate the presence of visible signatures of those processes, we can compare the number of signal events expected for each invariant mass value with the number of events expected for the SM background. In the following discussion the results will be presented for a parton-level analysis, with the invariant mass defined by the kinematics of the four semi-leptonic final

---

[2] The GGF is the dominant production mechanism at least for $M_S = 200, 650$ GeV.

products, as shown in figure 3. The plots have been obtained simulating the Run-2 LHC configuration, assuming a center of mass energy of $\sqrt{s} = 13$ TeV and an integrated luminosity of $\mathrm{L}_{int} = 160\ \mathrm{fb}^{-1}$. The width Γ_S was evaluated summing all the contributions of the accessible two-body decays.

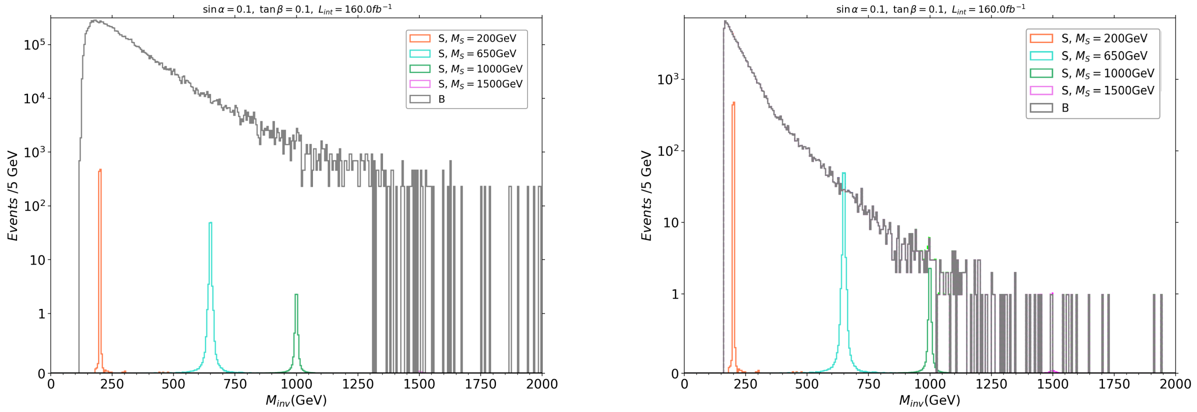

(a) *Background SM tree-level*

(b) *Background SM loop-induced (W^+W^- channel)*

Figure 3: *Number of events expected for signal (S) and SM background (B) for* $\sin\alpha = 0.1$, $\tan\beta = 0.1$ *and various mass hypotheses, for two sources of SM background.*

The main source of background assuming the same initial (gg) and final states ($l\nu qq'$) is the one that originates from the tree-level contribution ((a) in figure 3), and that has a cross section that is at least four order of magnitude higher with respect to the signal ones. We can see that in absence of specific cuts that are able to lower partially those background contributions - such as requiring that the invariant mass of the two jets lies around the W mass - the possibility to have an evidence of the signal contributions is absent.

Another source of background, that is obtainable with a different simulation, is the loop induced one in the W^+W^- channel, ((b) in figure 3, presented in scale with signal events). This contribution will be fundamental for the analysis only if the cuts on the tree-level source will be able to lower its number of expected events of at least two order of magnitude. With the current setup, the possibility to prove the Singlet Extension in the W^+W^- channel with semi-leptonic final states appears to be a challenging task for the signal hypotheses here tested, also after the High Luminosity phase of the LHC.

5 Conclusions

We have described a general approach to perform phenomenological studies of BSM signatures arising at the LHC in the W^+W^- channel with semi-leptonic final states due to the presence of an enlarged Higgs sector comprising one extra scalar that can be produced via GGF and VBF. We illustrated two scenarios for the study of the signal, interference and background events: the analysis of general models, where the two scalars in the Higgs sector have SM-like couplings, and the analysis of some viable configurations for the Singlet Extension scheme. Both the analyses were based on parton-level results and on the assumption of GGF production mechanism for the new particle. For the first scenario, we illustrated how it is possible to deconstruct the interference contributions between the signal and the SM background in order to separately study their impact. For the second analysis, we discussed the possibility of identifying some BSM signatures in the differential distribution of the invariant mass of the decay products. This appears to be a challenging task. Nevertheless, to understand definitely whether it is possible to test the SE framework with this methodology, some additional analyses must be performed, taking into account the interference contributions, the VBF production scenario for the extra scalar and the impact of the cuts on the SM background.

Acknowledgements

This paper collects some results obtained during the studies I performed for my master's thesis, realized under the supervision of Stefania De Curtis and with the precious collaboration of Luca Panizzi.

References

1. P.W. Higgs, Phys. Rev. Lett. **13**, 508–509 (1964).
2. F. Englert *et* R. Brout, Phys.Rev. Lett. **13**,321–323(1964).
3. ATLAS Collaboration, Phys.Lett. B **716**,1-29(2012).
4. CMS Collaboration, Phys. Lett. B **716**, 30(2012).
5. J. Alwall *et al*, JHEP **07**, 1-157(2014).
6. V.Hirschib *et al*, JHEP **10**, 1-34(2015).
7. CMS collaboration, CMS-PAS-HIG-20-016 (2022).
8. C. Degrande *et al*, Comput.Phys.Commun. **183**, 1201-1214(2012).
9. N. Christensen *et al*, feynrules.phys.ucl.ac.be (2014).
10. V. Barger *et al*, Physical Review D **77(3)** (2008).
11. T. Robens *et al*, The European Physical Journal C **75(3)**, 104 (2015).
12. M. E. Peskin *et al*, Phys. Rev. D **46**, 381(1992).
13. A. Beniwal *et al*, JHEP **2**, 1-43(2019).
14. S. Navas *et al*, Phys. Rev. D **110**,(2024).
15. H. Bahl *et al*, Computer Physics Communications **291**, 108803, (2023)

Frascati Physics Series Vol. 76 (2024)
8th young researchers' workshop 'Physics Challenges in the LHC Era'
May 13 and 16, 2024

Measurement of the CP properties and anomalous couplings of the Higgs boson with the CMS experiment

F. De Riggi on behalf of the CMS Collaboration
INFN, Sezione di Roma - Roma, Italy
Dipartimento di Fisica, Sapienza Università di Roma - Roma, Italy

Abstract

In many beyond the Standard Model (BSM) theories, anomalous couplings of the Higgs boson with the W and Z vector bosons, or with fermions, are possible and can potentially violate CP symmetry. BSM couplings between the Higgs boson and the top quark, as well as with particles not yet observed, could generate CP violation in the interactions between the Higgs boson and gluons, the dominant process in production at the LHC. Studies of CP violation and anomalous couplings of the Higgs boson to vector bosons (HVV) and fermions (Hff) conducted by the CMS experiment, utilizing the complete Run 2 datasets, are presented. We focus on measurements where the Higgs boson is produced on-shell. The data corresponds to an integrated luminosity of 138 fb^{-1} at a proton-proton collision energy of 13 TeV. The kinematic distributions of the final states are sensitive to the Higgs boson's quantum numbers, and various production and decay channels are used for these studies. Matrix element techniques and multivariate algorithms are employed to identify the production mechanisms and enhance sensitivity to the Higgs boson's tensor structure in the interactions.

1 Introduction

The discovery of the Higgs boson (H) by the ATLAS 1) and CMS 2, 3) experiments at the LHC has opened a new era for particle physics, where the characterization of this new boson is of crucial importance. The H boson serves both as a test of the Standard Model (SM) and as a gateway to exploring new physics. The properties of the H boson have been found to be consistent with those of the SM Higgs boson. In particular, non-zero spin assignments for the H boson have been excluded, and its spin-parity quantum numbers are consistent with what predicted by the SM $J^{PC} = 0^{++}$. However, the limited precision of current studies still allows for small anomalous couplings of the H boson to two electroweak gauge bosons (HVV). These couplings are expected to be suppressed by loop effects and therefore to be relatively small. On the other hand, anomalous Higgs boson couplings to fermions, which might also indicate CP violation, may appear at tree level and may not suffer from loop suppression. To fully exploit different possible deviations from the SM expectation that may arise in different couplings, it is essential to study the various decay and production channels of the Higgs boson.

2 Phenomenology of the CP structure in HVV and Hff interaction vertices

The most general form of the scattering amplitude between a spin-0 H boson with two spin-1 gauge bosons VV, is parametrized with three tensor structures and expansion of coefficients up to (q^2/Λ_1^2)

$$A(HVV) \sim \left[a_1^{VV} + \frac{k_1^{VV} q_1^2 + k_2^{VV} q_2^2}{(\Lambda_1^{VV})^2} \right] m_{V1}^2 \epsilon_{V1}^* \epsilon_{V2}^* + a_2^{VV} f_{\mu\nu}^{*(1)} f^{*(2)\mu\nu} + a_3^{VV} f_{\mu\nu}^{*(1)} \tilde{f}^{*(2)\mu\nu} \tag{1}$$

where q_i, ϵ_{Vi}, and m_{V1} are the 4-momentum, polarization vector, and the mass of the vector boson, indexed by i = 1, 2. $f^{(i)\mu\nu} = \epsilon_{Vi}^{\mu} q_i^{\nu} - \epsilon_{Vi}^{\nu} q_i^{\mu}$ is the gauge boson's field strength tensor and $\tilde{f}_{\mu\nu}^{i} = (1/2)\epsilon_{\mu\nu\rho\sigma} f^{(i)\rho\sigma}$ is the dual field strength tensor defined using the Levi-Civita symbol in four dimension ($\epsilon_{\mu\nu\rho\sigma}$). a_i^{VV} are the coupling coefficients. $k_i^{VV}/(\Lambda_1^{VV})^2$ multiply the next term in the q^2 expansion. Λ_1 is the scale of beyond the SM (BSM) physics.

In Eq. 1, the only nonzero SM contributions at tree level are a_1^{WW} and a_1^{ZZ}. All other ZZ and WW couplings are considered anomalous contributions, which are either due to BSM physics or small contributions arising in the SM due to loop effects and are not accessible with the current experimental precision. The parity-violating interaction of a pseudoscalar (CP-odd state) corresponds to the a_3 terms, while the other terms describe the parity-conserving interaction of a scalar (CP-even state). Due to the fact that kinematics of the H boson production in WW fusion and in ZZ fusion are very similar it is assumed that $a_i^{WW} = a_i^{ZZ} = a_i$ and $k_1^{WW}/(\Lambda_1^{WW})^2 = k_1^{ZZ}/(\Lambda_1^{ZZ})^2 = a_{\Lambda_1}$.

Among the anomalous contributions, considerations of symmetry and gauge invariance require $k_1^{ZZ} = k_2^{ZZ} = -exp(i\phi_{\Lambda_1}^{ZZ})$, $k_1^{\gamma\gamma} = k_2^{\gamma\gamma} = 0$, $k_1^{gg} = k_2^{gg} = 0$, $k_1^{Z\gamma} = 0$ and $k_2^{i\phi_{\Lambda 1}^{Z\gamma}}$, where $\phi_{\Lambda 1}^{Z\gamma}$ is the phase of the corresponding coupling.

It should be noted that other approaches to analysis are possible and have been undertaken. For example, one can choose the SMEFT (Standard Model Effective Field Theory) formulation, in which the SU(2)×U(1) symmetry is assumed. However, in this paper, we will focus on the first approach.

The purpose of the analysis is to constrain the three sets of couplings (a_2, a_3 and a_{Λ_1}). The results are expressed in terms of cross sections, or equivalently, signal strengths $\mu_j = \sigma_j/\sigma_{SM}$, and the fractional contributions f_i of the couplings a_i to cross sections The effective cross section f_{ai} and phase ϕ_{ai} are defined as follows:

$$f_{ai} = \frac{|a_i|^2 \sigma_i}{\sum_{j=1,2,3,\Lambda_1} |a_j|^2 \sigma_j}, \quad \phi_{a_i} = \arg\left(\frac{a_i}{a_1}\right) \tag{2}$$

Where the fraction $f_{a1} = 1 - f_{\Lambda_1} - f_{a2} - f_{a3}$ is the SM tree-level contribution.
$f_{ai} = 0$ indicates a pure SM Higgs boson, $f_{ai} = 1$ gives a pure BSM particle and $f_{ai} = 0.5$ means that the two couplings contribute equally to the process.

This formulation with f_{ai} allows the presentation of experimental results in the most direct way, with a minimal and complete set of parameters describing the given processes. This approach has several convenient features. The cross sections and their ratios are invariant with respect to the coupling convention. The cross section fractions f_{ai} reflect kinematic features in either production or decay in a direct way. They are conveniently bounded between -1 and +1, and the systematics that affect the normalization of the signal processes cancel out in the ratio.

Anomalous effects in the H boson couplings to fermions can be parameterized with the amplitude :

$$A(Hff) = -\frac{m_f}{v} \bar{\phi}_t (k_f + i\tilde{k_f}\gamma_5)\phi_t \tag{3}$$

where ϕ_f and $\bar{\phi}_f$ are the Dirac spinors, m_f is the fermion mass, v is the SM H field vacuum expectation value, and k_f and $\tilde{k_f}$ are the CP-even and CP-odd Yukawa couplings. In the SM $k_f = 1$ and $\tilde{k_f} = 0$. As for the HVV coupling is more convinient to measure the CP structure with

$$f_{CP}^{Hff} = \frac{|\tilde{k_t}|^2}{|k_t|^2 + |\tilde{k_t}|^2} sign(\tilde{k_t}/k_t) \tag{4}$$

in the SM $f_{CP} = 0$

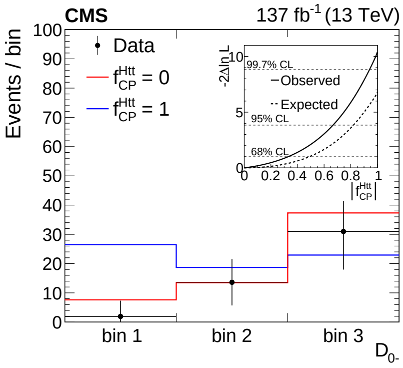

Figure 1: The distribution of events weighted by S/(S + B) (S = Signal, B = Background) in three bins of the D_{0^-} discriminant. In this display, leptonic/hadronic channels and BDT-bkg categories are combined in the mass range $115 < m_{\gamma\gamma} < 135$ GeV and the background contribution, as determined in the fit to data, is subtracted. The inner panel shows the likelihood scan for $|f_{CP}^{Htt}|$ 4).

3 CP structure of the Yukawa interactions with ttH production and diphoton decay

The tree-level top quark Yukawa (Htt) coupling and its CP structure can be tested by studying H production in association with a top quark-antiquark pair (ttH). One of the most sensitive channels for probing the ttH process is $H \to \gamma\gamma$.

In the ttH analysis in which the Higgs boson decay in to two photons, H candidates are built from pairs of photon, which are reconstructed from energy clusters in the electormagnetic calorimiter (ECAL) not linked to charged-particle tracks (with the exception of converted photons). The photon energies are corrected for the containment of electromagnetic showers in the clustered crystals and the energy losses of converted photons with a multivariate regression technique based on simulation. Photons are further required to satisfy a loose identification criterion based on a boosted decision tree (BDT). After the preselection described above,it is required that $100 < m_{\gamma\gamma} < 180$ GeV, $p_T/m_{\gamma\gamma} > 1/3$ and 1/4 for the leading (in p_T) and subleading photons respectively and then divide events into two channels. The leptonic channel is aimed at selecting events where at least one top quark decays leptonically. The hadronic channel targets $t\bar{t}$ hadronic decays by requiring at least three jets, at least one b-tagged jet, and no isolated leptons (electron or muon). A dedicated BDT discriminant ("BDT-bkg") is employed in each channel to distinguish between ttH and background events. A BDT is trained to distinguish CP-even and CP-odd contributions. The output of the BDT is the D_0^- observable. Simulation shows that D_0^- has negligible correlation with the BDT-bkg discriminant. The events selected for the cross section measurements are split into 12 categories, leptonic or hadronic, two BDT-bkg categories and three D_0^- bins. Fig. 1 shows the distribution of events in three bins of the D_{0^-}. The data disfavor the pure CP-odd model of the Htt coupling at 3.2 σ, and a possible fractional CP-odd contribution is measured to be $f_{CP}^{Htt} = 0.00 \pm 0.33$.

4 Anomalous couplings using the four-leptons final state

In the analysis H $\to$ ZZ $\to$ 4l, three mutually exclusive channels: H $\to$ 4e, 4μ, and 2e2μ are considered. This analysis is of particular importance as it is sensitive to various types of couplings. The ttH and gluon-fusion production modes (under the assumption that the gluon gluon fusion loop is dominated by top quarks) can be utilized to investigate the anomalous coupling between the Higgs boson and fermions. Additionally, the HVV coupling can be studied both in production (e.g., Higgs production through Vector Boson Fusion) and in decay, thus providing access to different phase spaces.

At least two leptons are required to have $p_T > 10$ GeV, and at least one is required to have $p_T > 20$ GeV. All four pairs of oppositely charged leptons that can be built with the four leptons are required to satisfy $m_{l^+l^-} > 4$ GeV regardless of lepton flavor. The Z candidates are required to satisfy the condition $12 < m_{l^+l^-} < 120$ GeV, where the invariant mass of at least one of the Z candidates must be larger than 40 GeV. The region between 105 and 140 GeV in the four-lepton invariant mass (m_{4l}) is considered in this analysis. Kinematic distributions of particles produced in the H boson decay or in the associated production with other particles are sensitive to the quantum numbers and anomalous couplings of the Higgs boson. The full kinematic information from each event using either the Higgs boson decay or associated particles in its production is extracted using discriminants from matrix element calculations. The discriminants used in this study are computed using the MELA 6) package which is designed to reduce the number of observables to a minimum, while retaining all essential information. Two categorization schemes are employed in this analysis, one designed to study Htt and Hgg and the other designed to study HVV anomalous couplings. To increase the sensitivity of the analysis the events are categorized to better distinguish between different production modes and different couplings.

In the analysis of HVV couplings, two different fitting methods were applied: the first method (”fix others”) allows only one anomalous coupling to vary while fixing the others at zero, whereas in the second method (”float others”), all anomalous couplings are allowed to vary during the fit. The results for the different couplings are shown in Table 1. As expected, the first method achieves better sensitivity for the parameters but makes the result more model-dependent than the first. The combination of the $H \rightarrow 4l$ and $\gamma\gamma$ channels with ttH, tH, and ggH processes is performed and the result related to f_{a3} and f_{CP}^{Htt} are shown in Fig. 2

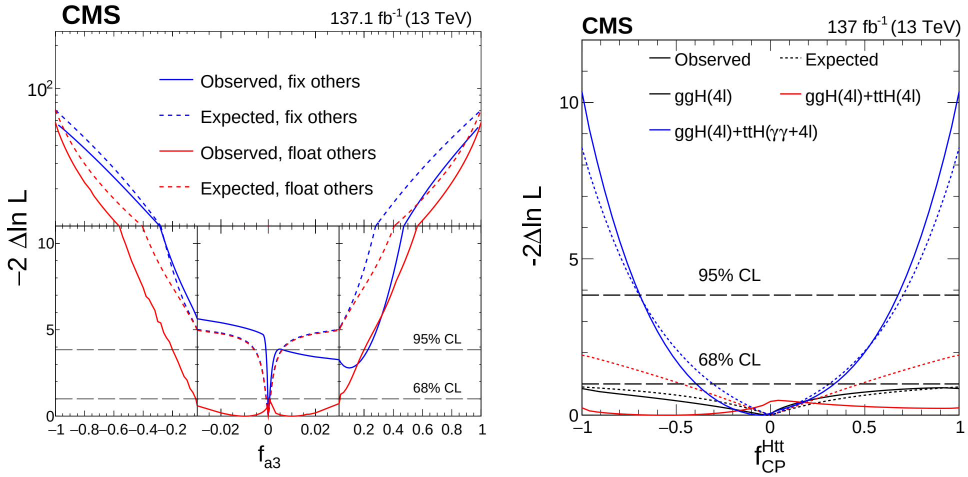

Figure 2: *On the left, observed (solid) and expected (dashed) likelihood scans of f_{a3}. The results are shown for each coupling fraction fit separately with the other three either set to zero or left unconstrained in the fit. In all cases, the signal strength parameters have been left unconstrained. The dashed horizontal lines show the 68 and 95% CL regions. On the right, constraints on the anomalous H boson couplings to top quarks in the ttH, tH, and ggH processes combined, assuming top quark dominance in the gluon fusion loop, using the $H \rightarrow 4l$ and gg decays. Observed (solid) and expected (dashed) likelihood scans of f_{Htt} CP are shown in the ggH process with $H \rightarrow 4l$ (black), ttH, tH, and ggH processes combined with $H \rightarrow 4l$ (red), and in the ttH, tH, and ggH processes with $H \rightarrow 4l$ and the ttH and tH processes with gg combined (blue). Combination is done by relating the signal strengths in the three processes through the couplings in the loops in both production and decay 5).*

5 Constraints on anomalous Higgs boson couplings using the $H \rightarrow \tau\tau$ final state

The study uses Higgs boson candidates produced mainly in electroweak vector boson or gluon fusion that subsequently decay to a pair of τ leptons. Selected events are classified according to four decay channels, $e\mu$, $e\tau_h$, $\mu\tau_h$, and $\tau_h\tau_h$. The resulting event samples are made mutually exclusive by discarding events that have additional loosely identified and isolated electrons or muons. The largest irreducible source of background is Drell-Yan production of $Z \rightarrow \tau\tau$, while the dominant background sources with jets misidentified as leptons are QCD multijet and W+jets.

Event categories are designed to increase the sensitivity to the signal by isolating regions with large signal-to-background ratios, and to provide sensitivity to the Hgg and HVV parameters. Using the same methodology as the previous analysis, the MELA package is once again employed to categorize the data in this case.

Table 1: *Allowed 68% CL (central values with uncertainties) intervals on anomalous HVV coupling parameters using the $H \to 4l$ decay channel* [5].

parameter	method	Observed	[68% CL]
f_{a3}	fix others $f_{a2} = f_{\Lambda_1} = f^{Z\gamma}_{\Lambda_1} = 0$	0.00004	[-0.00007,0.00044]
f_{a3}	floating others	-0.00805	(-0.00010,0.00061]
f_{a2}	fix others $f_{a3} = f_{\Lambda_1} = f^{Z\gamma}_{\Lambda_1} = 0$	0.00020	[-0.00010, 0.00109]
f_{a2}	floating others	-0.24679	[-0.41087, -0.15149] U[-0.00008, 0.00065]
f_{Λ_1}	fix others $f_{a3} = f_{a_2} = f^{Z\gamma}_{\Lambda_1} = 0$	0.00004	[-0.00002, 0.00022]
f_{Λ_1}	floating others	0.18629	[-0.00002, 0.00019]
$f^{Z\gamma}_{\Lambda_1}$	fix others $f_{a3} = f_{a_2} = f_{\Lambda_1} = 0$	-0.00001	[-0.00099,0.00057]
$f^{Z\gamma}_{\Lambda_1}$	floating others	-0.02884	[-0.09000, - 0.00534]U[-0.00068, 0.00078]

The results are combined with those from the $H \to 4l$ and $H \to \gamma\gamma$ decay channels to yield the most stringent constraints on anomalous Higgs boson couplings to date as shown in Fig. 3 and table 2

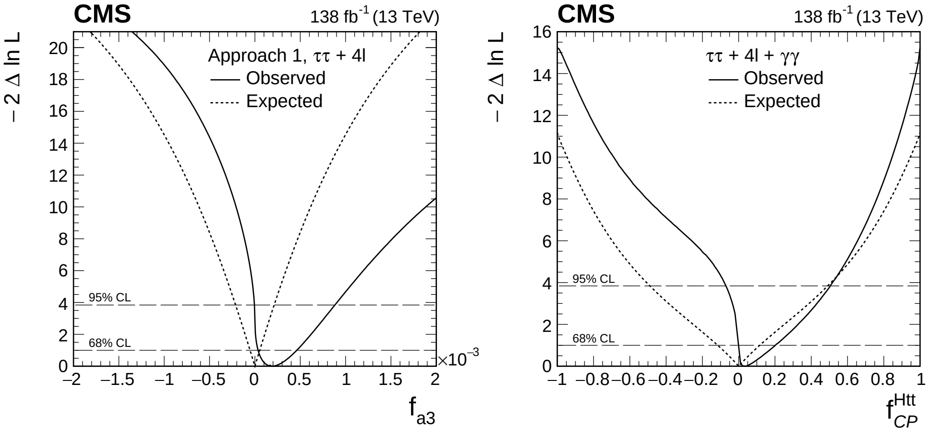

Figure 3: *On the left: observed (solid) and expected (dashed) likelihood scans of f_{a_3} (left) and f^{Htt}_{CP} (right) obtained with the combination of results using the $H \to \tau\tau$ and $H \to 4l$ decay channels* [7].

Table 2: *Allowed 68% CL (central values with uncertainties) intervals on anomalous coupling parameters using the $H \to \tau\tau$ $H \to 4l$ decay channel* [7].

parameter	Observed/10^{-3} [68% CL]	Expected/10^{-3} [68% CL]
f_{a3}	$0.20^{+0.26}_{-0.16}$	$0.00^{+0.05}_{-0.05}$
f_{a2}	$0.7^{+0.8}_{-0.6}$	$0.00^{+0.5}_{-0.4}$
f_{Λ_1}	$-0.04^{+0.04}_{-0.08}$	$0.00^{+0.11}_{-0.04}$
$f^{Z\gamma}_{\Lambda_1}$	$-0.7^{+1.6}_{-1.3}$	$0.00^{+1.0}_{-1.0}$
f^{Htt}_{CP}	$0.28^{+0.39}_{-0.23}$	$0.00^{+0.08}_{-0.08}$

6 Conclusion

The study of the spin and parity properties of the Higgs boson is a crucial area for exploring physics beyond the Standard Model. Investigating potential signs of CP violation in Higgs couplings has been a primary research focus. This field is rapidly expanding, with recent advancements offering new interpretative possibilities. Moreover those analyses are limited by statistical uncertainties, so we expect improvements from the increase in data.

References

1. ATLAS Collaboration Phys. Lett. B 716 1–30 (2012), 10.1016/j.physletb.2012.08.020
2. The CMS collaboration Phys. Lett. B 716 30–61 (2012) 10.1016/j.physletb.2012.08.021
3. The CMS collaboration JHEP 06 081 (2013), 10.1007/JHEP06(2013)081
4. The CMS collaboration Phys. Rev. Lett. 125 061801 (2020), 10.1103/PhysRevLett.125.061801
5. The CMS collaboration Phys. Rev. D 104 0520042021
6. Gritsan A. V., Röntsch R., Schulze M. Xiao M. Phys. Rev. D 94 055023 (2016)
7. The CMS collaboration Phys. Rev. D 108 032013 (2023)

Frascati Physics Series Vol. 76 (2024)
8th young researchers' workshop 'Physics Challenges in the LHC Era'
May 13 and 16, 2024

STUDY OF THE GAS TARGET DENSITY PROFILE FOR THE REACTION ^{22}Ne$(\alpha, n)^{25}$Mg

Marianna Vagnoni
on behalf of the LUNA Collaboration
Università di Roma "La Sapienza", Rome, Italy.

Abstract

The ^{22}Ne$(\alpha, \mathrm{n})^{25}$Mg nuclear reaction is an important neutron source, via s-process, and its rate also plays a role in type one-A supernovae. The LUNA Collaboration, using the Bellotti Ion Beam Facility, installed at the National Gran Sasso Laboratory (LNGS), is studying this reaction in the framework of ERC-Sarting Grant SHADES. The main goals are the measurement of the ^{22}Ne$(\alpha, \mathrm{n})^{25}$Mg cross section in the low-energy range $600 - 800$ keV and the redetermination of the 702 keV resonance energy and strength. This measurement is realized by bombarding a ^{22}Ne gas with an high intense α beam. The windowless gas target is realized by three differential pumping stages and it must be characterized in terms of beam heating. In this contribution we will present the measurements of the density profile of the gas target through the ^{20}Ne$(\mathrm{p}, \gamma)^{21}$Na reaction.

1 Introduction

Nuclear astrophysics arose when scientists understood the crucial role of nuclear physics to explain the nucleosynthesis of elements inside stars via thermonuclear reactions. The goal of nuclear astrophysics is to directly measure the nuclear cross section in the energy range of astrophysical interest as required by theoretical models.

The ^{22}Ne$(\alpha, \mathrm{n})^{25}$Mg reaction is one of the main neutron source for s-processes in stars together with the ^{13}C$(\alpha, \mathrm{n})^{16}$O reaction. In particular, the ^{22}Ne$(\alpha, \mathrm{n})^{25}$Mg reaction produces neutrons for main s-process in Asymptotic Giant Branch (AGB) stars, where it provides a high flux of neutrons for a short time interval, affecting mainly branchings in the s-process path. Moreover, this reaction is the main neutron source for weak s-process in massive stars ($\mathrm{M} \geq 8\ \mathrm{M}_{\odot}$), producing most of the s elements between iron (Fe) and strontium (Sr).

The ^{22}Ne$(\alpha, \mathrm{n})^{25}$Mg reaction rate has significant uncertainties at the temperatures of interest in AGB stars and massive stars (T $\simeq 0.3$ GK). The effects of these uncertainties on nucleosynthesis have been studied by Pignarari et al. $^{1)}$ and The et al. $^{2)}$. Both studies find that the current uncertainties on the cross section of this reaction produce uncertainties of up to a factor of 10 in the abundances of key elements on the s-process path.

Different experimental campaigns were performed by Stuttgart group, i.e. Harms et al. $^{3)}$, Drotleff et al. $^{4)}$ and Jeager et al. $^{5)}$, at Dynamitron accelerator using an extended gas target, but they obtained only upper limit data in the energy range of astrophysical interest due to a high level of neutrons from cosmic rays.

The SHADES (Scintillator-He3 Array for Deep-underground Experiments on the S-process) ERC-project[1], in the framework of the LUNA Collaboration, aims to directly measure the $^{22}\mathrm{Ne}(\alpha,\mathrm{n})^{25}\mathrm{Mg}$ cross section in the low energy range ($600-800$ keV), reaching a precision of $\sim 10\%$. To achieve this goal, SHADES makes the measurement at the underground Gran Sasso National Laboratory (LNGS), which provides a natural shielding from cosmic rays and a neutrons flux reduction of 4 orders of magnitude.

SHADES setup consists of a high-efficiency array composed of liquid scintillators and ^{3}He counters, combined with an extended windowless gas target (220 mm effective length) with a recirculation system for the enriched ^{22}Ne gas. The setup is installed at the second beam line of the Bellotti Ion Beam (BIB) facility, a new accelerator at LNGS.

A dedicated gas target characterization is of crucial importance to obtain a cross section measurement with a precision below 10% and it can be realized using the Narrow Resonance Technique to investigate the beam heating effect.

2 Experimental setup and procedure

The thermodynamic conditions of the gas changes inside the target chamber when an intense ion beam impinges into target particles. In particular, a local heating from ion energy loss is produced during interactions with target particles: the beam heating effect. To analyzed the beam heating effect, a gas target characterization is performed using the Narrow Resonance Technique, which consists of studying a well-defined narrow resonance along the beam path in terms of energy and position where the resonance is populated $^{?)}$. The SHADES gas target is characterized with the resonance of $^{20}\mathrm{Ne}(\mathrm{p},\gamma)^{21}\mathrm{Na}$ reaction at $\mathrm{E_R} = 1168$ keV [2]. The Q-value of this reaction is Q = 2431.6 keV and the ^{21}Na level at $\mathrm{E_X} = 3455.3$ keV is excited with the beam energy on resonance. This level de-excites to the ground state with a branching ratio BR = 99%. The $^{20}\mathrm{Ne}(\mathrm{p},\gamma)^{21}\mathrm{Na}$ reaction produces a γ-spectrum at each position of the target chamber, so each spectrum is acquired using a 2" × 2" $\mathrm{LaBr_3}$ detector. The detector is positioned on a movable table on one side of the chamber and surrounded by a 5 cm thick lead shielding with a 3 cm aperture in front of the detector itself. The experimental setup for the SHADES gas target characterization is shown in figure 1. The $\mathrm{LaBr_3}$ detector can be moved along the beam path through 14 steps and, at each position, a γ-spectrum is acquired and a complete resonance scan is obtained. Resonance scans have been performed at fixed beam energy $\mathrm{E_{beam}}$ at different target pressures p and, for each pressure, with different values of beam intensity $\mathrm{I_{beam}}$. For each complete resonance scan, a data structure is created to store all the experimental conditions of each run. It is created implementing a *Python* routine, using the *pandas* library $^{9)}$. Part of a selected data structure is shown in table 1.

---

[1] ERC-StG SHADES, no. 852016

[2] The energy is expressed in the laboratory frame, otherwise it is explicated.

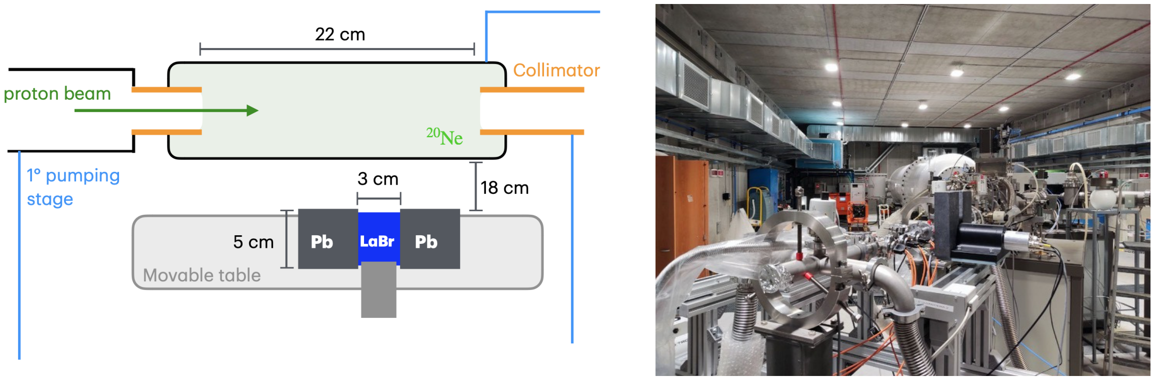

Figure 1: *On the left the scheme of the experimental setup for the SHADES gas target. A* $LaBr_3$ *scintillator on a movable table on one side of the target chamber surrounded by lead shielding. On the right a photo of the experimental setup at the Bellotti Ion Beam Facility.*

Table 1: *Part of a selected data structure related to a complete resonance scan created with the pandas library to store data.*

E_{beam} [keV]	I_{beam} [μA]	p [mbar]	x [mm]
1176	46.2	4.0	272.8
1176	46.2	4.3	253.2
1176	46.2	4.3	232.7
1176	46.2	4.4	213.3
1176	46.2	4.5	193.3
1176	46.2	4.5	173.8
1176	46.2	4.5	133.9
1176	46.2	4.5	113.9
1176	46.2	4.5	93.7
1176	46.2	4.5	73.8
1176	46.2	4.5	53.3
1176	46.2	4.6	34.2
1176	46.2	4.6	14.0
1176	46.2	4.6	-14.0

3 Data analysis and results

The gas target density can be extracted from the yield as a function of the position. The yield is defined as the number of signal events normalized by the total charge. Therefore, to extract the number of signal events under the resonance peak of interest at $E_\gamma = 3544.3$ keV, a detailed study of the background is necessary.

The background events are created by natural background, intrinsic background and beam-induced background. Firstly, the natural and intrinsic background is studied by analyzing a background spectrum acquired with the $LaBr_3$ detector (fig. 2).

The natural background is produced by environmental isotopes like ^{40}K and ^{208}Tl, while the intrinsic background is produced by the intrinsic isotopes of the $LaBr_3$ scintillator, such as ^{138}La and ^{227}Ac. In particular, the ^{138}La decays into two parallel processes: a β^- decay into ^{138}Ce and an electronic capture

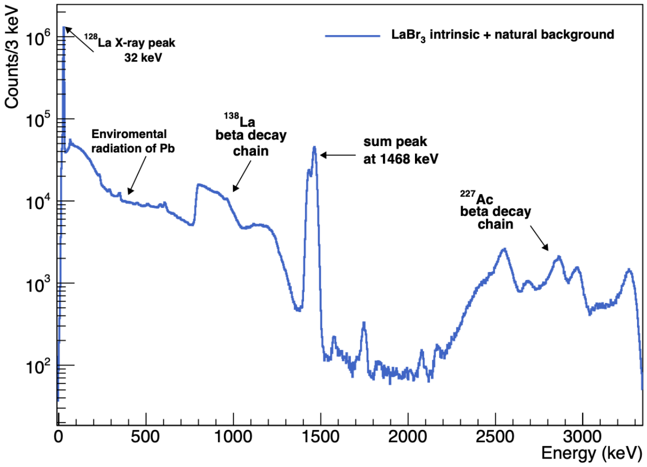

Figure 2: *Background spectrum acquired without beam. This spectrum is compatible with the LaBr$_3$ intrinsic background spectrum produced by the radioactive isotope ^{138}La and by the radioactive contaminant ^{227}Ac.*

that disintegrates the isotope. The ^{227}Ac contaminant is part of the ^{235}U decay chain, that is composed of different nuclear processes such as α, β and γ-rays emissions. The level of natural and intrinsic background is lower than the signal level, so it is negligible.

Secondly, the number of beam-induced background events must be extracted in the region of interest around $E_\gamma = 3544.3$ keV, analyzing the signal spectrum. In the $^{20}\mathrm{Ne}(\mathrm{p},\gamma)^{21}\mathrm{Na}$ spectrum there are no peaks associated with possible beam-induced background processes, so the level of beam-induced background is of the same order of the level of natural and intrinsic background. Therefore, all the materials used in the gas target system can be considered of high purity. Moreover, a model to parametrize the beam-induced background does not exist, so a dedicated analysis of the possible background under the peak of interest at $E_\gamma = 3544.3$ keV is necessary.

For each position along the gas target, two different models for the γ-spectrum "on-resonance" and "out-resonance" are used. They are chosen by the best-fit model on the background in the lateral side around the peak of interest.

For the "on-resonance" spectrum, an exponential function is used (fig. 3):

$$f_r = N\ e^{-ax} + k \tag{1}$$

While, for the "out-resonance" spectrum, a polynomial function is used (fig. 3):

$$f_{nr} = p_4 x^4 + p_3 x^3 + p_2 x^2 + p_1 x + p_0 \tag{2}$$

The number of background events (B) are extracted integrating the best-fit background function in the region of interest and the number of signal events (S) are calculated subtracting the number of background events, B, to the total number of events (N). The number of total events, N, is obtained integrating the histogram in the region of interest.

The yield at each position along the gas target is calculated using the number of signal events, S, and the total charge, Q_{tot}:

$$Y = \frac{S}{Q_{tot}} \tag{3}$$

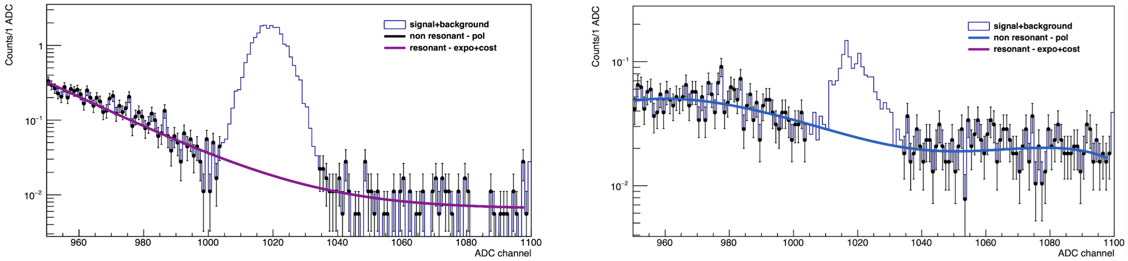

Figure 3: *On the left, the spectrum "on-resonance". On the right, the spectrum "out-resonance". The best-fit is executed only on the lateral sides of the peak, where data are underlined in black.*

and so the yield as a function of position is obtained.
The positions scale can be converted into energy via equation 4, using:

$$E(x) = E_{beam} - \frac{x}{d}\Delta E \tag{4}$$

where E(x) is the energy in position x, E_{beam} is the beam energy, x is the position which can be converted, d is the total target length and ΔE is the total beam energy loss calculated using the stopping power. The stopping power is calculated using a software for simulations of matter interactions called SRIM (Stopping and Range of Ions in Matter) $^{8)}$. In figure 4, the yield profile as a function of the position is shown on the left and the yield profile as a function of energy is shown on the right. These yield profiles are related to a complete resonance scan with $E_{beam} = 1176$ keV, $I_{beam} = 46.2\ \mu$A and p = 4.3 mbar. The magenta points are related to repeated runs that are compatible with the previous runs. On each yield profile, the green star represents the entrance of the gas target chamber and the red stars represents its exit. The yield profile as a function of positions is analyzed using the theoretical yield defined as:

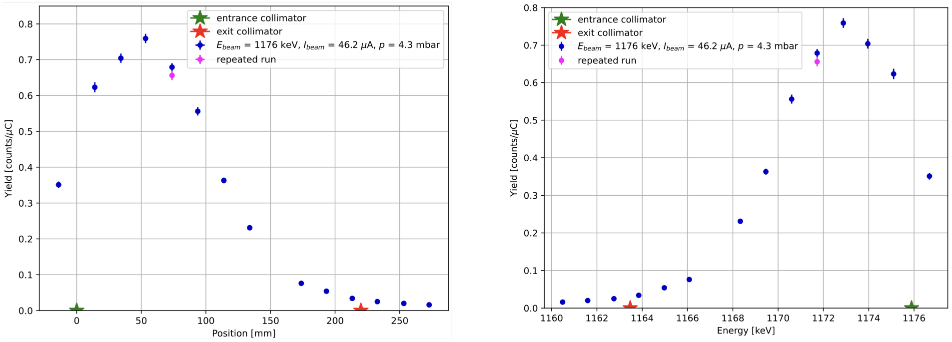

Figure 4: *Yield profiles for a complete resonance scan with $E_{beam} = 1176\ keV$, $I_{beam} = 46.2\ \mu A$ and $p = 4.3\ mbar$. The green star represents the entrance of the gas target chamber and the red stars represents the exit of the gas target chamber. On the left, yield vs position. On the right, yield vs energy.*

$$Y(E_0) = \int_0^{x_{max}} dx \int_{E_0}^{0} f(E, E(x))\, \sigma_{BW}\ \eta(x)\ \rho(x)\ dE \tag{5}$$

where E_0 is the beam energy, x_{max} is the target chamber length, ρ(x) is the gas density, η(x) is the detector efficiency, σ_{BW} is the cross section of a narrow resonance and f(E, E(x)) is the straggling distribution function 7), defined as:

$$f(E,E(x)) = exp\left(\frac{(E-E(x))^2}{2\sigma^2_{beam} + 2\sigma^2_{straggle}(E(x))}\right) \tag{6}$$

where $\sigma_{\mathrm{beam}} \simeq 0.1\ keV$ and $\sigma_{\mathrm{straggle}}$ is defined according to the Bohr approximation:

$$\sigma_{straggle} = 1.20 \times 10^{-12}\sqrt{Z_p^2 Z_t \frac{\Delta E}{\varepsilon}} \tag{7}$$

where $\mathrm{Z_p}$ is the projectile particle charge, $\mathrm{Z_t}$ is the target particle charge, ΔE is the total energy loss and ε is the stopping power simulated by SRIM 8).

In figure 5, three different yield profiles with different beam energies, but similar beam currents and pressures inside the target chamber are shown. The comparison between these yield profiles shows that the narrow resonance at $\mathrm{E_R} = 1168$ keV of the $^{20}\mathrm{Ne}(\mathrm{p},\gamma)^{21}\mathrm{Na}$ reaction is populated at different positions along the beam path while beam energy varies.

The theoretical yield is calculated through a *Python* routine and is compared to the experimental yield. The gas target density is extracted from the position where the resonance is populated for each of complete resonance scan. The full data analysis is in progress.

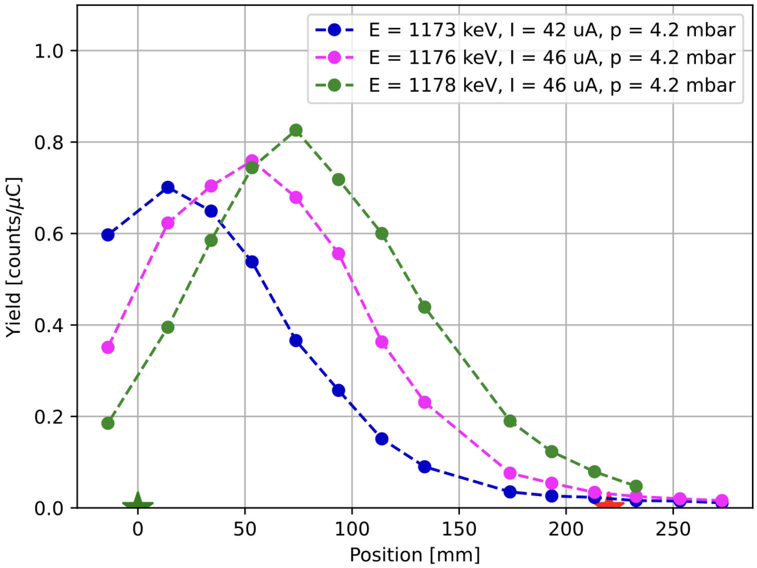

Figure 5: *Yield profile with different beam energies, but similar beam currents and gas pressures. The green star represents the entrance of the gas target chamber and the red stars represents the exit of the gas target chamber.*

4 Conclusion

The SHADES gas target characterization is an important step toward the $^{22}\mathrm{Ne}(\alpha,\mathrm{n})^{25}\mathrm{Mg}$ cross section measurement with a precision below 10%.

The gas inside the target chamber changes according to the beam heating effect that can be studied using the Narrow Resonance Technique. To perform this technique for the SHADES gas target characterization, the resonance at $E_R = 1168$ keV of the $^{20}\mathrm{Ne}(\mathrm{p},\gamma)^{21}\mathrm{Na}$ reaction is used and the gas density is extracted, analyzing the yield as a function of position.

In this preliminary analysis, the gas target densities extracted at different positions inside the gas target for similar experimental conditions (E_{beam}, I_{beam} and p) are consists within the 7%. Moreover, the beam-induced background is of the same order of the natural and intrinsic background, so all the materials used to build the gas target system are radiopure. Therefore, the SHADES gas target has optimal characteristics to achieve a precision below the 10% in the cross section measurement of $^{22}\mathrm{Ne}(\alpha,\mathrm{n})^{25}\mathrm{Mg}$ reaction.

References

1. M. Pignatari *et al*, Nucl. Phys. A **758**, 541-544 (2005).
2. L. The *et al.*, Ap. J. **533**, 998-1015 (2000).
3. V. Harms *et al*, Phys. Rev. C **43(6)**, 2849-2861 (1991).
4. H.W. Drotleff *et al*, ApJ **414(2)**, 735-739 (1993).
5. M. Jaeger *et al*, PRL **87(20)**, 202501 (2001).
6. J. Gorres *et al*, Nucl. Instrum. Methods Phys. Res. **177**, 295-303 (1980).
7. D. Bemmerer *et al*, EPL **122**, 52001 (2018).
8. J. F. Ziegler *et al*, Nucl. Instrum. Methods Phys. Res. B **268** 1818- 1823 (2010).
9. W. McKinney *et al*, https://pandas.pydata.org (2024)

Frascati Physics Series Vol. 76 (2024)
8TH YOUNG RESEARCHERS' WORKSHOP 'PHYSICS CHALLENGES IN THE LHC ERA'
May 13 and 16, 2024

A Simple Model for Pentaquarks

Davide Germani
Sapienza University of Rome and INFN, Piazzale Aldo Moro 2, I-00185, Italy

Abstract

We describe pentaquarks as 'baryo-charmonia' with a color octet $c\bar{c}$ core bonded to a color octet three-quark system. Fermi statistics of the light quark cloud allows to describe two pentaquark triplets: a lower one, well supported by experiment, and a higher one with strangeness. For the time being, the lowest line of the strange triplet has been experimentally identified in a 3σ peak. Data also suggest two different production mechanisms for pentaquarks. We show how this can be described in the proposed scheme.

1 Introduction

Let the pentaquarks be formed by three light quarks in color octet $(qqq)_{\mathbf{8}}$ orbiting in the mean color field of a charm-anticharm heavy pair $(c\bar{c})_{\mathbf{8}}$, a sort of 'baryo-charmonium'. The Fermi statistics of the light quarks leads to a determination of the spectrum of the best ascertained $J/\psi p$ pentaquarks, $P_c(4312)$, $P_c(4440)$ and $P_c(4457)$ 1), as well as to the prediction of two extra lines in the strange sector, in addition to the observed one. The lighter state in the strange pentaquark system is a 3σ peak, dubbed $P_{cs}(4459)$ by LHCb 4). The two heavier ones we predict, P'_{cs}, P''_{cs}, see Fig. 2, have roughly a similar level of significance and are found in a region where present data show fluctuations over the background. For both triplets we predict the same ordering of spins, namely $J = 1/2, 3/2, 1/2$, for increasing masses. The three P_c pentaquarks are observed in $\Lambda_b^0 \to (J/\psi p)K^-$ decays and the $P_{cs}(4459)$ peak is found in $\Xi_b^- \to (J/\psi\Lambda)K^-$. Data suggest at least two different production mechanisms for pentaquarks, idependently on their strangeness content.

In addition to the associated production with K in heavy baryon decays, the $\tilde{P}_c(4337)$ has been reported by 2) in the decay $B_s^0 \to (J/\psi p)\bar{p}$. A strange partner of $\tilde{P}_c$, the $\tilde{P}_{cs}(4338)$, is found in 3) in associated production with the anti-proton ($B^- \to (J/\psi\Lambda)\bar{p}$). We use the tilde to distinguish the pentaquarks produced in association with the anti-proton from those produced in association with the K. We will

Table 1: *Pentaquarks discovered by the LHCb collaboration* [1, 2, 3, 4]. *The first 4 states have light quarks content uud, the last two have uds. For $P^0_{cs}(4338)$, the experimentally preferred J^P is indicated next to the name.*

State	Mass [MeV]	Width [MeV]	Observed Process	Year
$P_c(4312)$	$4311.9 \pm 0.7^{+6.8}_{-0.6}$	$9.8 \pm 2.7^{+3.7}_{-4.5}$	$\Lambda^0_b \to (J/\psi\, p)\, K^-$	2019
$\tilde{P}_c(4337)$	$4337^{+7}_{-4}{}^{+2}_{-2}$	$29^{+26}_{-12}{}^{+14}_{-14}$	$B^0_s \to (J/\psi p)\, \overline{p}$	2022
$P_c(4440)$	$4440.3 \pm 1.3^{+4.1}_{-4.7}$	$20.6 \pm 4.9^{+8.7}_{-10.1}$	$\Lambda^0_b \to (J/\psi\, p)\, K^-$	2019
$P_c(4457)$	$4457.3 \pm 0.6^{+4.1}_{-1.7}$	$6.4 \pm 2.0^{+5.7}_{-1.9}$	$\Lambda^0_b \to (J/\psi\, p)\, K^-$	2019
$\tilde{P}_{cs}(4338)\frac{1}{2}^-$	$4338.2 \pm 0.7 \pm 0.4$	$7.0 \pm 1.2 \pm 1.3$	$B^- \to (J/\psi\, \Lambda)\, \overline{p}$	2022
$P_{cs}(4459)$	$4458.9 \pm 2.9^{+4.7}_{-1.1}$	$17.3 \pm 6.5^{8.0}_{-5.7}$	$\Xi^-_b \to (J/\psi\, \Lambda)\, K^-$	2021

show how we can describe this pattern comprising P and $\tilde{P}$ pentaquarks and place the observed states $\tilde{P}_c(4337)$, $\tilde{P}_{cs}(4338)$ in multiplets with their expected partners, which we name $\tilde{P}'_c, \tilde{P}''_c$ and $\tilde{P}'_{cs}, \tilde{P}''_{cs}$.

2 Fermi statistics in baryo-charmonia

The light quarks carry color, in the adjoint representation, flavor, spin and orbital quantum numbers and are identical particles obeying Fermi statistics. Let a, b, c be flavor indices and α, β, γ color indices. Requiring both color and flavor to be in the adjoint representation we can form the tensor

$$A^{ijk}_{\alpha\beta\gamma} = \psi^{[a}_{\alpha}\psi^{b]}_{\beta}\psi^{c}_{\gamma} - \psi^{[a}_{\beta}\psi^{b]}_{\gamma}\psi^{c}_{\alpha} = \psi^{a}_{(\alpha}\psi^{b}_{\beta)}\psi^{c}_{\gamma} - \psi^{a}_{(\beta}\psi^{b}_{\gamma)}\psi^{c}_{\alpha}\,, \tag{1}$$

which is anti-symmetric under the exchange of any two quarks provided that

$$\psi^a_\alpha \psi^b_\beta = -\psi^b_\beta \psi^a_\alpha\,. \tag{2}$$

Parentheses in (1) indicate symmetrization (round brackets) or anti-symmetrization (square brackets) of a certain pair of indices. Similarly the tensor S can be formed

$$S^{abc}_{\alpha\beta\gamma} = \eta^{[a}_{\alpha}\eta^{b]}_{\beta}\eta^{c}_{\gamma} - \eta^{[a}_{\beta}\eta^{b]}_{\gamma}\eta^{c}_{\alpha} = \eta^{a}_{[\alpha}\,\eta^{b}_{\beta]}\eta^{c}_{\gamma} - \eta^{a}_{[\beta}\,\eta^{b}_{\gamma]}\eta^{c}_{\alpha}. \tag{3}$$

This is symmetric under the exchange of any two quarks, provided that

$$\eta^a_\alpha \eta^b_\beta = +\eta^b_\beta \eta^a_\alpha\,. \tag{4}$$

The qqq system in the pentaquarks can either be in a color-flavor state A, Eq. (1), or in S, Eq. (3). In the first case the spin-orbital state must be symmetric whereas in the second case it must be anti-symmetric, to enforce Fermi statistics. In pentaquarks light quarks are in a flavor octet and can have both spins 1/2 and 3/2.

Consider pentaquarks produced in the decay of a baryon in association with a K^- meson. In the Λ^0_b baryon, the ud diquark is in the antisymmetric spin zero state, symmetric in color-flavor space. This is called the “good” diquark, as opposite to the spin one bad diquark in the Σ_Q. In the simplest decay process, the initial light quarks propagate to the final state as in Fig. 1. Assuming that the color-flavor symmetry of the ud pair is maintained in the formation of the final state, we choose S in Eq. (3), for the description of the light quarks in the pentaquark. The different production mechanism of the $\tilde{P}$ pentaquarks leads us to distinguish them from the P pentaquarks by using A, as in Eq. (1), in place of S.

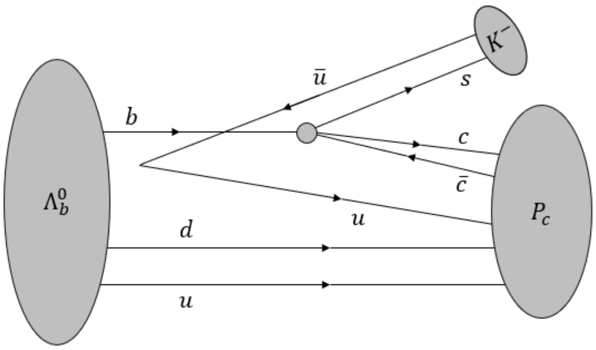

Figure 1: *Possible diagram for the decay* $\Lambda_b^0 \to P_c K^-$*.*

Each quark pair, say quark 1 and quark 2, can either be in a anti-symmetric $S = 0$ state or in a symmetric $S = 1$ state. The orbital wave-function of the quark pair (we will call Ψ the spin wave-function, and Φ the orbital one) will be, accordingly, symmetric or anti-symmetric.

3 Exchange interaction

Let U be the color interaction potential between, say, quark 1 and quark 2. The expectation value

$$\langle U \rangle_\Phi = \int \Phi^*(\boldsymbol{r}_1, \boldsymbol{r}_2)\, U(\boldsymbol{r}_1 - \boldsymbol{r}_2)\, \Phi(\boldsymbol{r}_1, \boldsymbol{r}_2)\, d^3\boldsymbol{r}_1\, d^3\boldsymbol{r}_2 \tag{5}$$

can be written as $C \pm J$, with the $\pm$ signs corresponding to Φ being symmetric/anti-symmetric. This in turn can be written as $\langle U \rangle_\Phi = C + \langle V \rangle_\Psi$ provided that $\langle V \rangle_\Psi = \pm J$ depending on Ψ being anti-symmetric ($S = 0$) or symmetric ($S = 1$) respectively. The potential V is given by [5)]

$$V = -\sum_{\text{pairs}} J_{ab} \left(\frac{1}{2} + 2\boldsymbol{S}_a \cdot \boldsymbol{S}_b \right) \tag{6}$$

where

$$J_{ab} = \int (\phi_a(\boldsymbol{r}_a)\phi_b(\boldsymbol{r}_b))^*\, U(\boldsymbol{r}_a - \boldsymbol{r}_b)\, (\phi_a(\boldsymbol{r}_b)\phi_b(\boldsymbol{r}_a))\, d^3\boldsymbol{r}_a\, d^3\boldsymbol{r}_b\,. \tag{7}$$

Using the basis of states $|-++\rangle, |+-+\rangle, |++-\rangle$ one obtains that $\langle V \rangle_\Psi$ splits the two spin 1/2 states, obtained by the combination of three spins 1/2, by

$$\Delta E_{1/2} = \pm\sqrt{J_{12}^2 + J_{13}^2 + J_{23}^2 - J_{12}J_{13} - J_{12}J_{23} - J_{13}J_{23}}\,. \tag{8}$$

The spin 3/2 shift is obtained by $|+++\rangle$ (or $|---\rangle$) to be

$$\Delta E_{3/2} = -J_{12} - J_{13} - J_{23}\,. \tag{9}$$

Orbital wave functions are not known. As for the color potential U, we might use the one-gluon exchange interaction concluding that if the i, j quark pair were in a color-symmetric configuration we would get a positive, repulsive coupling J_S, which, in modulus, is half the negative coupling J_A of the color anti-symmetric configuration [1]

$$J_S = -\frac{1}{2} J_A\,. \tag{10}$$

---

[1] The quadratic Casimir in the repulsive, symmetric, **6** representation is $C(\mathbf{6}) = 10/3$ so that $2(C(\mathbf{6}) - 2C(\mathbf{3})) = -(C(\bar{\mathbf{3}}) - 2C(\mathbf{3})))$.

3.1 P pentaquarks

Let us consider the case $qqq = uud$ in the color-flavor configuration S. Then from (3)

$$S^{121}_{\alpha\beta\gamma} = u_{[\alpha}\, d_{\beta]} u_\gamma + u_{[\gamma}\, d_{\beta]} u_\alpha \tag{11}$$

since the uu cannot be anti-symmetric in flavor space. The pentaquark contains the light quarks u_α, d_β and u_γ with the u quarks, u_α and u_γ, in a color symmetric (repulsive) representation and ud in color attractive, anti-symmetric pairings. Therefore from (10) we require

$$J^{uu}_S = -\frac{1}{2} J^{ud}_A \tag{12}$$

and we can write

$$J_{12} = J^{uu}_S > 0 \qquad J_{13} = J_{23} = J^{ud}_A < 0\,. \tag{13}$$

The pentaquarks discovered in the $J/\psi p$ channel, from Λ_b decays, are found at mass values 1)

$$M_{P_c}(4312) = 4311.9^{+7}_{-0.9}\ \text{MeV}\,, \quad M_{P_c}(4440) = 4440^{+4}_{-5}\ \text{MeV}\,, \quad M_{P_c}(4457) = 4457.3^{+7}_{-1.8}\ \text{MeV}\,. \tag{14}$$

The spins are not known so far. Assume that the ordering in mass corresponds to the lower one being spin 1/2 and the higher two being 3/2 and 1/2 respectively. Then we have to solve the simultaneous equations

$$M_{P_c}(4457) - M_{P_c}(4312) = 2|J^{uu}_S - J^{ud}_A|\,, \tag{15}$$

$$M_{P_c}(4440) - \frac{1}{2}(M_{P_c}(4312) + M_{P_c}(4457)) = -J^{uu}_S - 2J^{ud}_A \tag{16}$$

This system of equations has two sets of solutions, but only one is compatible with the condition of having one positive and two negative couplings. These are found to be

$$J^{uu}_S = 29.9^{+2.5}_{-2.8}\ \text{MeV}\,, \quad J^{ud}_A = -42.8^{+2.4}_{-1.6}\ \text{MeV}\,, \tag{17}$$

which gives

$$\frac{J^{uu}_S}{J^{ud}_A} = -0.7 \pm 0.1\,, \tag{18}$$

not far from the $-1/2$ factor in (10) we aimed to.

To conclude, let's define M_0 as the degenerate mass of the triplet, i.e., the mass that the three particles analyzed in this section would have if we turned off the exchange interactions. The value of M_0 is given by the average mass of the particles with spin 1/2.

$$M_0 = \frac{1}{2}(M_{P_c}(4312) + M_{P_c}(4457)) = 4384^{+4}_{-1}\,\text{MeV}\,. \tag{19}$$

If we consider the spin ordering $1/2, 1/2, 3/2$ for increasing mass values, we would get $S/A \simeq -0.32^{+0.05}_{-0.07}$. This gives a preference to (18) and to the 'inverted' spin ordering $1/2, 3/2, 1/2$ which we will apply also to the strange pentaquarks in the next section. We will take this $S/A \simeq -0.7$ ratio as a benchmark in pentaquarks (also in the case of strange pentaquarks) and assume that $J^{ud} = J^{uu} = J^{dd} \equiv J^{qq}$ in both A or S symmetries.

In addition to the three pentaquark lines described above, a strange $J/\psi\Lambda$ pentaquark has been discovered, with a mass value of 4)

$$M_{P_{cs}}(4459) = 4458.8^{+6}_{-3.1}\ \text{MeV}\,. \tag{20}$$

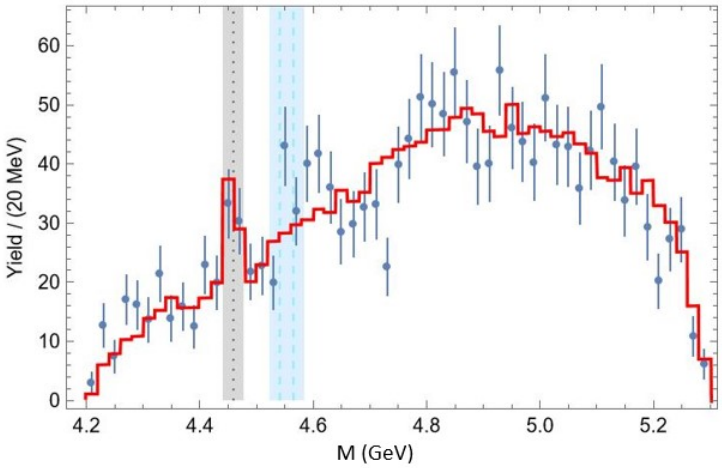

Figure 2: *The dotted line corresponds to the $J/\psi\Lambda$ resonance $P_{cs}(4459)$ reported by LHCb* $^{4)}$. *We take the fitting (red) curve to the P_{cs} peak from LHCb as well. The dashed lines, with uncertainty bands, correspond to our predictions for P'_{cs} and P''_{cs}. The state P''_{cs} is about 20 MeV below the $\bar{D}^*\Xi'_c$ neutral or charged threshold.*

Its mass difference with $M_{P_c}(4312)$ is approximately equal to the baryon mass difference $M(\Lambda) - M(p)$. This suggests to assume that P_{cs} is also a spin 1/2 state, and like the P_c^+, it is the first of a higher strange triplet. In the following we will determine the triplet with strangeness extending the analysis done above. Along the same lines we consider the Λ-like color-flavor symmetric combination

$$S^{123}_{\alpha\beta\gamma} = u_{[\alpha}d_{\beta]}s_\gamma + u_{[\gamma}d_{\beta]}s_\alpha\,. \tag{21}$$

From this we can infer that u and s are in a symmetric, repulsive, pairing J_S^{us} and u, d are in an anti-symmetric pairing J_A^{ud}, which will be taken from (17). As for ds, we can symmetrize and anti-symmetrize color indices so that $J^{ds} = (J_S^{us} + J_A^{us})/2$ where we assume $J_{S,A}^{us} = J_{S,A}^{ds} = J_{S,A}^{qs}$. We will derive J_A^{us} from J_S^{us} using the same $S/A = 1/k$ ratio given in (18) so that

$$J^{ds} = \frac{1+k}{2} J_S^{qs}\,, \tag{22}$$

where $k \simeq -1.43$, i.e. the inverse of the number in (18). We know from data on baryons that the ratio of chromomagnetic couplings in the constituent quark model is $\kappa_A^{qs}/\kappa_A^{qq} \sim 0.6$ $^{6)}$. Applying the same scaling law to J_A's, and consequently to J_S's, we have $J_S^{qs} = 17.9 \pm 2$ MeV which leads to $J^{ds} = -3.9 \pm 2$ MeV. The splitting formulae then give

$$\Delta E_{1/2} = 53.3 \pm 2.3\,\text{MeV}\,, \quad \Delta E_{3/2} = 28.7 \pm 3.5\,\text{MeV}\,. \tag{23}$$

The degenerate mass of this new triplet is

$$M_0^s = M_{P_{cs}} + \Delta E_{1/2} = 4512 \pm 6\,\text{MeV}\,, \tag{24}$$

with $\Delta_s = M_0^s - M_0 = (127 \pm 6)$ MeV to be compared to the analogous $\Delta_s \simeq 177$ MeV known from the baryon octet. The mass spectrum is

$$\begin{aligned} M_{P'_{cs}(3/2)} &= M_0^s + \Delta E_{3/2} = 4541 \pm 6\,\text{MeV}\,, \\ M_{P''_{cs}(1/2)} &= M_0^s + \Delta E_{1/2} = 4565 \pm 6\,\text{MeV}\,. \end{aligned} \tag{25}$$

Therefore the strange pentaquark spectrum is superimposed on available data in Fig. 2. The predicted states end up in a region of $\sim 2\sigma$ fluctuations over the background, so that it is difficult to make any definite conclusion different from an hint to look better at this region.

4 Conclusions

The same procedure we have outlined can be repeated for the pentaquarks we have defined as $\tilde{P}$, using the tensor A for the color-flavor part $^{7)}$. We summarize in Table 2 the values the masses of the observed and predicted Pentaquarks.

Table 2: *In this table we summarize all the masses of the pentaquarks. Pentaquarks in boldface,* $\mathbf{P}$*, are predictions. Experimental values are in parentheses and are taken as input to obtain predictions on the* J *couplings and masses of the pentaquarks* $\mathbf{P}$*. An exception is the* $\widetilde{P}_c(4337)$ *for which we have both the prediction and the experimental value. Each triplet is ordered from top to bottom with* $J = 1/2, 3/2, 1/2$.

	Mass [MeV]		Mass [MeV]
$P_c(4312)$	$(4311.9^{+7}_{-0.9})$	$P_{cs}(4459)$	$(4458.8^{+6}_{-3.1})$
$P_c(4440)$	(4440.0^{+4}_{-5})	$\mathbf{P}'_{cs}$	4541 ± 6
$P_c(4457)$	$(4457.3^{+7}_{-1.8})$	$\mathbf{P}''_{cs}$	4565 ± 6
$\widetilde{\mathbf{P}}''_{\mathbf{c}}$	4187 ± 7	$\widetilde{P}_{cs}(4338)$	(4338.2 ± 0.8)
$\widetilde{\mathbf{P}}'_{\mathbf{c}}$	4276 ± 12	$\widetilde{\mathbf{P}}'_{\mathbf{cs}}$	4387 ± 4
$\widetilde{P}_c(4337)$	$4332 \pm 7\ (4337^{+7}_{-4}{}^{+2}_{-2})$	$\widetilde{\mathbf{P}}''_{\mathbf{cs}}$	4435 ± 4

References

1. The $P_c(4312)^+$ has been reported in R. Aaij *et al.* [LHCb], Phys. Rev. Lett. **115**, 072001 (2015) doi:10.1103/PhysRevLett.115.072001 [arXiv:1507.03414 [hep-ex]], together with $P_c(4450)^+$ which later was realized to consist of two resonances, $P_c(4440)$ and $P_c(4457)$, as discussed in R. Aaij *et al.* [LHCb], Phys. Rev. Lett. **122**, no.22, 222001 (2019) doi:10.1103/PhysRevLett.122.222001 [arXiv:1904.03947 [hep-ex]].

2. R. Aaij *et al.* [LHCb], Phys. Rev. Lett. **128**, no.6, 062001 (2022) doi:10.1103/PhysRevLett.128.062001 [arXiv:2108.04720 [hep-ex]].

3. [LHCb], [arXiv:2210.10346 [hep-ex]].

4. R. Aaij *et al.* [LHCb], Sci. Bull. **66**, 1278-1287 (2021) doi:10.1016/j.scib.2021.02.030 [arXiv:2012.10380 [hep-ex]].

5. N. W. Ashcroft, N. D. Mermin, Holt-Saunders, ISBN 9788131500521, Chapter 32.

6. A. Ali, L. Maiani and A. D. Polosa, Cambridge University Press, 2019, ISBN 978-1-316-76146-5, 978-1-107-17158-9, 978-1-316-77419-9 doi:10.1017/9781316761465

7. D. Germani, F. Niliani and A. D. Polosa, Eur. Phys. J. C **84**, no.7, 755 (2024) doi:10.1140/epjc/s10052-024-13103-y [arXiv:2403.04068v2 [hep-ph]]

Frascati Physics Series Vol. 76 (2024)
8TH YOUNG RESEARCHERS' WORKSHOP 'PHYSICS CHALLENGES IN THE LHC ERA'
May 13 and 16, 2024

SEARCHING FOR EXCLUSIVE LEPTOQUARKS WITH THE NAMBU-JONA-LASINIO COMPOSITE MODEL AT THE LHC AND HL-LHC

S. Ajmal
INFN, Sezione di Perugia, Via A. Pascoli, I-06123, Perugia, Italy
J. T. Gaglione
Department of Physics and Astronomy, Vanderbilt University, Nashville, TN, 37235, USA
A. Gurrola
Department of Physics and Astronomy, Vanderbilt University, Nashville, TN, 37235, USA
O. Panella
INFN, Sezione di Perugia, Via A. Pascoli, I-06123, Perugia, Italy
M. Presilla
Institute for Experimental Particle Physics (ETP), Karlsruhe Institute of Technology (KIT),
Wolfgang-Gaede-Straße 1, 76131 Karlsruhe, Germany
F. Romeo
Department of Physics and Astronomy, Vanderbilt University, Nashville, TN, 37235, USA
H. Sun
Institute of Theoretical Physics, School of Physics, Dalian University of Technology,
No.2 Linggong Road, Dalian, Liaoning, 116024, P.R. China
S. S. Xue
ICRANet, Piazzale della Repubblica, 10-65122, Pescara, Italy
Physics Department, Sapienza University of Rome, Piazzale Aldo Moro 5, 00185 Roma, Italy
INFN, Sezione di Perugia, Via A. Pascoli, I-06123, Perugia, Italy
ICTP-AP, University of Chinese Academy of Sciences, Beijing, China

Abstract

The Composite NJL model, a beyond Standard Model (BSM) theory achieving UV completion via gauge-symmetric four-fermion couplings, distinguishes composite fermions and bosons. This study focuses on composite bosons, particularly their interactions with leptons and quarks, exploring production modes at various jet multiplicities. A strategy is developed to capture all final state particles from leptoquarks and their decays. The assessment of statistical significance for leptoquark couplings in the first and second generations at the LHC shows greater sensitivity than current searches.

1 Introduction

The Standard Model (SM) is a well-established theoretical framework that explains the fundamental particles and interactions governing the observable universe. However, despite its successes, the SM fails to address several key issues, including the hierarchy of fermion masses, the exclusion of gravity, the origin of neutrino masses, and the existence of dark matter and dark energy. The Composite NJL model, a BSM theory, achieves UV completion by integrating gauge-symmetric four-fermion couplings at the high-energy cutoff $\Lambda = \mathcal{O}(\text{TeV})$ [1, 2, 3]. In the gauge symmetric phase, composite particles, consisting of elementary fermions, emerge. In examining the particle spectrum of composite bosons, we focused on the phenomenology of scalar leptoquark (lq) pairs. Leptoquarks (LQs) have appeared in numerous beyond the Standard Model (BSM) theories, offering explanations for the symmetry between leptons and quarks. These theories include grand unified theories 4, 5, 6), technicolor models 7, 8), and compositeness frameworks 9, 10). LQs also feature in R-parity violating supersymmetry 11, 12, 13) and act as mediators in interactions between dark matter and the SM 14). These particles have been proposed as crucial elements for explaining fundamental symmetries and addressing unresolved questions in particle physics.

Leptoquarks (LQs) have attracted considerable attention for their potential to explain various anomalies observed in precision measurements. In particular, the $B \to D^*$ anomaly, reported by experiments such as BaBar 15, 16), Belle 17), and LHCb 18), has generated interest, with a possible explanation involving the mediation of an intermediate LQ scalar 19, 20). In a search for LQs coupling to τ leptons and b quarks, the CMS collaboration observed an excess with a significance of 2.8 standard deviations above the Standard Model (SM) expectation using Run 2 data 21). However, a similar search by the ATLAS collaboration showed results consistent with the SM prediction 22).

This article investigates LQ phenomena with additional jets, unveiling new production mechanisms and topologies in sections 2 and 3, respectively. In section 4, we propose a detection strategy that includes all relevant signal contributions, and in section 5, we evaluate the statistical significance of LQ couplings to $e-u$ and $\mu-c$ quark pairs for current and future LHC runs.

2 Nambu-Jona-Lasinio composite leptoquark model

The No-Go theorem 23) demonstrates that the SM fermion Lagrangian, in the context of a renormalizable quantum field theory at low infrared energies (IR), encounters theoretical inconsistencies with its chiral gauge symmetries and fermion spectra when a high-energy ultraviolet (UV) cutoff $\Lambda_{\rm cut}$ is imposed. Consequently, this necessitates the introduction of effective quadrilinear operators $G_{\rm cut}\bar\psi^f_L\psi^f_R\bar\psi^f_R\psi^f_L$ (where $G_{\rm cut}\propto\Lambda^{-2}_{\rm cut}$), resembling Nambu-Jona-Lasinio (NJL) or Einstein-Cartan interactions 1). These operators maintain SM gauge symmetry and involve left- and right-handed fermions (ψ^f_L, ψ^f_R) in the fermion family "f".

At strong coupling $g_{\rm cut} = G_{\rm cut}\Lambda^2_{\rm cut} > 1$, dynamics lead to the emergence of massive composite bosons $\Pi^f \sim (\bar\psi^f_R\psi^f_L)$ and fermions $F^f_R \sim \psi^f_R(\bar\psi^f_R\psi^f_L) \sim \psi^f_R\Pi^f$, which carry SM charges and interact with massless SM gauge bosons in a gauge-invariant manner. This effective theory, which respects SM gauge symmetry and is renormalizable, operates within the scaling domain of the UV fixed point $g^*_{\rm cut}$ at a composite scale $\Lambda \ll \Lambda_{\rm cut}$ 24).

As the energy scale drops below Λ, the effective theory undergoes a phase transition 25) where composite particles decay into their constituents, and spontaneous breaking of SM symmetries occurs through processes such as the top-quark channel $(\bar t_L t_R \bar t_R t_L)$, leading ultimately to the Standard Model manifesting at the electroweak scale $v \approx 246$ GeV 26). The scale $\Lambda = \mathcal{O}(\text{TeV})$ is estimated based on the masses of the top quark and Higgs boson, and extrapolations from the renormalization-group solutions into the high-energy regime 27).

Under consideration composite boson states $\Phi \sim (\bar\ell_R q_L)$ with fractional electric charge, or LQ, are listed in Table 1. The effective coupling between a LQ composite boson and its two constituents can be written as effective contact interactions,

$$\mathcal{L}_{CI} = g_{\Pi_{5/3}}(\bar e_R u_{La})\Pi_a^{-5/3} + g_{\Pi_{1/3}}(\bar\nu^e_R d_{La})\Pi_a^{1/3} + g_{\Pi_{-2/3}}(\bar\nu^e_R u_{La})\Pi_{u_a}^{-2/3} + g_{\Pi_{-2/3}}(\bar e_R d_{La})\Pi_{d_a}^{-2/3} + \text{h.c.} \quad (1)$$

where the LQ effective Yukawa coupling $g_{\Pi_i} = (F_{\Pi_i}/\Lambda)^2 \sim \mathcal{O}(1)$.

Bosons Π_a^Q	Charge $Q_i = Y + t^i_{3L}$,	$SU_L(2)$ 3-isospin t^i_{3L},	$U_Y(1)$ charge Y,	$SU_c(3)$ color a
$\Pi_a^{+5/3} \propto \bar{e}_R u_{La}$	$+5/3$	$+1/2$	$+7/6$	3
$\Pi_a^{-1/3} \propto \bar{\nu}_R^e d_{La}$	$-1/3$	$-1/2$	$+1/6$	3
$\Pi_{u_a}^{+2/3} \propto \bar{\nu}_R^e u_{La}$	$+2/3$	$+1/2$	$+1/6$	3
$\Pi_{d_a}^{+2/3} \propto \bar{e}_R d_{La}$	$+2/3$	$-1/2$	$+7/6$	3

Table 1: Composite bosons, their constituents, standard model charges for the first generation of the standard model fermions.

3 Signal implementation and samples generation

We generate signal and background events using MadGraph5 aMC@NLO [28], incorporating interaction terms from the previous section via the Feynrules package [29] as a Universal FeynRules Output (UFO) module [30], which is published on the official Feynrules website [31]. Monte Carlo (MC) samples for both signal and SM background processes are created with MadGraph5 aMC@NLO. Following this, we utilize Pythia 8.2 [32] to implement initial and final parton showering and fragmentation.

We examine LQs with a charge of 5/3 that couple to electron-u quark and muon-c quark pairs for the signal generation. The signal process is generated with two types of beam hypotheses: proton-proton (pp) and photon-proton (γp). For the pp LQ production, the NNPDF31-lo-as-0118 [33] PDF is used. For the γp collisions, we choose the MRST2004qed-proton PDF [34], and is motivated by our aim to distinguish between the elastic and inelastic contributions of the photon. The NNPDF set previously mentioned incorporates both the elastic and inelastic contributions. The MRST2004qed PDF allows for the separation of the elastic and inelastic contributions with the configurations available in Madgraph. We simulate the processes $pp \to \ell^+\ell^-$ with 0, 1, 2, or at least 3 partons to account for the standard production modes depicted in Fig. 1 (a-c). Additionally, examples of new production modes are illustrated in Fig. 1 (d-f), where Fig. 1 (d) shows a γp collision involving an inelastic contribution. For photon-induced processes, we specifically analyze $\gamma p \to \ell^+\ell^-$ with 1 parton, focusing solely on the inelastic contribution.

The center-of-mass energy is fixed at 13 TeV, with coupling values varying from 0.5 to 2.5 in increments of 0.5, and LQ masses considered in the ranges (in TeV) of [1.00-2.00] in steps of 0.25, [2.00, 10.00] in steps of 0.50, and including 20.00 and 30.00 TeV. Extra jets in LQ production can come from either gluons or quarks, with gluons arising from initial or final state radiation in standard tree-level diagrams, and quarks potentially introducing new LQ production mechanisms. Both scenarios contribute to the signal, so to avoid double counting, we use the MLM matching technique [35] with a 30 GeV matching scale and proper overlap removal in jet rates. Background events are generated at leading order (LO) using the NNPDF31-lo-as-0118 PDF and scaled to next-to-leading-order (NLO) cross-sections as needed, covering processes such as W + jets, Drell-Yan + jets, single top, $t\bar{t}$, and diboson events (WW, WZ, ZZ).

4 Analysis Strategy

The signal we look for produces a signature with two leptons in the final state plus a given number of jets (0, 1, 2, or at least 3). The samples described in previous section are used in the event selection. The events pass the signal selection if they satisfy the following baseline requirements for the LQ coupling. These criteria include the following:

- Exactly two electrons (for eu) or muons (for μc) with transverse momentum $p_{\mathrm{T}} > 20$ GeV and pseudorapidity $|\eta| < 2.5$.

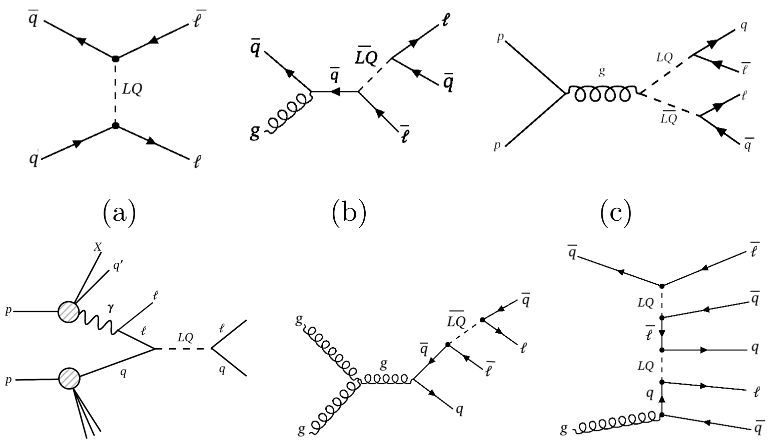

Figure 1: *Examples of Feynman diagrams for the t-channel (a), single (b), pair (c), Inelastic γp single production (d), and example of new production modes (e,f).*

- The invariant mass of the two leptons must exceed 120 GeV, a requirement implemented to diminish the presence of Drell-Yan SM contamination.
- The missing transverse energy should be less than 50 GeV.
- No jets originating from b quarks are allowed, aiming to reduce the impact of events associated with top quarks.
- Jets are specifically chosen based on two criteria: a transverse momentum (p_{T}) greater than 20 GeV and a pseudorapidity ($|\eta|$) less than 5. Additionally, these jets must be spatially separated from the selected muons by an angular distance, denoted as ΔR, which satisfies $\Delta R > 0.4$. The angular distance is defined as:

  $$\Delta R = \sqrt{(\Delta\eta)^2 + (\Delta\phi)^2} \tag{2}$$

  Here, $\Delta\eta$ represents the difference in pseudorapidity, and $\Delta\phi$ is the difference in azimuthal angle. The imposed conditions ensure that the selected jets are sufficiently distinct from the muons. It's noteworthy that no specific requirement is set regarding a minimum number of jets. Instead, events in the signal region are categorized based on the jet count, with separate categories for 0, 1, 2, or at least 3 jets. This approach allows for a flexible analysis, accommodating events with varying jet multiplicities.

The distribution derived from pp events involving two jets, plotted in the two-dimensional plane of variables χ and $\mathrm{S_T}$. The variable χ is defined as:

$$\chi = e^{|\eta_1 - \eta_2|} \tag{3}$$

Here, η_1 and η_2 represent the pseudorapidities of the two leptons. Additionally, $\mathrm{S_T}$ is defined as the sum of the scalar transverse momenta of the leptons and selected jets:

$$\mathrm{S_T} = \sum_{\mathrm{leptons}} \mathrm{p_{T,\,lepton}} + \sum_{\mathrm{jets}} \mathrm{p_{T,\,jet}} \tag{4}$$

5 Sensitvity Studies at LHC and HL-LHC

We utilize the distributions of the χ and $\mathrm{S_T}$ variable for each jet multiplicity in the signal regions. These distributions serve as the ultimate discriminant between the LQ signal and the background. The interpretation of signal events, both combined and separately from pp and γp collisions, takes into account factors such as production cross-section, efficiency, and luminosity. To assess the expected signal significance, we employ a profile-binned likelihood statistical test, as outlined in 36). The "Combine Tool" 37) is employed to calculate the expected significance.

Nuisance parameters encompassing systematic uncertainties are introduced for the signal (background), incorporating log-normal priors. We follow the same prescriptions used in the published LQ searches 38, 40). Subsequently, we will present the significance results for luminosities of 300 fb^{-1} and scaled to 140 fb^{-1} and 3000 fb^{-1}.

5.1 Results for pp and γp Combine

For the analysis of LQs for merged samples, we examine the sensitivity considering the eu and μc couplings. The results are obtained by combining signals from pp and γp collisions. In Fig. 2, we present 2 and 5σ significance contours corresponding to the eu and μc couplings across different luminosity levels. The green contours represent 3000 fb^{-1}, with solid lines for 5σ and dashed lines for 2σ. The red contours correspond to 300 fb^{-1}, and the blue contours represent 140 fb^{-1}, with solid lines for 5σ and dashed lines for 2σ.

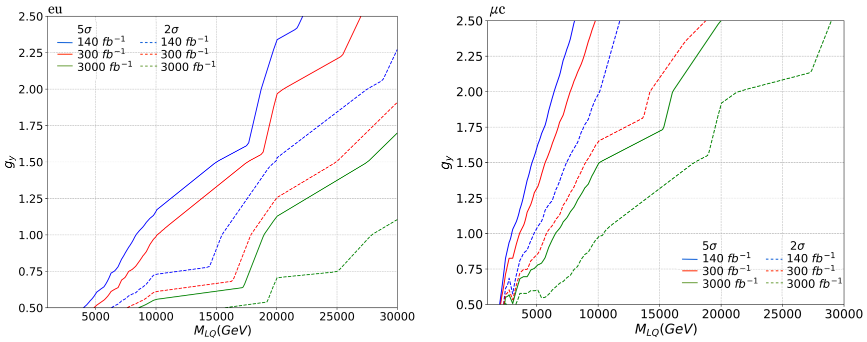

Figure 2: *Contour lines at 2 and 5σ for the expected signal significance for different couplings and LQ masses. The estimates are performed at $\sqrt{s}$ = 13 TeV, 140 fb^{-1}, 300 fb^{-1} and 3000 fb^{-1}.*

5.2 Comparison with CMS and ATLAS Results

In Fig. 3, we depict the confidence levels derived from CMS and ATLAS for the μc generation. The contour plots in the left panel showcase the expected significance in the two-dimensional space defined by the coupling and the mass of the LQ. These plots are generated at a COM energy of 13 TeV and an integrated luminosity of 300 fb^{-1}. The right panel extends the analysis by considering varying luminosity assumptions, namely 140 (blue), 300 (red), and 3000 (green) fb^{-1}, for both the 5σ (solid line) and 2σ (dashed line) significance levels.

The vertical lines in both panels represent the most recent exclusion limits at a 95% confidence level from ATLAS 39) (black dashed) and CMS 40) (violet solid), scaled for 300 (left) and 3000 (right) fb^{-1}. The exclusive LQ approach yields 5σ (2σ) significance for LQ masses reaching 2.0, 2.2, 2.5 (2.3, 2.4, 3.4) TeV at 140, 300, and 3000 fb^{-1}, respectively, for coupling values of 0.5 and 2.5. Comparatively, the scaled results from ATLAS and CMS would exclude an LQ coupling to a muon-charm quark pair up to masses of 1.7, 1.8, 2.2, and 1.8, 1.9, 2.3 TeV, regardless of the coupling value and for the same luminosity scenarios.

Finally we can comment that the 2σ significance achieved with 140 fb^{-1} is comparable to the scaled upper limit on the LQ mass expected by ATLAS and CMS with 3000 fb^{-1}, specifically for the lowest considered coupling value.

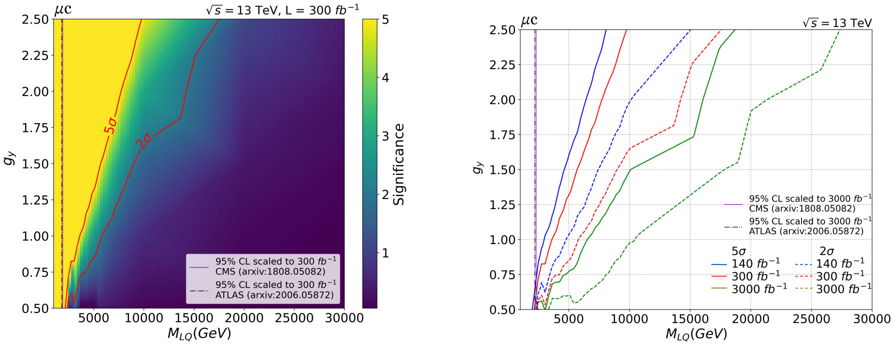

(a) (b)

Figure 3: *Signal significance in the plane of the coupling μc and the mass of the LQ using pp and γp events at $\sqrt{s} = 13$ TeV expected for 300 fb^{-1} (left) and different luminosity scenarios (right). The colored solid and dashed lines represent 5 and 2 σ levels for the analysis presented in this text. While the vertical lines show the most recent exclusion limits results at 95% confidence level from a search for LQs from ATLAS [39] (black dashed) and CMS [40] (violet plain) collaborations scaled for 300 (left) and 3000 (right) fb^{-1}.*

6 Summary

In our study, we thoroughly investigate LQ particles, focusing on a novel scenario involving LQ composite particles through the NJL-Composite model with effective strong four-fermion couplings. Unlike previous analyses that concentrate on primary LQ production modes, we explore the impact of additional jet associations, revealing new mechanisms beyond classical pair, single, and Drell-Yan non-resonant LQ generation. We introduce a global strategy for t-channel, single, and pair signal generation at different jet multiplicities, incorporating observables like event energy (S_T) and angular (χ) distributions. The significance of 2σ with 140 fb^{-1} is comparable to the scaled upper limit on LQ mass expected by ATLAS and CMS with 3000 fb^{-1} for the lowest considered coupling value.

7 Acknowledgements

We thank the organizers of the XXI LNF Spring School "Bruno Touschek" in Nuclear, Subnuclear, and Astroparticle Physics for the opportunity to present this work.

References

1. S.-S. Xue, "$SU(2)_L \times U(1)_Y$ symmetry and fermion masses," Phys. Lett. B 398, 177-183 (1997).
2. S.-S. Xue, "Vector-like composite fermions in the Standard Model," Phys. Lett. B 735, 188 (2014).
3. S.-S. Xue, "Ultraviolet Fixed Point and the Emergence of Composite Fermions," Phys. Rev. D 93, 076006 (2016).
4. J. C. Pati and A. Salam, "Unified Lepton-Hadron Symmetry and a Gauge Theory of the Basic Interactions," Phys. Rev. D 8, 1240 (1973).
5. J. C. Pati and A. Salam, "Lepton Number as the Fourth Color," Phys. Rev. D 10, 275 (1974).
6. H. Georgi and S. L. Glashow, "Unity of All Elementary Particle Forces," Phys. Rev. Lett. 32, 438 (1974).
7. S. Dimopoulos and L. Susskind, "Mass Without Scalars," Nucl. Phys. B 155, 237 (1979).
8. S. Dimopoulos, "Technicolored Signatures," Nucl. Phys. B 168, 69 (1980).
9. T. M. Morris et al., "Light Scalar Leptoquarks," Phys. Rev. D 47, 831 (1993).
10. B. Gripaios, "Composite Leptoquarks at the LHC," JHEP 0902, 053 (2009).
11. R. Barbier et al., "R-Parity Violating Supersymmetry," Phys. Rept. 420, 1 (2005).
12. G. R. Farrar and P. Fayet, "Phenomenology of the Production, Decay, and Detection of New Hadronic States Associated with Supersymmetry," Phys. Lett. B 76, 575 (1978).
13. P. Ramond, "Dual Theory for Free Fermions," Phys. Rev. D 3, 2415 (1971).
14. M. J. Baker et al., "The Coannihilation Codex," JHEP 12, 120 (2015).
15. BaBar Collaboration, "Evidence for an excess of $\bar{B} \to D^{(*)}\tau^-\bar{\nu}_\tau$ decays," Phys. Rev. Lett. 109, 101802 (2012).
16. BaBar Collaboration, "Measurement of an Excess of $\bar{B} \to D^{(*)}\tau^-\bar{\nu}_\tau$ Decays and Implications for Charged Higgs Bosons."
17. Belle Collaboration, "Measurement of the branching ratio of $\bar{B} \to D^{(*)}\tau^-\bar{\nu}\tau$ relative to $\bar{B} \to D^{(*)}\ell^-\bar{\nu}\ell$ decays with hadronic tagging at Belle," Phys. Rev. D 92, no. 7, 072014 (2015).
18. LHCb Collaboration, "Measurement of the ratio of branching fractions $\mathcal{B}(\bar{B}^0 \to D^+\tau^-\bar{\nu}_\tau)/\mathcal{B}(\bar{B}^0 \to D^+\mu^-\bar{\nu}_\mu)$," Phys. Rev. Lett. 115, no. 11, 111803 (2015).
19. T. Mandal, S. Mitra, and S. Raz, "$R_{D^{(*)}}$ motivated $\mathcal{S}_1$ leptoquark scenarios: Impact of interference on the exclusion limits from LHC data," *Phys. Rev. D*, **99**, 055028 (2019), doi: 10.1103/PhysRevD.99.055028.
20. S. Iguro, T. Mandal, and H. Yonaha, "Revisiting $\mathcal{S}_1$ leptoquark solutions to the $R_{D^{(*)}}$ anomaly with and without vector-like fermions," *Phys. Lett. B*, **841**, 137919 (2023), doi: 10.1016/j.physletb.2023.137919.

21. A. Hayrapetyan *et al.* [CMS Collaboration], "Search for a third-generation leptoquark coupled to a τ lepton and a b quark through single, pair, and nonresonant production in proton-proton collisions at $\sqrt{s} = 13$ TeV," arXiv:2308.07826 [hep-ex], Aug. 2023, CMS-EXO-19-016, CERN-EP-2023-144.

22. ATLAS Collaboration, "Search for leptoquarks decaying into the bτ final state in pp collisions at $\sqrt{s} = 13$ TeV with the ATLAS detector," arXiv:2305.15962 [hep-ex], May 2023, CERN-EP-2023-033.

23. H. B. Nielsen and M. Ninomiya, "No Go Theorem for Regularizing Chiral Fermions," *Phys. Lett. B*, **105**, 219–223 (1981), doi: 10.1016/0370-2693(81)91026-1, RL-81-052.

24. S. S. Xue, "Ultraviolet fixed point and massive composite particles in TeV scales," *Phys. Lett. B*, **737**, 172–177 (2014), doi: 10.1016/j.physletb.2014.08.031, arXiv:1405.1867 [hep-th].

25. S. S. Xue, "Higgs boson origin from a gauge symmetric theory of massive composite particles and massless W± and Z0 bosons at the TeV scale," *Nuclear Phys. B*, **990**, 116168 (2023), doi: 10.1016/j.nuclphysb.2023.116168, `http://dx.doi.org/10.1016/j.nuclphysb.2023.116168`.

26. W. A. Bardeen, C. T. Hill, and M. Lindner, "Minimal Dynamical Symmetry Breaking of the Standard Model," *Phys. Rev. D*, **41**, 1647 (1990), doi: 10.1103/PhysRevD.41.1647, report number: FERMILAB-PUB-89-127-T.

27. S. S. Xue, "Higgs boson and top-quark masses and parity-symmetry restoration," *Phys. Lett. B*, **727**, 308–313 (2013), doi: 10.1016/j.physletb.2013.10.024.

28. J. Alwall, M. Herquet, F. Maltoni, O. Mattelaer, and T. Stelzer, "MadGraph 5: Going Beyond," *J. High Energy Phys.*, **2011**, no. 06, 128 (2011), doi: 10.1007/JHEP06(2011)128, arXiv:1106.0522 [hep-ph], FERMILAB-PUB-11-448-T.

29. A. Alloul, N. D. Christensen, C. Degrande, C. Duhr, and B. Fuks, "FeynRules 2.0 - A complete toolbox for tree-level phenomenology," *Comput. Phys. Commun.*, **185**, 2250–2300 (2014), doi: 10.1016/j.cpc.2014.04.012, arXiv:1310.1921 [hep-ph].

30. C. Degrande, C. Duhr, B. Fuks, D. Grellscheid, O. Mattelaer, and T. Reiter, "UFO - The Universal FeynRules Output," *Comput. Phys. Commun.*, **183**, 1201–1214 (2012), doi: 10.1016/j.cpc.2012.01.022, arXiv:1108.2040 [hep-ph].

31. NJL Composite Model Implementation in Feynrules, `https://feynrules.irmp.ucl.ac.be/wiki/NJLComposite`.

32. T. Sjöstrand, S. Ask, J. R. Christiansen, R. Corke, N. Desai, P. Ilten, S. Mrenna, S. Prestel, C. O. Rasmussen, and P. Z. Skands, "An introduction to PYTHIA 8.2," *Comput. Phys. Commun.*, **191**, 159–177 (2015), doi: 10.1016/j.cpc.2015.01.024, arXiv:1410.3012 [hep-ph].

33. R. D. Ball *et al.* [NNPDF Collaboration], "Parton distributions from high-precision collider data," *Eur. Phys. J. C*, **77**, 663 (2017), doi: 10.1140/epjc/s10052-017-5199-5, arXiv:1706.00428 [hep-ph].

34. A. D. Martin, R. G. Roberts, W. J. Stirling, and R. S. Thorne, "Parton distributions incorporating QED contributions," *Eur. Phys. J. C*, **39**, 155–161 (2005), doi: 10.1140/epjc/s2004-02088-7, arXiv:hep-ph/0411040.

35. M.L. Mangano, M. Moretti, F. Piccinini, and M. Treccani, "Matching matrix elements and shower evolution for top-quark production in hadronic collisions," *JHEP*, vol. 01, p. 013, 2007, doi: 10.1088/1126-6708/2007/01/013.

36. Particle Data Group, "Statistics," G. Cowan (ed.), (2021), [Online]. Available: `https://pdg.lbl.gov/2023/reviews/rpp2022-rev-statistics.pdf`.

37. CMS Collaboration, "Documentation of the RooStats-based statistics tools for Higgs PAG," [Online]. Available: `http://cms-analysis.github.io/HiggsAnalysis-CombinedLimit/`.

38. A. M. Sirunyan *et al.* [CMS Collaboration], "Search for pair production of first-generation scalar leptoquarks at $\sqrt{s} = 13$ TeV," *Phys. Rev. D*, vol. 99, no. 5, p. 052002, 2019, doi: 10.1103/PhysRevD.99.052002.

39. G. Aad *et al.* [ATLAS Collaboration], "Search for pairs of scalar leptoquarks decaying into quarks and electrons or muons in $\sqrt{s} = 13$ TeV pp collisions with the ATLAS detector," *JHEP*, vol. 10, p. 112, 2020, doi: 10.1007/JHEP10(2020)112.

40. A. M. Sirunyan *et al.* [CMS Collaboration], "Search for pair production of second-generation leptoquarks at $\sqrt{s} = 13$ TeV," *Phys. Rev. D*, vol. 99, no. 3, p. 032014, 2019, doi: 10.1103/PhysRevD.99.032014.

Frascati Physics Series Vol. 76 (2024)
8th young researchers' workshop 'Physics Challenges in the LHC Era'
May 13 and 16, 2024

The ITk pixel detector for the ATLAS Phase 2 Upgrade at HL LHC

Zaza Chubinidze on behalf of the ATLAS Collaboration
INFN e Laboratori Nazionali di Frascati (IT)
E-mail: zaza.chubinidze@lnf.infn.it

Abstract

The ATLAS Phase-II upgrade, particularly the Inner Tracker (ITk) pixel detector project for the High-Luminosity Large Hadron Collider (HL-LHC), aims to enhance the capabilities of the ATLAS experiment to handle higher collision rates and extreme radiation levels. The ITk pixel detector will replace the current ATLAS Inner Detector with a full silicon-based tracker. It is designed to provide high granularity, precision, and radiation resistance, with improvements in tracking performance, especially in environments with higher pile-up events. The ITk incorporates a more advanced layout and material design, significantly reducing the material budget to enhance tracking efficiency and resolution. The use of serial powering, lightweight materials, and a cooling system ensures the system's ability to operate under the challenging conditions of the HL-LHC. The upgrade includes pixel modules with advanced sensors and electronics, specifically designed to endure high radiation doses while maintaining high detection efficiency. The ITk's development and integration are part of a global collaboration, with installation planned for 2026. The ITk is expected to significantly improve the physics performance of the ATLAS detector in the HL-LHC era.

1 Introduction

The Phase-II upgrade of the Large Hadron Collider (LHC) [1] aims to push the boundaries of particle physics by providing more powerful tools for scientific exploration. Key goals include exploring the Higgs boson in greater detail and searching for new particles beyond the Standard Model.

The High-Luminosity Large Hadron Collider (HL-LHC) [2] phase, starting in 2029, will offer proton-proton collisions at energies up to 14 TeV, with integrated luminosities of $3000\,\mathrm{fb}^{-1}$ to $4000\,\mathrm{fb}^{-1}$. This increase will enable deeper investigations of particle interactions. Additionally, the upgrade will lead to a 5-7 times higher instantaneous luminosity, raising the number of simultaneous particle interactions (pile-up events) to 200 per bunch crossing. Higher particle densities will require improved detector granularity and faster data processing. Radiation damage will also increase with fluences reaching up to $2 \times 10^{16}\, \text{n}_{\text{eq}}/\text{cm}^2$ and total ionizing doses of up to 10 MGy, where necessitating new radiation-resistant technologies, as current Inner Detector (ID) will not stand up to the demanding conditions of HL-LHC.

2 The ATLAS Inner Tracker Detector

Upgrade of the ID to the new Inner Tracker (ITk) for the ATLAS experiment 3), is a critical part of the HL-LHC project. The ITk will replace the current ATLAS ID with a full silicon-based tracker designed to withstand the harsh conditions of the HL-LHC. Spanning a radius of 1 meter and a length of 6 meters, it will feature both strip 4) and pixel 5) detectors. The ITk consists of pixel and strip sections (Figure 1), detailed in substructures such as the outer barrel, end-caps, and inner system, providing high granularity, precision, and radiation resistance.

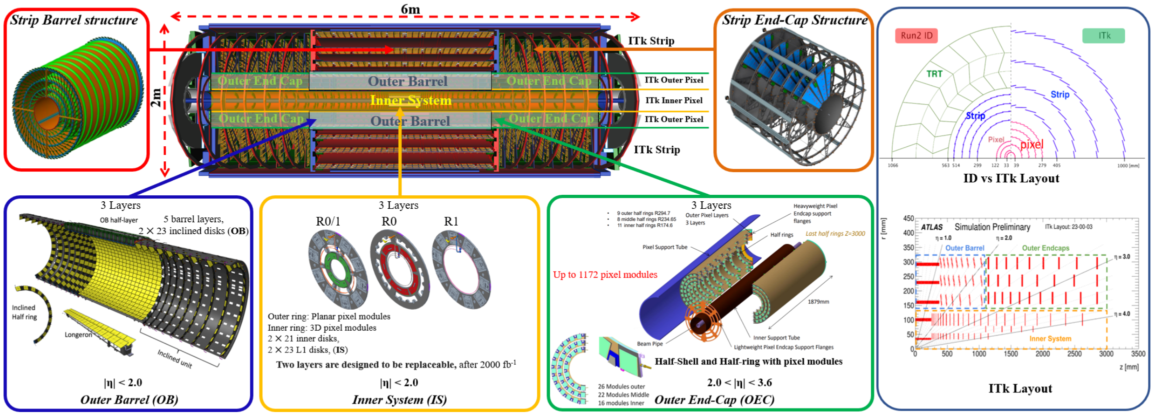

Figure 1: *ATLAS ITk with Sub detectors and layout.*

The pixel section, with five-barrel layers and multiple disk structures, ensures superior spatial resolution, while the strip detectors provide extensive coverage and rapid data processing. Designed to cope with the 1 MHz trigger rate of the HL-LHC, the ITk ensures low mass for cooling and mechanical support, achieving high data granularity with minimal occupancy (< 1%) even under extreme radiation. ITk detector upgrade summary is shown in Table 1.

ITk (ID)	Area (m^2)	# Modules	# Channels (M)	L0 Trigger rate	Pseudo-rapidity $\lvert\eta\rvert$	Maximum fluence ($\text{n}_{\text{eq}}/\text{cm}^2$)
Pixels	∼ 13 (1.9)	∼ 9700 (2000)	∼ 5100 (92)	1 MHz (100 kHz)	< 4 (< 2.5)	$2 \times 10^{16}\, \text{n}_{\text{eq}}/\text{cm}^2$ ($10^{14}\, \text{n}_{\text{eq}}/\text{cm}^2$)
cline1-7 **Strips**	∼ 165 (61)	∼ 17888 (4088)	∼ 60 (6.3)	1 MHz (100 kHz)	< 2.7 (< 2.5)	$1.6 \times 10^{15}\, \text{n}_{\text{eq}}/\text{cm}^2$ ($2 \times 10^{14}\, \text{n}_{\text{eq}}/\text{cm}^2$)

Table 1: *ITk Upgrade summary (The parameters for the ID are reported in parenthesis)*

3 ITk Detector Performances

The ITk detector is a key component of the ATLAS experiment's where primary focus is on the detector's layout, material reduction, and performance improvements, which are crucial for operating under the high interaction rates and radiation levels of the HL-LHC.

The layout of the ITk Detector, depicted in the (Figure 2), shows the structure of one-quarter of the detector. It is designed with several layers, including the outer barrel and endcaps, each covering different pseudo-rapidity ranges. This structure ensures that the detector can efficiently track particles

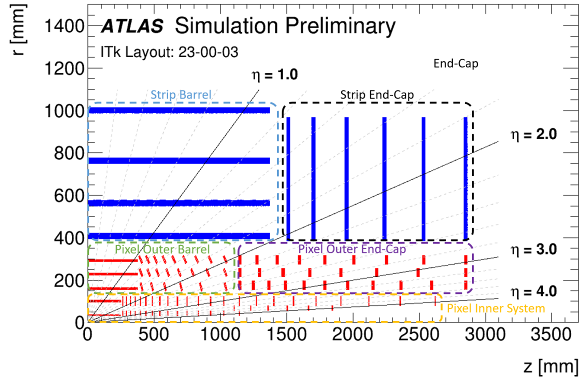

Figure 2: *One quarter of the ITk pixel layout*

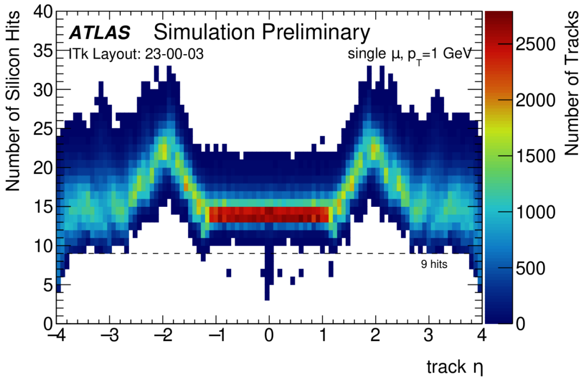

Figure 3: *Number of strip plus pixel measurements on a track as a function of* η *for single muons events with* $pT = 1$ *GeV*

over a wide range of angles and the distribution of silicon hits per track for single muon events (Figure 3) ensuring that the detector provides at least nine hits per track in the barrel region and thirteen in the endcaps. This configuration enables highly accurate tracking, especially in areas of high pseudo-rapidity.

The emphasis on reducing the material within the detector is highlighted as a key factor in improving performance, particularly for low-momentum particles. By using lightweight materials such as carbon fiber for support structures, thin titanium pipes for cooling, and employing serial powering, the material budget has been significantly reduced. This reduction is critical for minimizing interactions between particles and the detector, which enhances both tracking 6) efficiency and resolution. A comparison of radiation lengths between the previous Run 2 detector and the ITk shows a substantial improvement, with the ITk offering at least a factor of two reduction in radiation length (Figure 4).

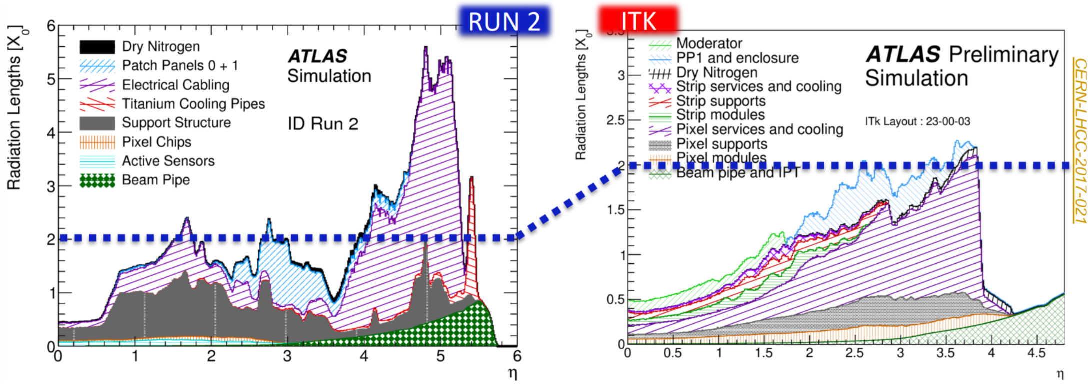

Figure 4: *Low-mass materials of the detector, to reduce radiation length* $[X_0]$

In terms of tracking performance, the ITk Detector is designed to deliver precise measurements, even under challenging conditions.

Charged particle track reconstruction involves determining key parameters of the particle's trajectory, represented as $q = (d_0, z_0, \phi, \theta, q/p)$. These parameters include the transverse impact parameter (d_0), longitudinal impact parameter (z_0), azimuthal angle (ϕ), polar angle (θ), and the charge-to-momentum ratio (q/p).

The ITk significantly improves the resolution of d_0, which is crucial for reconstructing long-lived particles. Performance comparisons between the ITk and the Run 2 detector reveal that the ITk offers superior resolution for d_0 particularly at higher pseudo-rapidity values. This improvement is largely due to the smaller pixel pitch size and the reduced amount of material in the detector.

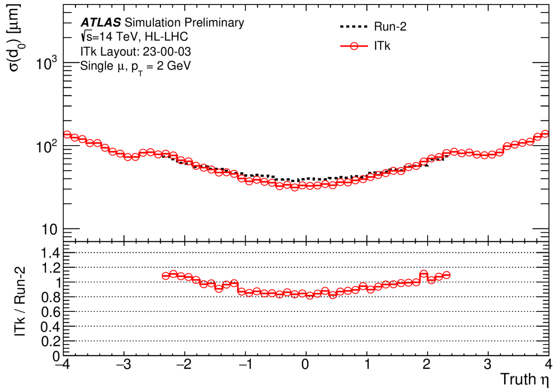

Figure 5: *Transverse impact parameter* (d_0) *resolution vs.* η *for 2 GeV muons without pileup, comparing Run 2 detector and updated ITk layout.*

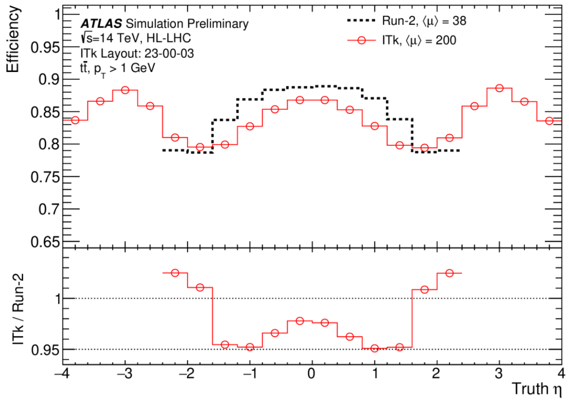

Figure 6: *Tracking efficiency for* $t\bar{t}$ *events at* $\langle\mu\rangle = 200$ *with the updated ITk layout compared with the Run 2 detector at* $\langle\mu\rangle = 38$.

The (Figure 6) illustrates a comparison of tracking efficiency for $t\bar{t}$ events between the updated ITk layout and the Run 2 detector. It shows tracking efficiency as a function of the pseudorapidity (η) for two different pile-up conditions. The red solid line represents the ITk performance at $\langle\mu\rangle = 200$, indicating high pile-up, while the black dashed line represents the Run 2 detector at $\langle\mu\rangle = 38$, reflecting lower pile-up conditions. The ITk exhibits superior or comparable tracking efficiency across all pseudorapidity values, with particularly notable improvements in the central region around $\eta = 0$. In the lower portion of the (Figure 6), the ratio of the ITk's efficiency to that of the Run 2 detector is plotted. This highlights that the ITk offers improved performance, especially in the forward pseudorapidity regions (higher $|\eta|$), where tracking is more challenging due to higher particle densit. Overall, the ITk shows enhanced tracking efficiency under high pile-up conditions, providing a significant upgrade over the Run 2 detector, especially in regions with higher pseudorapidity.

In conclusion, the ITk Detector upgrade represents a significant advancement for the ATLAS experiment, combining material reduction, improved tracking precision, and high efficiency to meet the demands of the HL-LHC.

4 The ITk Pixel modules

The ITk Pixel modules $^{7)}$, are a key component of the upgraded ITk for the ATLAS experiment at the HL-LHC. These pixel modules are designed with advanced technology to meet the high demands of radiation hardness and precise detection.

The sensors and front-end (FE) $^{8)}$ electronics are designed in collaboration with the RD53 project, utilizing 65 nm CMOS technology. The pixel modules consist of both 3D and planar sensors (Figure 7), bump-bonded to the pixel readout ASICs (Figure 8). The 3D structured pixel sensors are used in the innermost layers due to their better radiation hardness and lower power dissipation, while the planar sensors are used in other layers, providing flexibility and performance across different regions of the detector.

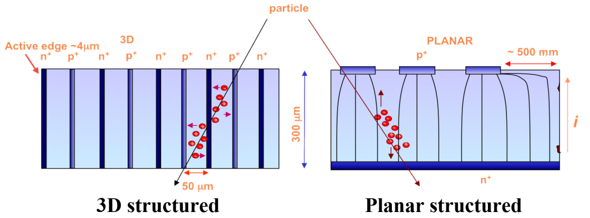

Figure 7: *Pixel Sensor Technologies.*

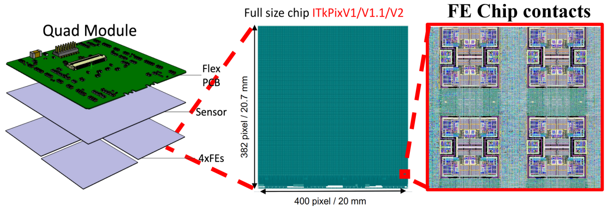

Figure 8: *Quad module with Front-End readout chip*

The n-in-p structured sensors provide excellent radiation hardness, with the ITk pixel layer 0 sensors being notably compact at $25 \times 100\,\mu\text{m}^2$, ensuring enhanced resolution and performance in high-radiation environments. The modules are built in a quad structure, with each sensor measuring 40 × 40 mm and integrated with 4 FE ASICs. These compact designs are essential for achieving the necessary performance while managing the increased particle flux expected at the HL-LHC. A critical aspect of these pixel modules is their high efficiency. The hit efficiency of the ITk-Pixel exceeds 97% at a bias voltage of 40V, demonstrating excellent performance under high radiation conditions.

5 The pixel Outer End-Cap integration at LNF

The Pixel Outer End-Cap integration at the ”Laboratori Nazionali di Frascati” (LNF) features a 3.5 meter long structure composed of multiple layers containing Half-Rings (HRs) (Figure 9). Each HR supports a serial-powering chain, delivering power and monitoring through a bus tape. A titanium pipe integrated into the Half-Ring structure facilitates heat removal via a CO_2 cooling system. The CO_2 evaporation temperature is set at -30°C.

The End-Cap (Figure 11) consists of three Layer Half-Shells (HS) (Figure 10): Layer 2 with 11 HRs, Layer 3 with 8 HRs, and Layer 4 with 9 HRs, totaling 1172 modules across all layers.

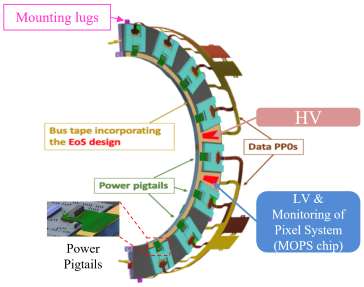

Figure 9: *Half-Ring with pixel modules and services*

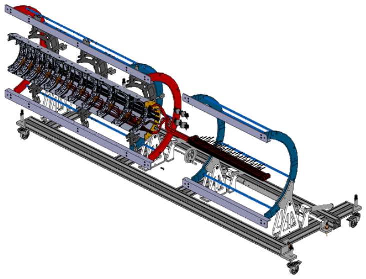

Figure 10: *End-Cap HRs loaded Half-Shell layer with trolley.*

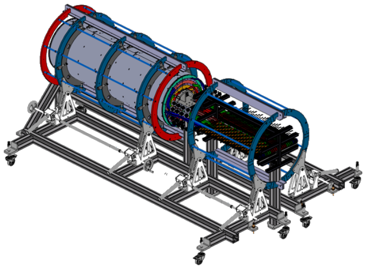

Figure 11: *Full End-Cap layers with trolley*

The clean room (ISO 6 standards) for End-Cap integration at LNF hosts, supports mechanical assembly, electrical testing, cooling and large climate chamber. It includes facilities for CO_2 cooling, dry air, and nitrogen distribution. Detector prototypes are currently undergoing system testing at Frascati.

6 Conclusion

The design and construction of the new ATLAS tracker for the HL-LHC phase presents significant challenges due to the harsher operating conditions, but it is expected to deliver comparable or even improved physics performance. The new all-silicon tracking system is being developed to handle the increased event rates and radiation levels. Installation of the ITk detector will begin in 2026, and the design offers large acceptance for tracking with high granularity and radiation hardness. Both strips and pixel technologies have demonstrated efficient performance up to the required end-of-life radiation doses. The production of the ITk will be a global collaboration, involving over fifty institutes worldwide.

7 Acknowledgements

The authors acknowledge the contributions of the ATLAS ITk Pixel Collaboration and I would like to thank to Marianna Testa (LNF) for her guidance throughout this work. Special thanks also go to the organizing committee of the XXI LNF Spring School at LNF for the opportunity to present this work.

References

1. L. Evans and P. Bryant, LHC machine, 2008 JINST 3 S08001. URL: `https://iopscience.iop.org/article/10.1088/1748-0221/3/08/S08001`
2. High-Luminosity Large Hadron Collider (HL-LHC), Technical Design Report, URL: `https://cds.cern.ch/record/2284929/files/40-39-PB.pdf`
3. ATLAS Collaboration, The ATLAS Experiment at the CERN Large Hadron Collider, JINST 3 (2008) S08003 URL: `https://cds.cern.ch/record/1129811/files/jinst8\_08\_s08003.pdf`
4. ATLAS Collaboration, ATLAS Inner Tracker Strip Detector: Technical Design Report, ATLAS-TDR-025; CERN-LHCC-2017-005, 2017, URL: `https://cds.cern.ch/record/2257755/files/ATLAS-TDR-025.pdf`
5. ATLAS Collaboration, The ATLAS Inner Tracker Pixel Detector: Technical Design Report for, CERN-LHCC-2017-021, ATLAS-TDR-030, URL: `https://cds.cern.ch/record/2285585/files/ATLAS-TDR-030.pdf`
6. ATLAS Collaboration, Expected tracking and related performance with the updated ATLAS Inner Tracker layout at the High-Luminosity LHC, ATLAS PUB Note; ATL-PHYS-PUB-2021-024, URL: `https://cds.cern.ch/record/2776651/files/ATL-PHYS-PUB-2021-024.pdf`
7. The ATLAS ITk Group 2022 JINST 17 C03042, Module development for the ATLAS ITk pixel detector, URL: `https://iopscience.iop.org/article/10.1088/1748-0221/17/03/C03042/pdf`
8. RD53 collaboration, RD53B manual, Tech. Rep., CERN, Geneva (2019), URL: `https://cds.cern.ch/record/2665301`

Frascati Physics Series Vol. 76 (2024)
8TH YOUNG RESEARCHERS' WORKSHOP 'PHYSICS CHALLENGES IN THE LHC ERA'
May 13 and 16, 2024

Mu2e calorimeter: in situ calibration of energy and time with selected Cosmic Ray samples

Pierluigi Fedeli
Laboratori Nazionali di Frascati dell'INFN, Frascati, Italy
Università degli Studi di Roma "La Sapienza", Roma, Italy

on behalf of the Mu2e calorimeter group

Abstract

The Mu2e electromagnetic crystal calorimeter is a state-of-art detector that will play a crucial role in detecting the signal of a neutrino-less muon to electron conversion that the Mu2e experiment will explore. The calibration in time and energy of the calorimeter is necessary to match the requirements and will serve as monitoring during the operations. In this article, we present the results of our calibration study in energy and time for the Mu2e crystal calorimeter as well as the time-scale inter-calibration between the tracker and the calorimeter using simulated cosmic rays in the configuration where both the detectors are placed outside the detector solenoid, named extracted position.

1 Introduction

The Mu2e experiment 1) is under construction at the Fermilab National Accelerator Laboratory and will explore physics beyond the Standard Model (BSM) through the search for the charged lepton flavor violation (CLFV) process of a neutrino-less conversion of a muon into an electron in the field of an aluminum nucleus. The Mu2e experiment plans to improve the current best limit by four orders of magnitude 2) reaching an upper limit value $< 6.2 \times 10^{-16}$ at 90% C.L.

The final state of the conversion process is a monoenergetic electron with an energy of approximately 105 MeV which will be detected by a high-resolution straw tracker and an undoped CsI crystal calorimeter. Both the detectors are inserted in a solenoid which provides a 1T magnetic field and the whole detector region is surrounded by the highly-efficient Cosmic Ray Veto which will suppress the cosmic ray (CR) background.

A pulsed beam of 8 GeV protons will strike a tungsten target; the produced pions will be sign-selected and guided through an S-shape system of solenoids where they will decay and be captured by the aluminum atoms in the Muon Stopping Target (MST). The normalization of the CLFV events is calculated with the

Stopping Target Monitor (STM) composed of the High Purity Germanium Detector and the Lanthanum Bromide crystal detector which observe the X-rays emitted from the muonic atoms formed in the MST.

2 The electromagnetic crystal calorimeter

The electromagnetic calorimeter 3) must have a large acceptance for the conversion electron and a strong particle identification capability with a muon-electron rejection factor of 200. This results in requiring an energy resolution of $\mathcal{O}(10\%)$ and a time resolution of 500 ps for 100 MeV electrons. In addition, the calorimeter must have the capability to withstand a high-radiation environment up to 100 krad and 10^{12} $\mathrm{n_{1MeVeq}/cm^2}$ within a 10^{-4} torr vacuum.

The Mu2e calorimeter is arranged in two annular disks, each one composed of 674 undoped CsI scintillating crystals 3.4cm × 3.4cm × 20cm. Each crystal is read out by two custom UV-extended Silicon Photo-Multipliers (SiPMs) and each SiPM is connected to a Front-End Electronics board (FEE). Groups of 20 FEE are managed by the Mezzanine Board (MZB) which is the interface between the FEE, the voltage source, and a custom DIgitizer and ReAdout Controller (DIRAC) module.

The performance of the calorimeter and the technological choices were evaluated using a large-scale prototype composed of 51 crystals, named Module-0, which was assembled at Laboratori Nazionali di Frascati. At the Beam Test Facility in Frascati, Module-0 was tested with a 100 MeV electron beam, obtaining an energy resolution of 7% and a time resolution of 200 ps 4).

3 Calibration with simulated cosmic ray sample

In the official Mu2e simulation campaign, simulating the whole detector, two Monte Carlo generators, CRY 5) and CORSIKA 6) are used to generate cosmic ray data. Subsequently, the interaction processes are simulated using the Geant4 toolkit. 7) 8) 9)

For the calorimeter, the simulation considers a nominal Longitudinal Response Uniformity (LRU) of a few percent for the crystals, as derived from quality control assessments. The energy deposited within the calorimeter is translated into optical photons, and the signal is digitized using experimentally-acquired pulse shapes. This process includes a nominal Light Yield (LY) of 30 photoelectron/MeV, Poisson-distributed photostatistics fluctuations, SiPM response, and electronic noise levels equivalent to 150 keV. Crystal hits are organized into clusters by starting with the crystal that has the highest reconstructed energy and adding hits from adjacent crystals with similar relative timing.

3.1 Energy calibration

For the presented analysis, a dataset simulating 10 hours of cosmic ray flux incident on the two calorimeter disks is used. To select clean cosmic ray (CR) events, we require a candidate to have a minimum of 6 crystals hit with energy deposited of at least 15 MeV. The track of a cosmic ray event is then identified as the linear fit to the positions of the crystals above the energy threshold. CR candidates must have a $\chi^2/\mathrm{NDF} \leq 2.5$ for the linear fit. From the fit to the deposited-energy distribution (Fig. 1) we extract the most probable value (MPV) which is the corresponding calibration scale parameter for each crystal.

To simulate a real experimental environment, we apply a random offset of up to ±10% to each crystal. The calibrated energy response of readout channels is defined as:

$$E_{\mathrm{calibrated}} = \frac{E_{\mathrm{smeared}}}{\mathrm{MPV}} \cdot 20\ \mathrm{MeV} \tag{1}$$

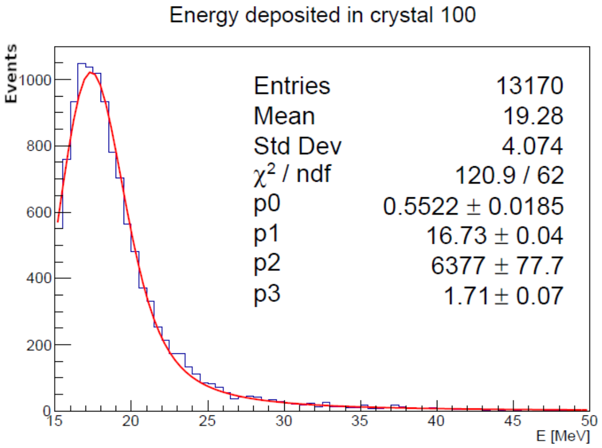

Figure 1: The deposited-energy distribution in one of the 1348 crystals of the Mu2e calorimeter. The fit is performed with a Landau function convoluted with a Gaussian. In this crystal, the extracted MPV value corresponds to 16.73 MeV.

since the energy deposit of a cosmic ray event is equivalent to 20 MeV electrons. The energy calibration reaches 0.2% accuracy with 2 simulated hours (Fig 2).

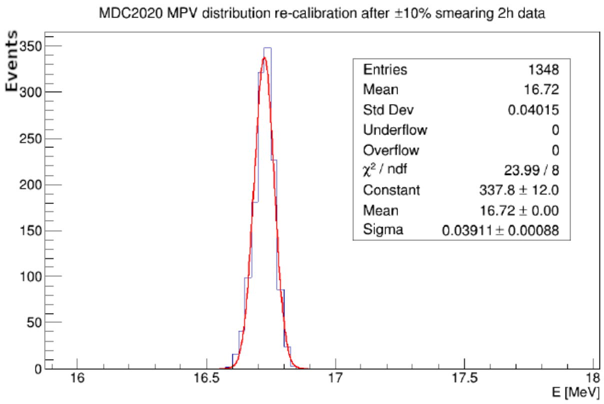

Figure 2: The MPV distribution after calibration shows a resolution σ/μ=0.2%.

3.2 Light Yield and Noise study with cosmic rays

The consistency of the SiPMs double readout is studied through the asymmetry variable:

$$\text{Asymm} = \frac{E_L - E_R}{E_L + E_R} \tag{2}$$

Where E_L and E_R indicate respectively the energy readout by the left SiPM and the right SiPM.
The sigma of the asymmetry variable can be parameterized using the Light Yield (LY) and the noise (SigNoise) value of the crystals:

$$\sigma(\text{Asymm}) = \sqrt{\frac{1}{2}\left(\left(\frac{1}{\text{LY}\cdot\text{E}}\right) + \left(\frac{\text{SigNoise}}{\text{E}}\right)^2\right)} \tag{3}$$

where E is the mean value of E_L and E_R.
For every 5 MeV slice, we extract the σ from the Gaussian fit to the asymmetry variable. As a function of the mean energy of the left and right readout (E), the extracted σ's distribution is fitted with Eq. 3 (Fig 3 - Left). The LY and the SigNoise values are extracted for every crystal.
As a confirming result, Fig. 3 - Right shows the asymmetry variable as a function of energy which is well confined in 5σ's described in Eq. 3 where we set a LY value of 30 Photoelectrons/MeV and a SigNoise value of 300 KeV.

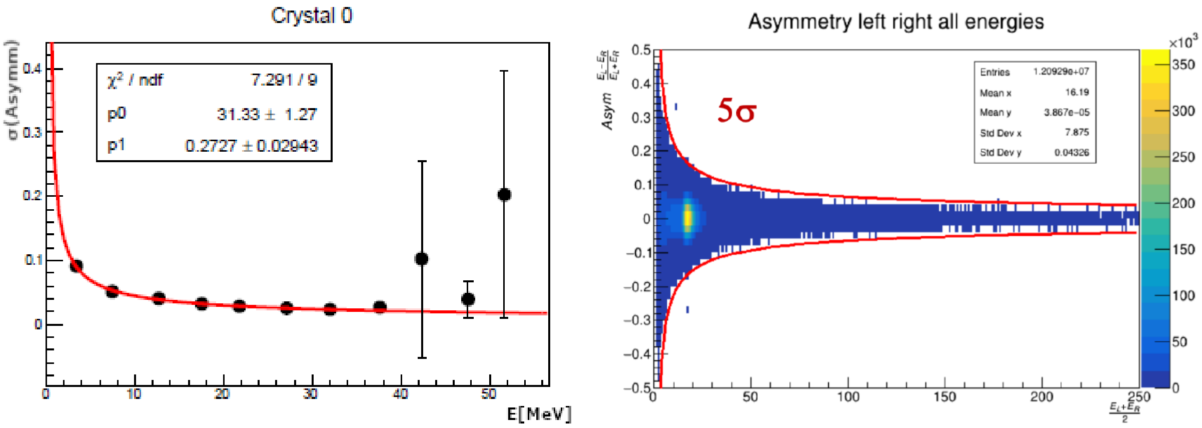

Figure 3: Left: σ(Asymm) distribution of the asymmetry variable for every 5 MeV slice fitted with Eq. 3. Right: The asymmetry variable as a function of the mean energy readout by the two SiPMs. The red lines identified 5σ's described by Eq. 3 for a LY value of 30 photoelectrons/MeV and a SigNoise value of 0.3 MeV.

3.3 Time Calibration

A time calibration is needed to remove the time offset and align the time response of crystals. An event selection is applied by requiring cosmic ray events belonging to one disk hitting at least four cells with a deposit of energy between 10 MeV and 30 MeV. The slope of the CR track is evaluated using a linear fit with the least-square method.
The time calibration method is organized in a two-step procedure: the first calibration step aligns the timing offsets at the ns level by using laser signals. In the second step, imposing that cosmic rays with minimum ionization travel at the speed of light, we correct the linear fit evaluation with its residual values iteratively. The process gets stable after few iterations and reaches a time resolution of 500 ps for a single readout unit (Fig. 4) and a time resolution of 350 ps at crystal level.

3.4 Time scale inter-calibration

The last step of calorimeter time calibration provides a global offset, which aligns crystal times with respect to the tracker. To perform this analysis, The CR track is reconstructed in the tracker, extrapolated to one of the two calorimeter disks, and associated to the nearest cluster. A subsequent selection for the tracker-calorimeter time calibration requires that the CR tracks cross at least a whole disk in the beam direction and is contained in the annulus defined by the radius R $\in$ [400, 600]mm. A further cut on the 2D distance between the cluster centroid and track extrapolation on the disk surface is applied along with a cut on the energy of the cluster. The timing of the calorimeter and tracker are calibrated independently.

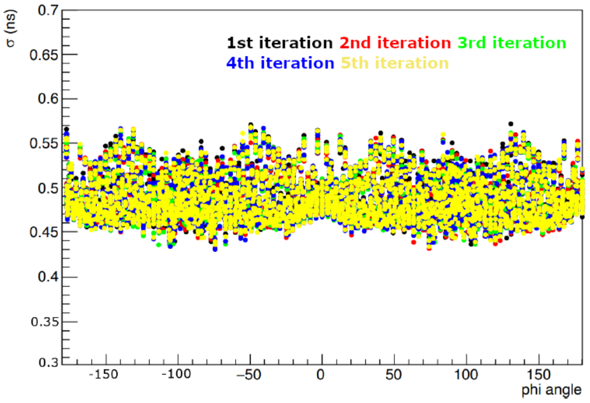

Figure 4: Time resolution of the time calibration method as a function of the azimuthal angle of the calorimeter for the iterative correction steps to the linear CR track fit.

Given the known relative positions of the two detectors and assuming that cosmic rays travel at the speed of light, the expected time-of-flight (TOF) can be computed and compared to the measured TOF.
To reach an agreement between the two TOF's, we parametrize their difference in terms of the polar angle of the CR track (Fig. 5) and we correct the calorimeter time response accordingly.
Fig 6 shows the tracker-calorimeter time difference before and after inter-calibration. The measured and

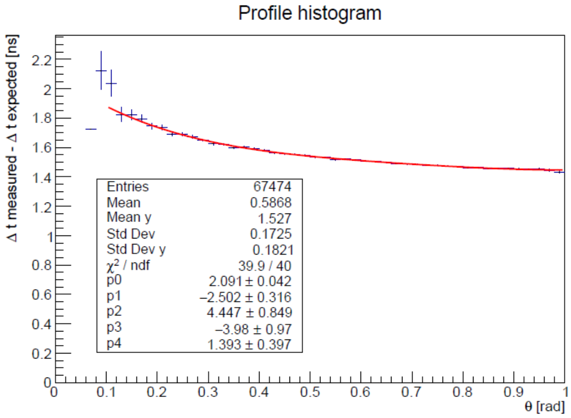

Figure 5: Parametrization of the difference between the TOF measured and the TOF expected in terms of the polar angle of the cosmic ray tracks

expected TOF's are aligned after applying the correction.

4 Acknowledgements

We are grateful for the vital contributions of the Fermilab staff and the technical staff of the participating institutions. This work was supported by the US Department of Energy; the Istituto Nazionale di Fisica Nucleare, Italy; the Science and Technology Facilities Council, UK; the Ministry of Education and Science, Russian Federation; the National Science Foundation, USA; the National Science Foundation, China; the Helmholtz Association, Germany; and the EU Horizon 2020 Research and Innovation Program under

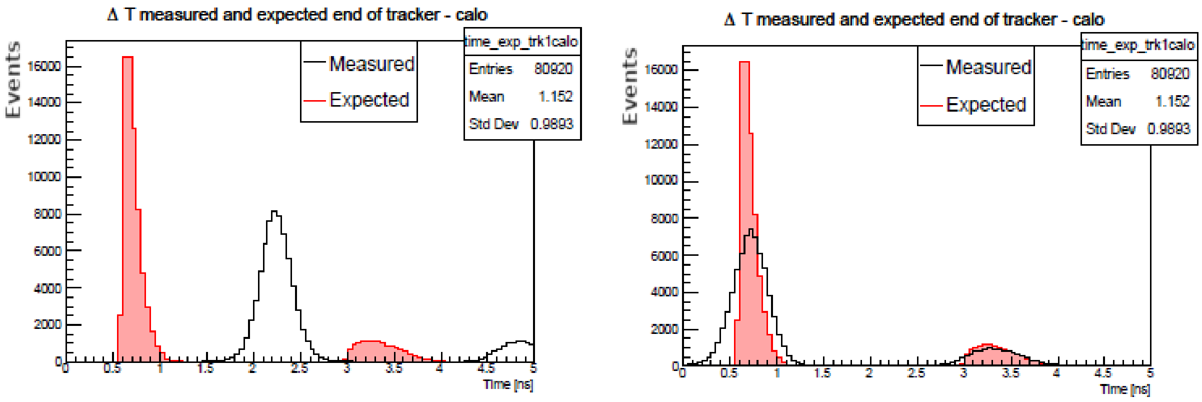

Figure 6: Left: TOF expected and TOF measured before the time scale inter-calibration show a relative offset of 1.5 ns. The two populations correspond to the TOFs with respect to the position of the two calorimeter disks. Right: TOF expected and TOF measured after the time scale inter-calibration.

the Marie Sklodowska-Curie Grant Agreement Nos. 734303, 822185, 858199, 101003460, and 101006726. This document was prepared by members of the Mu2e Collaboration using the resources of the Fermi National Accelerator Laboratory (Fermilab), a U.S. Department of Energy, Office of Science, HEP User Facility. Fermilab is managed by Fermi Research Alliance, LLC (FRA), acting under Contract No. DE-AC02-07CH11359.

References

1. L. Bartoszek *et al*, Mu2e Experiment, Mu2e technical design report, 2015, arXiv:1501.05241.
2. Mu2e Collaboration. Mu2e Run I Sensitivity Projections for the Neutrinoless $\mu^- \rightarrow e^-$ Conversion Search in Aluminum. Universe 2023, 9, 54. https://doi.org/10.3390/universe9010054.
3. S. Giovannella *et al*, The Mu2e crystal and SiPM calorimeter, Nuclear Instruments and Methods in Physics Research Section A: Accelerators, Spectrometers, Detectors and Associated Equipment, Volume 1069, December 2024, 169959.
4. N. Atanov *et al*, Design and status of the Mu2e crystal calorimeter, IEEE Trans.Nucl. Sci. 65 (2018) 2073–2080.
5. Chris Hagmann, David Lange, and DouglasWright. Cosmic-ray shower generator (cry) for monte carlo transport codes. In 2007 IEEE Nuclear Science Symposium Conference Record, volume 2, pages 1143–1146, 2007.
6. Tim Huege *et al*, Corsika an air shower simulation program. 2021.
7. Recent Developments in Geant4, J. Allison et al., Nucl. Instrum. Meth. A 835 (2016) 186-225
8. Geant4 Developments and Applications, J. Allison et al., IEEE Trans. Nucl. Sci. 53 (2006) 270-278
9. Geant4 - A Simulation Toolkit, S. Agostinelli et al., Nucl. Instrum. Meth. A 506 (2003) 250-303

Frascati Physics Series Vol. 76 (2024)
8TH YOUNG RESEARCHERS' WORKSHOP 'PHYSICS CHALLENGES IN THE LHC ERA'
May 13 and 16, 2024

MICROSCOPIC PARAMETRIZATION OF THE NEAR THRESHOLD OSCILLATIONS OF THE NUCLEON TIME-LIKE EFFECTIVE ELECTROMAGNETIC FORM FACTORS

Francesco Rosini
Dipartimento di Fisica e Geologia, INFN Sezione di Perugia, 06123 Perugia, Italy

Abstract

We present an analysis of the recent near threshold BESIII data for the nucleon time-like effective form factors. The damped oscillation emerging from the subtraction of the dipole formula is treated in non-perturbative-QCD, making use of the light cone distribution amplitudes expansion. Non-perturbative effects are accounted for by considering Q^2-dependent coefficients in such expansions, whose free parameters are determined by fitting to the proton and neutron data.

1 Introduction

The theoretical impossibility of describing the nucleon internal structure in terms of strongly interacting quarks and gluons, which are the fundamental fields of quantum chromodynamics, enhances the electromagnetic form factors (EMFFs) to the role of unique and privileged tools to unravel the dynamics underlying the electromagnetic interaction of nucleons. In specific reference frames, EMFFs represent the Fourier transforms of spatial charge and magnetic momentum densities.

Recently, the BESIII 1) experiment measured the time-like nucleon form factors (FFs) at center-of-mass energies between 2.0 GeV and 3.5 GeV 2, 3, 4, 5, 6). These data present an oscillating behavior 7, 8, 9, 10, 11, 12), which manifests itself as a periodic, exponentially dumped component over the typical dipolar carrier, usually identified as the only contribution. The nature of such an oscillating component is still unknown. If intrinsic to the baryons nature, the phenomenon would be encoded by the EMFFs of nucleons.

In order to investigate this eventuality we propose a parametrization for the EMFFs defined by considering the nucleons as triplets of collinear quarks lying at light-like distances in the light-front framework 13).

The matrix element of the "+" component of the hadronic current J^{μ}, which depends directly on the EMFFs, evaluated between the baryon and antibaryon particle states, can then be expanded using the Lorentz invariance of the three quark Fock state's matrix elements.

The resulting form depends on a set of functions of the four momentum squared fractions, called light cone distribution amplitudes (LCDAs), and a deep knowledge of their expression can provide further information about the form factors shape. Using the $\mathcal{L}_{\text{QCD}}$ conformal symmetry 14), the LCDAs are expanded on a polynomial basis, the most common choice being represented by the orthonormal Appell polynomials, defined on the triangle $T\left(x_1, x_3\right)=\left\{\left(x_1, x_3\right) \in \mathbb{R}: x_1>0, x_3>0, x_1+x_3<1\right\}$, where $x_i=k_i^{+}/P^{+}$ are the quark's light front momentum fractions along the $(^{+})$ direction and so the following relation holds: $\sum_{i=1}^{3} x_i=1$; here P^{+} and k_i^{+} being the baryon's momentum and the i-th parton's momentum along the $(^{+})$ direction respectively. The only unknown quantities now are the expansion coefficients, which have to be determined considering the phenomenology of the problem. Since we are considering a center of mass energy of the system between 2.0 GeV and 3.5 GeV, we cannot to use perturbative methods. Here we perform a truncated Laurent expansion of the non-perturbative coefficients over the negative powers of the four momentum squared, subsequently performing a fit over the recent BESIII experimental data to determine these coefficients. The final goal of this description is to find whether the oscillations of the EMFFs can be described by the model functions.

2 The microscopic model

One of the most effective ways to describe subnuclear processes is to work on a light front framework, expanding the involved particle states in a free particle state basis, commonly known as Fock states. For a baryon we have

$$|\text{baryon}\rangle=|0\rangle+|qqq\rangle+|qqqg\rangle+|qqqq\bar{q}\rangle+\ldots, \tag{1}$$

where the three-quark state can be expanded in a Lorentz series of its matrix element between the vacuum and the particle states. The expansion has already been performed in Ref. 15), e.g., for the proton has the form

$$\begin{aligned}
& \langle 0|\, \varepsilon^{ijk} u_\alpha^i\left(a_1 z\right) u_\beta^j\left(a_2 z\right) d_\gamma^k\left(a_3 z\right)|P\rangle \\
= \quad & \frac{1}{4}\Big[\mathcal{S}_1 M C_{\alpha\beta}\left(\gamma_5 N^{+}\right)_\gamma+\mathcal{V}_1\left(\not{p} C\right)_{\alpha\beta}\left(\gamma_5 N^{+}\right)_\gamma \\
& +\mathcal{P}_1 M\left(\gamma_5 C\right)_{\alpha\beta} N_\gamma^{+}+\mathcal{A}_1\left(\not{p}\gamma_5 C\right)_{\alpha\beta} N_\gamma^{+} \\
& +\mathcal{T}_1\left(i\sigma_{\perp p} C\right)_{\alpha\beta}\left(\gamma^{\perp}\gamma_5 N^{+}\right)_\gamma+\ldots\Big].
\end{aligned} \tag{2}$$

where z is a light-cone vector, ε^{ijk} is the Levi-Civita totally antisymmetric tensor, with $\varepsilon^{123}=1$, $q_\alpha^i\left(a_1 z\right)$ is a quark operator, where i is a colour index and α is a Dirac index. Moreover, C is the charge conjugation matrix, $\not{p}=p_\mu\gamma^\mu$, N^{+} is the plus component of the nucleon spinor, $\sigma^{\mu\nu}=\frac{i}{2}\left[\gamma^\mu, \gamma^\nu\right]$ and $|P\rangle$ is the nucleon state. The functions $\mathcal{S}_1$, $\mathcal{V}_1$, $\mathcal{P}_1$, $\mathcal{A}_1$, and $\mathcal{T}_1$ are called light cone distribution amplitudes. They are functions of the scalar product $P \cdot z$.

Considering now the Fourier transform of the three quark matrix element defined in Eq. (2) and imposing that the nucleon state isospin is 1/2, we can restrict the study of twist-3 LCDAs to a single function, which is chosen to be

$$\varphi_N(\mathbf{x})=V_1(\mathbf{x})-A_1(\mathbf{x}),$$

where $\mathbf{x}$ is the 3-vector (x_1, x_2, x_3). The new defined symbols V_1 and A_1 are the Fourier transforms of the functions $\mathcal{V}_1$ and $\mathcal{A}_1$, defined as

$$F\left(a_i p \cdot z\right) = \int [dx]\, F\left(x_i\right) e^{-ipz \sum_i a_i x_i} \,. \tag{3}$$

Taking advantage from the conformal symmetry of the Lagrangian density $\mathcal{L}_{\mathrm{QCD}}$, the twist-3 LCDA φ_N can be expanded over the orthonormalized Appell polynomials set $\left\{P_n\left(\mathbf{x}\right)\right\}_n$ as follows

$$\varphi_N\left(\mathbf{x}, Q^2\right) = 120 x_1 x_2 x_3 \sum_n B_n\left(Q^2\right) P_n\left(\mathbf{x}\right) \,. \tag{4}$$

The set of non-perturbative coefficients $\left\{B_n\right\}_n$ is unknown and contains all the information about the form factor for the leading twist.

Each coefficient B_n is linked to the φ_N LCDA's momenta. The first coefficient B_0 is fixed to one being linked to the normalization of φ_N.

As already stated, since we are considering the non perturbative aspect of the LCDAs, we can perform an expansion over the negative powers of the four-momentum squared,

$$B_n\left(Q^2\right) = \sum_{k=0}^{M_n} b_k^{(n)} Q^{-2k}, \tag{5}$$

where $Q^2 = -q^2$, $\left\{\{b_k^{(n)}\}_{k=0}^{M_n}\right\}_n$ is the set of coefficients and M_n is the maximum power of Q^{-2} in the expansion of the n^{th} parameter B_n.

3 Leading order contributing diagrams

Taking the leading order into account, the minimum number of contributing diagrams has been evaluated in Ref. 15), where fourteen diagrams have been considered. The Sachs form factors G_E and G_M which we are interested in are related to the Pauli and Dirac ones, F_1 and F_2 by the relations

$$\begin{aligned} G_E\left(Q^2\right) &= F_1\left(Q^2\right) - \tau F_2\left(Q^2\right) \,, \\ G_M\left(Q^2\right) &= F_1\left(Q^2\right) + F_2\left(Q^2\right) \,, \end{aligned} \tag{6}$$

where $\tau = Q^2/\left(4M_B^2\right)$. We performed our fit over the effective form factor data, which is linked to the Sachs form factors by the relation

$$G_{\text{eff}} = \sqrt{\frac{\left|G_E\right|^2 + 2\tau\left|G_M\right|^2}{1+2\tau}}. \tag{7}$$

Since we considered only twist-3 LCDAs, we assumed the coincidence of the Sachs form factors near the threshold, hence we can say that the modulus of the effective form factor coincides with the magnetic's one.

The light front EMFF can be written as the convolution of three probabilities, namely the probability of describing the baryon and antibaryon as a system of three collinear quarks, $\varphi_N\left(\mathbf{x}, Q^2\right)$, and the probability of finding a certain strong interaction, known as " hard scattering kernel" K_H. At the leading order, each of the fourteen contributing diagrams involving the exchange of two gluons, shown in 15, 16), corresponds to a hard scattering kernel $K_i\left(\mathbf{x}, \mathbf{y}\right)$. Here $\varphi_N\left(\mathbf{x}\right) = V_1\left(\mathbf{x}\right) - A_1\left(\mathbf{x}\right)$, and

$T(\mathbf{x}) = T_1(\mathbf{x})$ are the light cone distribution amplitudes involved in the calculation. In order to evaluate the form factor G_M, we used the Chernyak-Zhitnitsky 15) asymptotic formula

$$q^4 G_M\left(q^2\right) \to \frac{\left(4\pi\bar{\alpha}_s\right)^2}{54}\left|f_N\right|^2 \int[dx]\!\int[dy]\left(2\sum_{i=1}^{7} e_i K_i(\mathbf{x},\mathbf{y}) + \sum_{i=8}^{14} e_i K_i(\mathbf{x},\mathbf{y})\right), \tag{8}$$

where $[dx] = \delta\left(1-\sum_{i=1}^{3} x_i\right) dx_1 dx_2 dx_3$ and $\bar{\alpha}_s$ is the modified coupling constant. For the evaluation of the modified coupling constant $\bar{\alpha}_s^2$, we follow the procedure proposed by Chernyak and Zhitnitsky in Ref. 15). The value of $\bar{\alpha}_s^2$ is given by the product of the coupling constants for the two subprocesses, namely the two gluon exchanges which appear in the tree-level diagrams shown in Table **??**. The average virtuality $\bar{q}_1^2$ of the lightest gluon is $\bar{x}_3\bar{y}_3 q^2$, while the rest gluon has an averaged virtuality $\bar{q}_2^2 = \overline{(1-x_1)}\;\overline{(1-y_1)}q^2$. The typical values of a realistic nucleon wave function for the $\bar{x}_i$ are $\bar{x}_1 \simeq 2/3$, $\bar{x}_2 \simeq \bar{x}_3 \simeq 1/6$. Therefore $\bar{\alpha}_s^2\left(q^2\right) = \alpha_s\left(\frac{1}{36}q^2\right)\alpha_s\left(\frac{1}{9}q^2\right)$.

The integrals in Eq. (8) are (weakly) convergent and it is possible to solve them analytically, Non-perturbative-QCD effects are accounted for by considering the Q^2-dependence of the B_n defined in Eq. (5).Since we are limiting our discussion to the LCDA's second order momenta, we are only interested in the first six parameters, namely those of the set $\{B_n\}_{n=0}^{5}$.

For the truncated expansion, we propose $M_0 = 0$, $M_1 = M_2 = 1$, $M_3 = M_4 = M_5 = 2$, so that

$$\begin{aligned} B_0 &= 1\,, \\ B_n(Q^2) &= b_0^{(n)} + \frac{b_1^{(n)}}{Q^2}\,, \quad n = 1, 2\,, \\ B_m(Q^2) &= b_0^{(m)} + \frac{b_1^{(m)}}{Q^2} + \frac{b_2^{(m)}}{(Q^2)^2}\,, \quad m = 3, 4, 5\,. \end{aligned} \tag{9}$$

We obtain a closed expression of the form factor G_M depending only on the non-perturbative parameters for the proton and the neutron. Due to isospin symmetry, the proton and neutron parameters are the same and the magnetic form factors defined by Eq. (8) differ only by the values of the electric charges of the quarks which interact with the virtual photon. Due to this property, we performed a simultaneous fit to the recent BESIII data on proton and neutron cross sections to determine the coefficients.

4 Results and discussion

Figure 1 shows the results for the effective proton (left panel) and neutron (right panel) form factors in comparison with the experimental values measured by the BESIII experiment 2, 3, 4). The fit functions depend on 13 free parameters, which are the coefficients of the expressions of Eq. (9) and are reported with their corresponding errors in Table 1.
The normalized minimum χ^2 is

$$\frac{\chi^2}{n_{\mathrm{DoF}}} = \frac{79.93}{43} \simeq 1.79\,. \tag{10}$$

The fit has been obtained by using 48 data points of the proton cross section and 18 of the neutron one. The 1-σ error bands have been determined by considering both the errors of data, and the theoretical systematic error of the model, which has ben estimated by using expressions for the $B_n(Q^2)$ parameters with the additional power $\left(Q^{-2}\right)^{M_n+1}$.

Parameter	Coefficient	Value
B_1	$b_0^{(1)}$	-31 ± 1
	$b_1^{(1)}$	(-144 ± 11) GeV^2
B_2	$b_0^{(2)}$	-15.3 ± 0.1
	$b_1^{(2)}$	(36 ± 1) GeV^2
B_3	$b_0^{(3)}$	7.2 ± 0.3
	$b_1^{(3)}$	(-80 ± 3) GeV^2
	$b_2^{(3)}$	(251 ± 7) GeV^4
B_4	$b_0^{(4)}$	56 ± 2
	$b_1^{(4)}$	$(-2.95 \pm 0.03) \cdot 10^3$ GeV^2
	$b_2^{(4)}$	$(6.7 \pm 0.1) \cdot 10^3$ GeV^4
B_5	$b_0^{(5)}$	0.6 ± 0.7
	$b_1^{(5)}$	(80 ± 6) GeV^2
	$b_2^{(5)}$	(-135 ± 21) GeV^4

Table 1: Best values of fit parameters with errors.

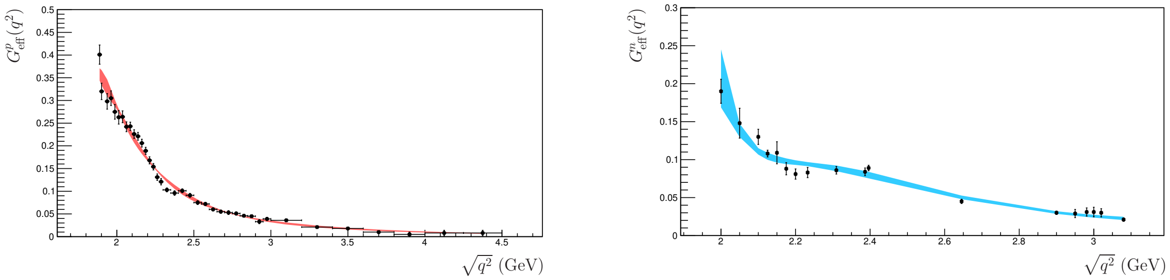

Figure 1: The bands represent the fit results for the proton (left panel) and neutron (right panel) effective form factor. The data are from the BESIII experiment (2, 3, 4).

Figure 2 shows the twist-3 nucleon distribution amplitude $\varphi_N(\mathbf{x})$ evaluated at $\sqrt{-Q^2} = 2.5$ GeV. The maximum value is reached at the light-cone momentum fractions

$$x_1 \simeq 0.49\,, \qquad x_2 \simeq 0.24\,, \qquad x_3 \simeq 0.27\,,$$

which agree with the assumption made in the Chernyak-Zhitnitsky formula (15) that the first quark has a momentum fraction about 50% larger than the other two, which equally divide the remaining momentum fraction.

Summarizing, a coherent model has been developed to reproduce the data on proton and neutron EMFFs, recently obtained by the BESIII collaboration. The model is based on a parametrization of the light-cone distribution amplitudes, and obeys conformal symmetry of the QCD Lagrangian.

Even though for the neutron effective form factor the model reproduces quite well the oscillatory behaviour, it seems to fail in the case of the proton. Indeed, the obtained behaviour of the effective proton form factor, the red band shown in the upper panel of Fig. 1, is compatible with the so-called regular background of Refs. (7, 8, 11). It can be interpreted as the contribution due to the short distance quark-level dynamics (17, 18), i.e., the $p\bar{p}$ final state is produced by the creation of quark-antiquark pairs within a small volume, with a linear dimension much smaller than the standard hadron size of about 1 fm.

Nevertheless, the model has the added value of proving that a unique parametrization in all the

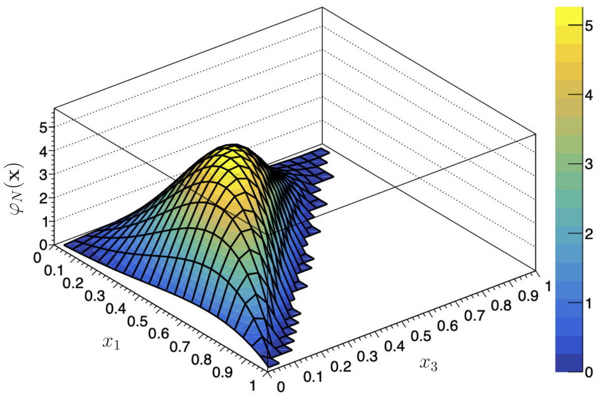

Figure 2: The nucleon distribution function $\varphi_N(\mathbf{x})$ obtained at $\sqrt{-Q^2} = 2.5$ GeV as a function of x_1 and x_3.

kinematical ranges where data are present is effective both for proton and neutron FFs. This is in contrast to previous works, where a common fit could only be achieved either in a restricted kinematical region, concluding in a change of the phase [3], or at the price of three different models applicable in different kinematical regions [5].

References

1. Institute of High Energy Physics Chinese Academy of Sciences, *BEPCII*. Available: `https://web.archive.org/web/20160316234203/http://www.ihep.ac.cn/english/E-Bepc/`. [Accessed: 16-Mar-2016].

2. M. Ablikim, M. N. Achasov, P. Adlarson, N. Amhed, Study of the process $e^+e^- \to p\overline{p}$ via initial state radiation at BESIII, *Phys. Rev. D*, 99(9):092002, May 2019.

3. M. Ablikim, M. N. Achasov, P. Adlarson, S. Ahmed, M. Albrecht, Oscillating features in the electromagnetic structure of the neutron, *Nature Physics*, 17(11):1200–1204, November 2021.

4. M. Ablikim, M. N. Achasov, P. Adlarson, N. Amhed, Measurement of Proton Electromagnetic Form Factors in $e^+e^- \to p\overline{p}$ in the Energy Region 2.00–3.08 GeV, *Phys. Rev. Lett.*, 124(4):042001, January 2020.

5. Qin-He Yang, Di Guo, Ling-Yun Dai, Johann Haidenbauer, Xian-Wei Kang, Ulf-G. Meißner, New insights into the oscillations of the nucleon electromagnetic form factors, *Science Bulletin*, 68(22):2729–2733, 2023.

6. M. Ablikim, M. N. Achasov, P. Adlarson, S. Ahmed, M. Albrecht, Measurement of proton electromagnetic form factors in the time-like region using initial state radiation at BESIII, *Physics Letters B*, 817:136328, 2021.

7. Andrea Bianconi and Egle Tomasi-Gustafsson, Periodic interference structures in the timelike proton form factor, *Phys. Rev. Lett.*, 114, 2015.

8. Andrea Bianconi and Egle Tomasi-Gustafsson, Phenomenological analysis of near threshold periodic modulations of the proton timelike form factor *Phys. Rev. C.*, 93, 2016.

9. Andrea Bianconi and Egle Tomasi-Gustafsson, Fourth dimension of the nucleon structure: Spacetime analysis of the timelike electromagnetic proton form factors *Phys. Rev. C.*, 95, 2017.

10. Andrea Bianconi and Egle Tomasi-Gustafsson, Soft rescattering in the timelike proton form factor within a spacetime scheme *Phys. Rev. C.*, 98, 2018.

11. Andrea Bianconi, Egle Tomasi-Gustafsson and Simone Pacetti, New fit of timelike proton electromagnetic form factors from e^+e^- colliders *Phys. Rev. C.*, 103, 2021.

12. Egle Tomasi-Gustafsson, Andrea Bianconi, and Simone Pacetti, Dynamical Properties of Baryons, *Symmetry*, 13(8):1480, 2021.

13. Stanley J. Brodsky and Hans-Christian Pauli and Stephen S. Pinsky, Quantum chromodynamics and other field theories on the light cone *Physics Reports*, 301, 1998.

14. V. M. Braun, S. É. Derkachov, G. P. Korchemsky, A. N. Manashov, Baryon distribution amplitudes in QCD, *Nuclear Physics B*, 553(1-2):355–426, July 1999.

15. V.L. Chernyak and I.R. Zhitnitsky, Nucleon wave function and nucleon form factors in QCD *Nuclear Physics B*, 246, 1984.

16. Francesco Rosini, Simone Pacetti, Olga Shekhovtsova, Egle Tomasi-Gustafsson, Microscopic parametrization of the near threshold oscillations of the nucleon time-like effective electromagnetic form factors, *The European Physical Journal A*, 60(7), July 2024.

17. V. A. Matveev, R. M. Muradian, and A. N. Tavkhelidze, Automodellism in the large - angle elastic scattering and structure of hadrons, *Lett. Nuovo Cim.*, 7:719–723, 1973.

18. Stanley J. Brodsky and Glennys R. Farrar, Scaling Laws at Large Transverse Momentum, *Phys. Rev. Lett.*, 31:1153–1156, 1973.

19. G. Peter Lepage and Stanley J. Brodsky, Exclusive processes in perturbative quantum chromodynamics *Phys. Rev. D.*, 22, 1980.

Frascati Physics Series Vol. 76 (2024)
8th young researchers' workshop 'Physics Challenges in the LHC Era'
May 13 and 16, 2024

NEW OPPORTUNITIES IN KAONIC ATOMS SPECTROSCOPY WITH NOVEL CZT DETECTOR

Francesco Artibani
Laboratori Nazionali di Frascati, INFN, Via E. Fermi 54, 00044 Frascati, Italy
Dipartimento di Matematica e Fisica, Università di Roma Tre, Via della Vasca Navale 84, 00146 Roma, Italy

Leonardo Abbene [2], Manuele Bettelli [4], Antonino Buttacavoli [2], Fabio Principato [2], Andrea Zappettini [4], Massimiliano Bazzi [1], Giacomo Borghi [5,6], Damir Bosnar [7], Mario Bragadireanu [8], Michael Cargnelli [3], Marco Carminati [5,6], Alberto Clozza [1], Francesco Clozza [1], Luca De Paolis [1], Raffaele Del Grande [1,9], Kamil Dulski [1], Laura Fabbietti [9], Carlo Fiorini [5,6], Ivica Friščić [7], Carlo Guaraldo [1†], Mihail Iliescu [1], Masahiko Iwasaki [10], Aleksander Khreptak [11], Simone Manti [1], Johann Marton [3], Pawel Moskal [11,12], Fabrizio Napolitano [1], Szymon Niedźwiecki [11,12], Hiroaki Ohnishi [13], Kristian Piscicchia [14,1], Yuta Sada [13], Francesco Sgaramella [1], Diana Laura Sirghi [1,8,14], Florin Sirghi [1,8], Magdalena Skurzok [11,12], Michal Silarski [11], Antonio Spallone [1], Kairo Toho [13], Lorenzo Toscano [5,6], Marlene Tüchler [3], Johann Zmeskal [3†], Catalina Curceanu [1], Alessandro Scordo [1]

Affiliations.
[1] Laboratori Nazionali di Frascati, INFN, Via E. Fermi 54, 00044 Frascati, Italy
[2] Dipartimento di Fisica e Chimica - Emilio Segrè, Università di Palermo, Viale Delle Scienze, Edificio 18, Palermo, 90128, Italy
[3] Stefan-Meyer-Institut für Subatomare Physik, Dominikanerbastei 16, Wien, 1010, Austria
[4] Istituto Materiali per l'Elettronica e il Magnetismo, Consiglio Nazionale delle Ricerche, Parco Area delle Scienze 37/A, Parma, 43124, Italy
[5] Dipartimento di Elettronica, Informazione e Bioingegneria, Via Giuseppe Ponzio 34, Milano, 20133, Italy
[6] INFN Sezione di Milano, Via Giovanni Celoria 16, Milano, 20133, Italy
[7] Department of Physics, Faculty of Science, University of Zagreb, Bijenička cesta 32, Zagreb, 10000, Croatia
[8] Horia Hulubei National Institute of Physics and Nuclear Engineering (IFIN-HH), No. 30, Reactorului Street, Magurele, Ilfov, 077125, Romania
[9] Physik Department E62, Technische Universität München, James-Franck-Straße 1, Garching, 85748, Germany
[10] Institute of Physical and Chemical Research, RIKEN, 2-1 Hirosawa, Wako, Saitama, 351-0198, Japan
[11] Faculty of Physics, Astronomy, and Applied Computer Science, Jagiellonian University, Łojasiewicza 11, Krakow, 30-348, Poland

[12] Centre for Theranostics, Jagiellonian University , Kopernika 40, Krakow, 31-501, Poland
[13] Research Center for Accelerator and Radioisotope Science (RARIS), Tohoku University, 1-2-1 Mikamine, Taihaku-kun, Sendai, 982-0826, Japan
[14] Centro Ricerche Enrico Fermi - Museo Storico della Fisica e Centro Studi e Ricerche "Enrico Fermi", Via Panisperna 89A, Roma, 00184, Italy
† Deceased.

Abstract

Kaonic atoms spectroscopy provides important observables for low-energy strong interactions in strange systems studies. In this paper, an overview of the SIDDHARTA-2 activities in kaonic atoms field is presented.
Particular attention is given to the development of the new cadmium-zinc-telluride detection systems to measure intermediate-mass kaonic atoms. The characteristics of the detector, the results of the two first test measurements in DAΦNE, and some of the physics goals are presented.

1 Introduction

The study of kaonic atoms is crucial to investigate the low-energy regime of the strong interactions with strangeness [1, 2, 3]. Kaonic atoms are systems in which a low energy kaon is trapped by the electromagnetic field of an atoms's nucleus. The kaon, after replacing one of the electrons in the outermost cell, is bounded to the nucleus and forms a kaonic atom. The kaonic atom is created in an highly excited state, and the kaon starts a cascade de-excitation process that, in its last part, is radiative. In the last levels, the kaon and the nucleus are close enough to experience strong interactions together with the electromagnetic one. A schematic image representing these three processes is reported in Figure 1.
The presence of the additional strong interaction, from a spectroscopic point of view, reflects in a shift ϵ on the energy of the level calculated with Quantum-ElectroDynamics (QED) only, and in a widening Γ of the level, caused by the limited lifetime of the level before the kaon is absorbed by the nucleus [4]. These observables are linked to the scattering lengths, that at vanishing relative energy is direcly related to the cross section, relevant for the theories studying the strong interactions at low energy.
The SIDDHARTA-2 collaboration performs high precision kaonic atoms studies. After the important measure of the shift and the width of kaonic hydrogen, done by the SIDDHARTA experiment at DAΦNE [5], the main goal of SIDDHARTA-2 is to measure the shift and width of the kaonic deuterium. Thanks to these two measurements together, it will be possible to extract the isospin-dependent antikaon-nucleon scattering lenghts.
The kaonic atoms data are also important to improve and test new models on the kaon-nucleon (K-N) and kaon-multinucleon (K-multiN) interactions at threshold. Indeed, they provide unique observables at (even below) threshold for the strong interaction, and these observables are direct input to the theory. For this reason, the collaboration is aiming to measure kaonic atoms' shift and width for different mass ranges. Focusing on the light and intermediate mass range, the existing dataset of kaonic atoms measurement [12] reports the results of experiments done in the '70s-'80s, often incompatible between each other.
The SIDDHARTA-2 collaboration is also planning to measure intermediate mass kaonic atoms, exploiting a new cadmium-zinc-telluride (CZT, CdZnTe) detector. In test measurements, this promising semiconductor showed good feature in terms of resolution and efficiency in a wide energy range (from keV to MeV), and, differently from other X-ray detectors, it works at room temperature, making it ideal to build reliable and compact setups [6, 7, 8]. It is the first application of such a technology in a collider experiment, and important tests about the feasibility of a kaonic atoms experiments in a collider paved the way for a new generation of CZT detectors with applications on collider experiments and on particle

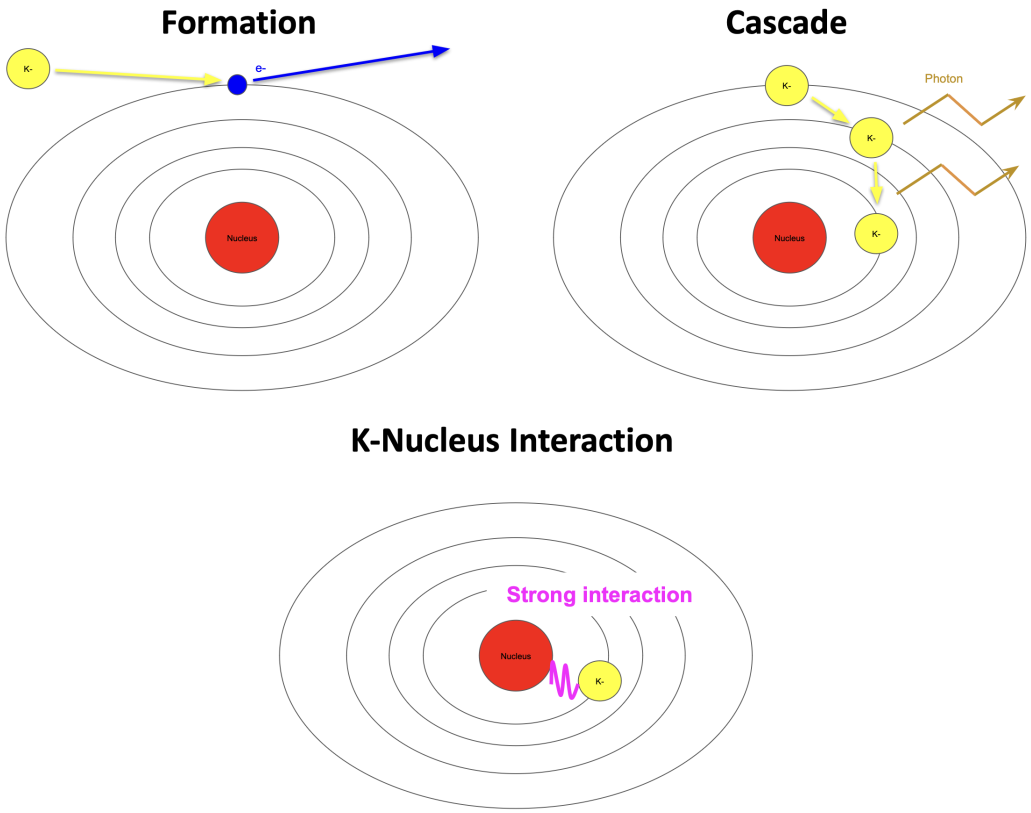

Figure 1: *Schematic representation of the kaonic atom's processes: Formation, Cascade and Strong Interaction. The kaon is represented in yellow, the nucleus in red, the electrons in green, the X-rays coming from the cascade process in orange, and the strong interaction in the last level in purple.*

and nuclear physics. In section 2, the detection system and the first outcomes of the tests in DAΦNE are summarized.

2 The Cadmium-Zinc-Telluride Detector

CZT is a promising material in the field of radiation detectors for X-ray spectroscopy. This compound semiconductor, a ternary compound of cadmium, zinc and tellurium, attracted increasing interest as X-ray and γ-ray detector in the last decades, because of the good performance in terms of resolution, linearity and fast response at room temperature. This unique features are appealing for the possibility to produce incredibly versatile, reliable and compact detectors for the X-ray and γ-ray, without the need of a cooling system.

Following important applications in various research fields, the SIDDHARTA-2 collaboration built a new CZT detector system foreseeing one of the first application of this semiconductor in a collider 9, 10, 11). The system, in its last configuration, is composed of two modules of eight $13\,\mathrm{mm} \times 15\,\mathrm{mm} \times 5\,\mathrm{mm}$ quasi-hemispherical CZT detectors provided by REDLEN in a thin aluminum box. The detectors present a custom electronics developed within the collaboration to increase the performances: a 3D-printed detector holder with electrical connection to cathode and anode electrodes, Charge Sensitive Preamplifiers (CSPs) and a Digital Pulse Processing (DPP) system, described accurately in [8, 10]. A view of a module of the detector is reported in Figure 2.

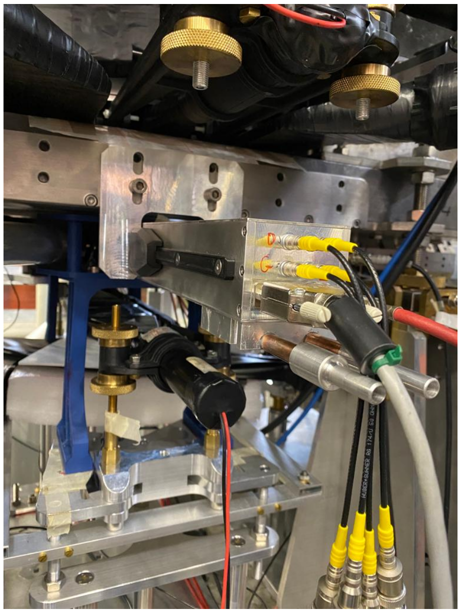

Figure 2: *Photo of the aluminum box containing the four CZT detectors installed near the DAΦNE collider's beam pipe, during a test measurement.*

The collaboration performed two important tests of the detector. These tests represent the first spectroscopic measurements using a CZT detector in a collider environment. The resolution, the linearity and the fast response of the detector were tested, obtaining good results despite the high background of the DAΦNE collider. In Figure 3, a spectrum collected with an Americium (^{2}41Am) source and beam on in the first test in DAΦNE [10] with the CZT detector is reported. Two peaks of the ^{2}41Am source were visible, together with escape peaks. The resolutions resulted to be 6% at 60 keV and of 2.2% at 511 keV. The test confirmed that a CZT detectors can be used in colliders despite the high background. The results on linearity and fast timing are reported in [9].

3 The Physics Case: Intermediate-mass Kaonic Atoms

The CZT detector will be used to perform intermediate-mass kaonic atoms measurements at the DAΦNE collider or elsewhere.

In particular, some kaonic atoms present interesting physics cases and new measurements are requested by the theoretical community:

- **Kaonic Oxygen and Kaonic Carbon.** These two kaonic atoms deserve a particular attention. Indeed, these two measurements exhibit a large uncertainty comparing to the others following the table in [12]. This causes problems in the phenomenological models because they are the boundary elements between light and heavy ones, and more precise results have important implications, for example, on the description of the nuclear density distribution [13].

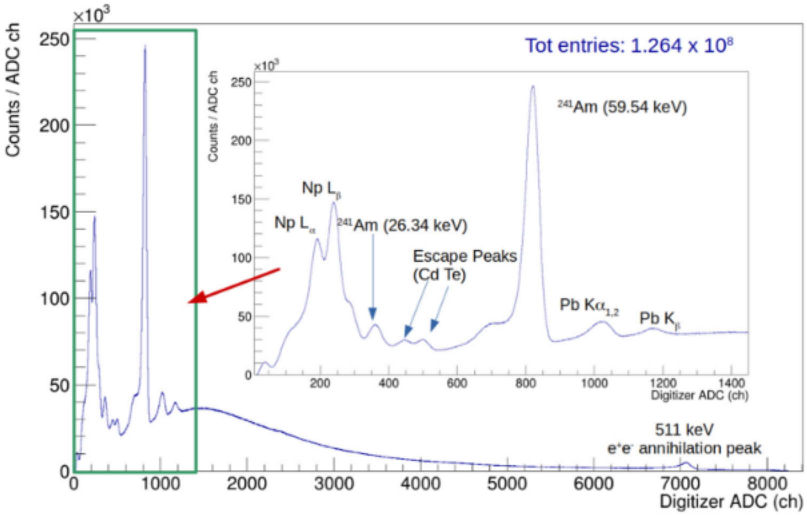

Figure 3: *Spectrum collected with the CZT detector and the DAΦNE beam on during the test described in* 10)*. The annihilation peak at 511 keV and the two peaks coming from the lead shielding scintillation are visible together with the Americium source spectrum. In the box a zoom on the source's peaks around 26 keV and 60 keV is reported.*

- **Kaonic Aluminum, Kaonic Sulfur, Kaonic Copper.** These atoms exhibit two (three in the case of sulfur) incompatible measurements, that reflect in huge uncertainties in the models on K-multiN interactions in that range 14). A new, precise, measurement, would finally solve this problem.
- **Kaonic Lead.** The kaonic lead, beside the important role in the low-energy strong interactions with strangeness, has also applications in the kaon mass calculation. The kaon mass is one of the open problem in particle physics 15). A new HPGe detector was arranged by the SIDDHARTA-2 collaboration with the aim of measuring kaonic lead transitions and the kaon mass. The experiment is already providing first results 16), and parallel kaonic lead measurement with CZT detector would help to confirm these results and extend the range of the transitions measured by the collaboration.

In Table 1, a list of kaonic atoms transitions, calculated with relativistic effects based on the calculations in 17), which can be measured by CZT, is reported.

4 Conclusions

New measurements of kaonic atoms are needed by the theoretical community working in the studies of strong interaction at low energies. The SIDDHARTA-2 collaboration, beside the groundbreaking measurement of the kaonic deuterium, which is the main goal of the experiment, is also planning new kaonic atoms measurement from the whole periodic table. To measure intermediate mass kaonic atoms, the collaboration developed an innovative CZT detector system, tested successfully for the first time in the DAΦNE collider.

5 Acknowledgements

We thank H. Schneider, L. Stohwasser, and D. Pristauz-Telsnigg from Stefan Meyer-Institut for their fundamental contribution in designing and building the SIDDHARTA-2 setup. We thank as well the INFN, INFN-LNF and the DAΦNE staff, in particular to Dr. Catia Milardi, for the excellent working conditions and permanent support. Catalina Curceanu acknowledge University of Adelaide, where part of this work was done (under the George Southgate fellowship, 2024). Part of this work was supported by the Austrian Science Fund (FWF): [P24756-N20 and P33037-N]; the EXOTICA project of the Ministero degli Affari Esteri e della Cooperazione Internazionale, PO22MO03; the Croatian Science Foundation under the project IP-2018–01-8570; the EU STRONG-2020 project (Grant Agreement No. 824093); the EU Horizon 2020 project under the MSCA (Grant Agreement 754496); the Japan Society for the Promotion of Science JSPS KAKENHI Grant No. JP18H05402; the SciMat and qLife Priority Research Areas budget under the program Excellence Initiative - Research University at the Jagiellonian University, and the Polish National Agency for Academic Exchange (Grant No. PPN/BIT/2021/1/00037); the EU Horizon 2020 research and innovation programme under project OPSVIO (Grant Agreement No. 101038099). This work was also supported by the Italian Ministry for University and Research (MUR), under PRIN 2022 PNRR project CUP: B53D23024100001.

References

1. C. Curceanu *et al*, Rev. Mod. Phys. **91**, 025006 (2019).
2. F. Artibani, F. Clozza *et al*, Acta Phys. Pol. B **55**, 5-A2 (2024).
3. C. Curceanu *et al*, Front. Phys. **11** (2023).
4. A. Cieplý and M. Mai and Ulf-G. Meißner and J. Smejkal, Nucl. Phys. A **954**, 17-40 (2016).
5. M. Bazzi *et al*, Phys. Lett. B **704**, 113-117 (2011).
6. L. Abbene and G. Gerardi, J. Synchrotron Radiat. **22**, 1190-1201 (2015).
7. L. Abbene *et al*, J. Synchrotron Radiat. **24**, 429-438 (2017).
8. L. Abbene *et al*, J. Synchrotron Radiat. **27**, 319-328 (2020).
9. A. Scordo *et al*, NIM A **1060**, 169060 (2024).
10. L. Abbene *et al*, EPJ ST **232**, 1487-1492 (2023).
11. L. Abbene *et al.* Sensors. **23(17)**, 7328, (2023)
12. E. Friedman and A. Gal and C. J. Batty, Nucl. Phys. A **579**, 518-538 (2024).
13. H. De Vries and C. W. De Jager and C. De Vries, At. Data Nucl. Data Tables **36**, 495-536 (2024).
14. C.J. Batty and E. Friedmann and A. Gal, Phys. Rep. **287**, 385-445 (2024).
15. S. Navas *et al.* (Particle Data Group), Phys. Rev. D **110**, 030001 (2024)
16. D. Bosnar *et al*, Kaonic lead feasibility measurement at DAΦNE to solve the charged kaon mass discrepancy, eprint (2024).
17. O. Gorceix *et al* J. Phys. B: Atom. Mol. Phys. **20** 639 (1987)

Table 1: *Table reporting kaonic atoms reference energies in keV.*

Kaonic Aluminum				
Transition	Non - relativistic Transition Energy	Relativistic Effects	**Transition Energy**	Measured Shift
3-2	302.293	1.407	**303.700**	Never Measured
4-3	105.803	0.767	**106.570**	- 0.130 ± 0.050 - 0.076 ± 0.014
5-4	48.9715	0.2585	**49.230**	//
6-5	26.6018	0.1052	**26.707**	//

Kaonic Sulfur				
Transition	Non - relativistic Transition Energy	Relativistic Effects	**Transition Energy**	Measured Shift
4-3	160.753	1.322	**162.075**	- 0.550 ± 0.06 - 0.43 ± 0.12 - 0.462 ± 0.054
5-3	235.158	1.775	**236.933**	Never Measured
5-4	74.4055	0.4525	**74.858**	//
6-5	40.4178	0.1872	**40.605**	//

Kaonic Copper				
Transition	Non - relativistic Transition Energy	Relativistic Effects	**Transition Energy**	Measured Shift
5-4	246.411	2.274	**248.685**	- 0.240 ± 0.022 - 0.377 ± 0.048
6-4	380.264	3.235	**383.499**	Never Measured
6-5	133.853	0.961	**134.814**	//
7-6	80.709	0.464	**81.173**	//
8-7	52.3833	0.2457	**52.629**	//

Kaonic Lead				
Transition	Non - relativistic Transition Energy	Relativistic Effects	**Transition Energy**	Measured Shift
8-7	421.271	4.903	**426.174**	- 0.020 ± 0.012
9-8	288.822	2.800	**291.622**	//
10-9	206.593	1.703	**208.296**	//
11-10	152.855	1.087	**153.942**	//
12-11	116.259	0.720	**116.979**	//
13-12	90.4769	0.4921	**90.969**	//
14-13	71.791	0.344	**72.135**	//
15-14	57.917	0.247	**58.164**	//

Frascati Physics Series Vol. 76 (2024)
8TH YOUNG RESEARCHERS' WORKSHOP 'PHYSICS CHALLENGES IN THE LHC ERA'
May 13 and 16, 2024

A NEW MEASUREMENT OF THE KAONIC HELIUM L-LINES WITH SIDDHARTA-2 AT DAΦNE

Francesco Clozza
Laboratori Nazionali di Frascati INFN, Frascati, Italy

L. Abbene [2], F. Artibani [1,14], M. Bazzi [1], G. Borghi [4,5], D. Bosnar [6], M. Bragadireanu [7], A. Buttacavoli [2], M. Cargnelli [3], M. Carminati [4,5], A. Clozza [1], G. Deda [4,5], L. De Paolis [1], R. Del Grande [1,8], K. Dulski [1,11], C. Fiorini [4,5], I. Friščić [6], C. Guaraldo [1†], M. Iliescu [1], M. Iwasaki [9], A. Khreptak [10], S. Manti [1], J. Marton [3], P. Moskal [10,11], F. Napolitano [1], S. Niedźwiecki [10,11], H. Ohnishi [12], K. Piscicchia [13,1], F. Principato [2], A. Scordo [1], F. Sgaramella [1], M. Silarski [10,11], D.Sirghi [1,7,13], F. Sirghi [1,7], M. Skurzok [10,11], A. Spallone [1], K. Toho [12], M. Tüchler [3], J. Zmeskal [3†] and Catalina Curceanu [1]

Affiliations.
[1] Laboratori Nazionali di Frascati, INFN, Via E. Fermi 54, 00044 Frascati, Italy
[2] Dipartimento di Fisica e Chimica - Emilio Segrè, Università di Palermo, Viale Delle Scienze, Edificio 18, Palermo, 90128, Italy
[3] Stefan-Meyer-Institut für Subatomare Physik, Dominikanerbastei 16, Wien, 1010, Austria
[4] Dipartimento di Elettronica, Informazione e Bioingegneria, Via Giuseppe Ponzio 34, Milano, 20133, Italy
[5] INFN Sezione di Milano, Politecnico di Milano, Via Giuseppe Ponzio 34, Milano, 20133, Italy
[6] Department of Physics, Faculty of Science, University of Zagreb, Bijenička cesta 32, Zagreb, 10000, Croatia
[7] Horia Hulubei National Institute of Physics and Nuclear Engineering (IFIN-HH), No. 30, Reactorului Street, Magurele, Ilfov, 077125, Romania
[8] Physik Department E62, Technische Universität München, James-Franck-Straße 1, Garching, 85748, Germany
[9] Institute of Physical and Chemical Research, RIKEN, 2-1 Hirosawa, Wako, Saitama, 351-0198, Japan
[10] Faculty of Physics, Astronomy, and Applied Computer Science, Jagiellonian University, Łojasiewicza 11, Krakow, 30-348, Poland
[11] Centre for Theranostics, Jagiellonian University , Kopernika 40, Krakow, 31-501, Poland
[12] Research Center for Accelerator and Radioisotope Science (RARIS), Tohoku University, 1-2-1 Mikamine,Taihaku-ku, Sendai, 982-0826, Japan
[13] Centro Ricerche Enrico Fermi - Museo Storico della Fisica e Centro Studi e Ricerche "Enrico Fermi", Via Panisperna 89A, Roma, 00184, Italy
[14] Università degli studi di Roma Tre, Dipartimento di Fisica, Roma, Italy

† Deceased.

Abstract

The ultimate goal of the SIDDHARTA-2 experiment at the LNF-INFN is to perform the first ever measurement, via X-ray spectroscopy, of the width and shift induced by the strong interaction to the $2p \rightarrow 1s$ energy transition of kaonic deuterium. Such a measurement has not been performed yet due to its high difficulty level; in fact, this transition exhibits an extremely low X-ray yield. For this reason, before starting the kaonic deuterium data taking campaign, an accurate and thorough characterisation of the experimental apparatus is of primary importance to gauge its performance. To finalize such a task the best candidate is Helium-4, since the $3d \rightarrow 2p$ transition of kaonic helium-4 exhibits a much higher yield of X-rays. This work reports the results of the characterisation of the SIDDHARTA-2 apparatus in preparation for the kaonic deuterium measurement. This is done by measuring the shift and width for the $3d \rightarrow 2p$ transition of kaonic helium-4. The measured values are $\varepsilon_{2p} = 2.0 \pm 1.2(\mathrm{stat}) \pm 1.5(\mathrm{syst})\,\mathrm{eV}$ and $\Gamma_{2p} = 1.9 \pm 5.7(\mathrm{stat}) \pm 0.7(\mathrm{syst})\,\mathrm{eV}$. The result shows a net enhancement of the performance of the apparatus when compared to the previous measurement done by the SIDDHARTA experiment $\varepsilon_{2p} = 0 \pm 6(\mathrm{stat}) \pm 2(\mathrm{syst})\,\mathrm{eV}$, thus providing strong evidence of the potential to perform the kaonic deuterium measurement.

1 Scientific case

An exotic atom 1) is an atomic system in which a negatively charged particle, either a lepton or an hadron, replaces an electron when captured into an atomic orbit by its electromagnetic interaction with the nucleus. The values of the energy levels of the electromagnetic interaction between the negatively charged particle and the nucleus are calculated with great accuracy by Quantum Electrodynamics (QED). Therefore, small deviations in the energy of the atomic levels with respect to the solely QED-calculated ones, contain additional information on the interaction occurring between the captured particle and the nucleus. In this framework, hadronic atoms play a crucial role: when present, the strong interaction manifests itself in the lowest energy levels before nuclear absorption occurs. Transitions to these low-lying energy levels are concurrent with the emission of radiation, namely X-rays. These can be detected via X-ray spectroscopy and, given that the relative energy between the captured hadron and the nucleus is the binding energy of the system, of the order of some keV for light kaonic atoms, this allows us to perform a direct measurement of the strong interaction at low energy. Among hadronic atoms, kaonic atoms offer a unique opportunity to directly probe the strong interaction of particles with strangeness in the non-perturbative regime of Quantum Chromodynamics (QCD). From the measurement of the shift and the width induced by the strong interaction on the $1s$ level of the kaonic hydrogen and kaonic deuterium, the isospin-dependent antikaon-nucleon (anti$K$-N) scattering lengths can be obtained 2, 3). Hence, the outcome of the kaonic deuterium measurement will contribute to the understanding of the anti$K$–N interaction in the non-perturbative regime of QCD and will be a test field for several theoretical models 4, 5, 6, 7, 8, 9, 10). The SIDDHARTA experiment 11) successfully measured the kaonic hydrogen in 2009, while the kaonic deuterium measurement is still to be performed. This is a very challenging measurement due to the extremely low yield of X-rays of the transitions to the fundamental level, which is expected to be about one order of magnitude lower than that of kaonic hydrogen. To perform such a measurement it is therefore of key importance that the experimental apparatus is thoroughly characterized using a high X-ray yield gaseous target. Helium-4 is an excellent candidate to fulfill this purpose since the $3d \rightarrow 2p$ transition has a yield roughly 100 times larger than that of kaonic deuterium. This kind of measurement has already been performed by the SIDDHARTA experiment 12) in 2009, hence its result in terms of the shift of the $2p$ level can be compared to the new one obtained with the SIDDHARTA-2 experimental apparatus. The new measurement of the kaonic helium L-lines, presented in this work, proves the excellent performance of the SIDDHARTA-2 apparatus, which qualifies as the state-of-the-art instrument for the challenging measurement of kaonic deuterium.

2 The SIDDHARTA-2 Setup on DAΦNE

DAΦNE is an electron-positron collider at the INFN-LNF working with center of mass energy centered on the mass of the ϕ meson (1.02 GeV). The ϕ mesons are produced at threshold and decay into K^+/K^- pairs with a branching ratio of **48.9%**. The produced charged kaons have low energies, with a momentum of only 127 MeV/c, hence are easily stopped inside a gaseous target. The SIDDHARTA-2 experiment is installed above the interaction point (IP) of the DAΦNE collider. The setup is shown in Figure 1. Above and below the IP, a pair of plastic scintillators, read by two Photo-Multiplier Tubes (PMTs) each, act as a Kaon Trigger (KT) exploiting the specific time of flight (TOF) of the slow kaons. The purpose of the KT is to select the kaons which are emitted back-to-back from the ϕ decay in the IP and are directed towards the target, and is used to suppress the background asynchronous with the collisions. The vacuum chamber is located above the IP and contains the cryogenic target cell. High purity titanium–copper strips are placed on dedicated holders on the target cell walls for calibration purposes. The charged kaons travel through the vacuum chamber window, then enter the target cell and interact with the gas, forming kaonic atoms and subsequently emitting X-rays. Surrounding the target, silicon drift detectors (SDDs) 13, 14, 15, 16, 17, 18) are used to detect the X-rays coming from the de-excitation of the kaonic atoms. To suppress the background component synchronous with the collisions, two different veto systems are placed outside the vacuum chamber, the Veto-1 system 19), and around the SDDs, the Veto-2 system 20, 21). A system made of two X-ray tubes is employed for the in situ calibration of the SDDs. More information regarding the experimental setup and its components can be found in 22).

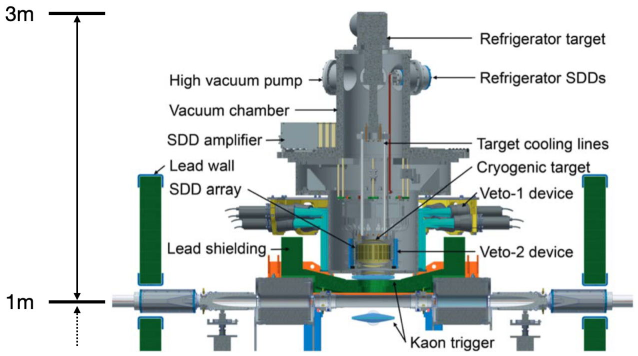

Figure 1: *Schematic view of the SIDDHARTA-2 experimental setup. The whole system is installed at the* e^+e^- *IP in DAΦNE.*

3 SDDs calibration and data selection

The characterization of the experimental setup was carried out using a helium-4 gaseous target at **1.5%** of liquid helium-4 density.

3.1 SDDs Calibration in DA$\mathbf{\Phi}$NE

The energy calibration of the detectors inside the DA$\mathbf{\Phi}$NE hall is one of the most crucial aspects of the data analysis procedure. Given the slight differences between the SDDs, individual calibrations are mandatory. The calibration was carried out using two X-ray tubes and a ^{55}Fe source. The X-ray tubes are used to induce the characteristic fluorescence emission lines of the high-purity titanium and copper strips placed on the target cell walls; the ^{55}Fe decays via electron capture to an excited state of ^{55}Mn, which then emits an X-ray during the de-excitation process. Hence, we identified in the spectrum the peaks associated with the TiK$_{\alpha}$, the CuK$_{\alpha}$, and the MnK$_{\alpha}$ X-ray emissions. To describe each peak, a Gaussian function summed up to a tail component, to account for the low energy contributions due to incomplete charge collection, is used 23). Once the individual calibrations are done with, the calibrated spectra of each detector are summed up together into a final spectrum, shown in Figure 2, which is then analyzed. By analyzing the difference between the measured energy value and the nominal one of the TiK$_{\alpha}$, CuK$_{\alpha}$, and MnK$_{\alpha}$ peaks, shown in Figure 2, we obtained a gauge of the calibration accuracy, which is of the order of 1.5 eV at ∼6 keV. From the fit can also be extracted a good estimate of the energy resolution of the apparatus at ∼6 keV from the FWHM of the MnK$_{\alpha}$ peak, resulting in a value of (170.97 ± 0.69) eV FWHM 24).

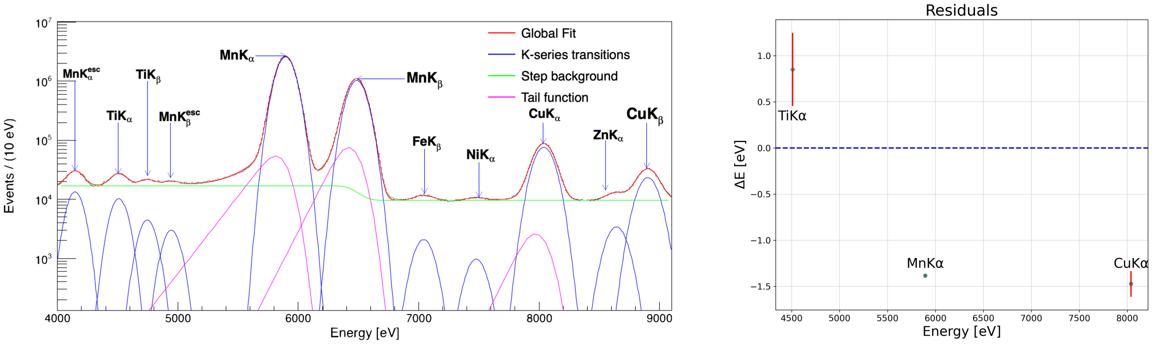

Figure 2: *a) Final calibration spectrum given by the sum of all the calibrated spectra of each SDD; b) Distribution of the residuals of the energy of the TiK$_{\alpha}$, MnK$_{\alpha}$, and CuK$_{\alpha}$ lines from their nominal energy. Adapted from* 24).

3.2 Data selection

To perform the measurement of kaonic helium-4, a total integrated luminosity of ∼31 pb^{-1} was collected. The energy spectrum initially presents a high continuous background component hindering the direct observation of the kaonic helium lines; therefore, background rejection cuts were applied to the experimental data. The asynchronous component of the background can be heavily suppressed by using the KT. A 5 µs time window in coincidence with the KT signal is set, thus rejecting a major portion of the background. Aside from this background source, MIPs, generated by the beam–beam and beam–gas interactions resulting in particle losses, can produce a fake signal in the trigger. To reject such triggers, the TOF signature was used by measuring the time difference between the trigger signal and the DA$\mathbf{\Phi}$NE radio-frequency (RF). From the mean time of the PMTs signal of the upper scintillator and that of the lower one, the timing information of the trigger is extracted and referenced to the RF. Figure 3 shows the time distributions measured by the two KT scintillators and the cut used to reject the MIPs-induced triggers. Furthermore, the time difference between the X-ray detection and the KT signal (Figure 3), was evaluated. Events inside the red lines are related to hits on the SDDs in coincidence with the KT signals, while the flat distribution on the two sides comes from uncorrelated events which therefore are rejected.

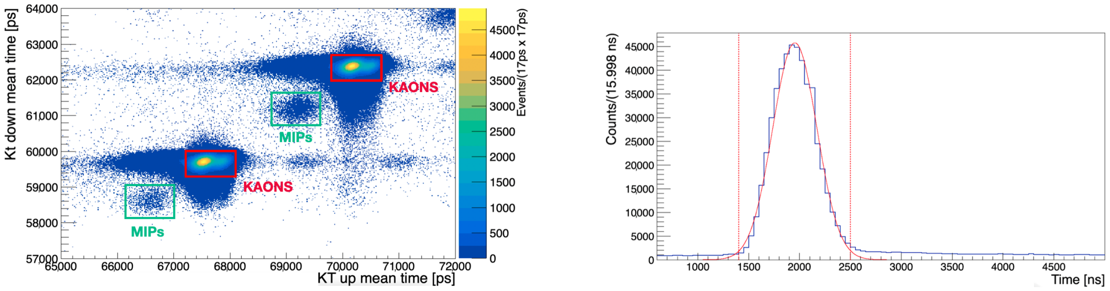

Figure 3: *a) Two-dimensional scatter plot of the mean time distributions measured by the two KT scintillators; b) Distribution of the time differences between the KT signal and the detection of the X-ray with the temporal cut to reject the background. Adapted from* [24].

4 The Kaonic Helium-4 Energy Shift and Width

The final spectrum, with the fit to it, is shown in Figure 4; after the data selection, the kaonic helium-4 L-series lines are clearly visible and were fitted to extract their energies. To account for the intrinsic line width ($\boldsymbol{\Gamma}$) induced by the strong interaction, the kaonic helium peaks were fitted with a Voigt function, *i.e.* a convolution of a Lorentzian function with a Gaussian.

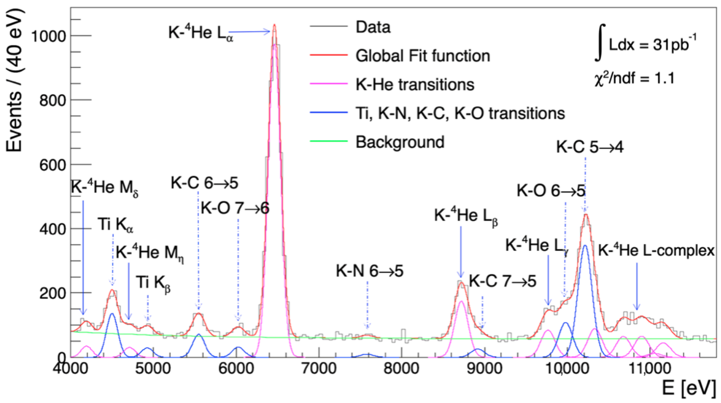

Figure 4: *X-ray energy spectrum and fit to the data after the data selection. The lines of kaonic helium transitions are fitted with a Voigt function, and the other lines are fitted with a Gaussian. Adapted from* [24].

The measured value of the shift of the $\boldsymbol{2p}$ level and its measured intrinsic width induced by the strong interaction are $\boldsymbol{\varepsilon_{2p}} = \mathbf{2.0 \pm 1.2}(\text{stat}) \pm \mathbf{1.5}(\text{syst})$ eV and $\boldsymbol{\Gamma_{2p}} = \mathbf{1.9 \pm 5.7}(\text{stat}) \pm \mathbf{0.7}(\text{syst})$ eV [24]. Both the shift and the width induced by the strong interaction are compatible with null values inside the error bars, in agreement with the theoretical models, which exclude the presence of a significant shift, and with the previous results obtained by SIDDHARTA 12). The new measurement of the kaonic helium $\boldsymbol{3d \to 2p}$ transition, compared to the value of the shift measured by SIDDHARTA $\boldsymbol{\varepsilon_{2p} = 0 \pm 6(}\text{stat}\boldsymbol{)} \pm \boldsymbol{2(}\text{syst}\boldsymbol{)}$ eV, exhibits an improvement in terms of resolution, with a statistical uncertainty six times less than the SIDDHARTA one.

5 Conclusions

The main goal of the SIDDHARTA-2 experiment at the DA**Φ**NE collider of INFN-LNF is to perform the first ever measurement of the shift and width induced by the strong interaction to the $\boldsymbol{1s}$ level of kaonic deuterium. This work displays the result of the characterization campaign of the SIDDHARTA-2 experimental setup. The run was realised using a gaseous helium-4 target operating at a density of **1.5%** of the liquid helium-4 density, which features an X-ray yield nearly 100 times higher than that expected from kaonic deuterium. A new measurement of the L-series lines of the kaonic helium-4 was performed to gauge the performance of the new apparatus. A total amount of $31\,\text{pb}^{-1}$ were collected. The analysis of the collected data yielded a shift and a width of the $\boldsymbol{2p}$ level of kaonic helium-4 of $\boldsymbol{\varepsilon_{2p}} = \mathbf{2.0} \pm \mathbf{1.2}(\text{stat}) \pm \mathbf{1.5}(\text{syst})$ eV and $\boldsymbol{\Gamma_{2p}} = \mathbf{1.9} \pm \mathbf{5.7}(\text{stat}) \pm \mathbf{0.7}(\text{syst})$ eV 24), thus excluding a large shift, in good agreement with the theoretical models and with the previous experimental results. The improved accuracy of the measurement of the shift with respect to the one done by the SIDDHARTA experiment 12) is a clear validation of the capability of the new apparatus to perform the challenging measurement of kaonic deuterium.

6 Acknowledgements

We thank H. Schneider, L. Stohwasser, and D. Pristauz-Telsnigg from Stefan Meyer-Institut for their fundamental contribution in designing and building the SIDDHARTA-2 setup. We thank as well the INFN, INFN-LNF and the DA**Φ**NE staff in particular to Dr. Catia Milardi for the excellent working conditions and permanent support. Catalina Curceanu acknowledge University of Adelaide, where part of this work was done (under the George Southgate fellowship, 2024). Part of this work was supported by the Austrian Science Fund (FWF): [P24756-N20 and P33037-N]; the Croatian Science Foundation under the project IP-2018–01-8570; the EU STRONG-2020 project (Grant Agreement No. 824093); the EU Horizon 2020 project under the MSCA (Grant Agreement 754496); the Japan Society for the Promotion of Science JSPS KAKENHI Grant No. JP18H05402; the SciMat and qLife Priority Research Areas budget under the program Excellence Initiative - Research University at the Jagiellonian University, and the Polish National Agency for Academic Exchange (Grant No. PPN/BIT/2021/1/00037); the EU Horizon 2020 research and innovation programme under project OPSVIO (Grant Agreement No. 101038099).

References

1. Sin-itiro Tomonaga and G. Araki, Phys. Rev. **58**, 90 (1940).
2. U-G Meißner, U. Raha and A. Rusetsky, Eur. Phys. J.-Part. Fields **35**, 349–357 (2004).
3. U-G Meißner, U. Raha and A. Rusetsky, Eur. Phys. J.-Part. Fields **47**, 473–480 (2006).
4. M. Mai, U-G Meißner, Nucl. Phys. A **900**, 51–64 (2013).
5. Z.H. Guo, J.A. Oller, Phys. Rev. C **87**, 035202 (2013).

6. Y. Ikeda, T. Hyodo, W. Weise, Nucl. Phys. A **881**, 98–114 (2012).
7. A. Cieply, E. Friedman, A. Gal, D. Gazda, J. Mares, Phys. Lett. B **702**, 402–407 (2011).
8. A. Cieply, E. Friedman, A. Gal, D. Gazda, J. Mares, J, Phys. Rev. C **84**, 045206 (2011).
9. Z.W. Liu, J.J. Wu, D.B. Leinweber, A.W. Thomas, Phys. Lett. B **808**, 135652 (2020).
10. J. Révai, Phys. Rev. C **94**, 054001 (2016).
11. M. Bazzi, G. Beer, L. Bombelli, A. Bragadireanu, M. Cargnelli, G. Corradi, C. Curceanu, C. Fiorini, T. Frizzi, F. Ghio *et al*, Phys. Lett. B, **704**, 113–117 (2011).
12. M. Bazzi, G. Beer, L. Bombelli, A. Bragadireanu, M. Cargnelli, G. Corradi, C. Curceanu, A. d'Uffizi, C. Fiorini, T. Frizzi *et al*, Phys. Lett. B, **681**, 310–314 (2009).
13. E. Gatti, P. Rehak, Nucl. Instrum. Methods Phys. Res. **225**, 608–614 (1984).
14. E. Gatti, P. Rehak, J.T. Walton, Nucl. Instrum. Methods A **226**, 129–141 (1984).
15. M. Miliucci, A. Scordo, D. Sirghi, A. Amirkhani, A. Baniahmad, M. Bazzi, D. Bosnar, M. Bragadireanu, M. Carminati, M. Cargnelli *et al*, Meas. Sci. Technol. **32**, 095501 (2021).
16. M. Miliucci, M. Iliescu, F. Sgaramella, M. Bazzi, D. Bosnar, M. Bragadireanu, M. Carminati, M. Cargnelli, A. Clozza, C. Curceanu *et al*, Meas. Sci. Technol. **33**, 095502 (2022).
17. F. Sgaramella, M. Miliucci, M. Bazzi, D. Bosnar, M. Bragadireanu, M. Carminati, M. Cargnelli, A. Clozza, G. Deda, L. De Paolis *et al*, Phys. Scr. **97**, 114002 (2022).
18. M. Skurzok, A. Khreptak, Bio-Algorithms Med-Syst. **19**, 74–79 (2023).
19. M. Bazzi, C. Berucci, C. Curceanu, A. d'Uffizi, M. Iliescu, E. Sbardella, A. Scordo, M. Shi, F. Sirghi, H. Tatsuno *et al*, J. Instrum. **8**, T11003 (2013).
20. M. Tüchler, C. Amsler, M. Bazzi, D. Bosnar, M. Bragadireanu, M. Cargnelli, A. Clozza, G. Deda, R.D. Grande, L.D. Paolis *et al*, J. Instrum. **18**, P11026 (2023).
21. M. Tüchler, J. Zmeskal, A. Amirkhani, M. Bazzi, G. Bellotti, C. Berucci, D. Bosnar, A. Bragadireanu, M. Cargnelli, C. Curceanu *et al*, In Proceedings of the 10th International Conference on Precision Physics of Simple Atomic Systems, Vienna, Austria, 14–18 May 2018; IOP Publishing: Bristol, UK, **1138**, 012012 (2018).
22. F. Sirghi, F. Sgaramella, L. Abbene, C. Amsler, M. Bazzi, G. Borghi, D. Bosnar, M. Bragadireanu, A. Buttacavoli, M. Carminati *et al*, arXiv:2311.16144 (2023)
23. M. Van Gysel, P. Lemberge, P. Van Espen, X-ray Spectrom. Int. J. **32**, 434–441 (2003)
24. F. Sgaramella, F. Clozza *et al*, Condens. Matter, **9**, 16 (2024).

Frascati Physics Series Vol. 76 (2024)
8TH YOUNG RESEARCHERS' WORKSHOP 'PHYSICS CHALLENGES IN THE LHC ERA'
May 13 and 16, 2024

Kaonic atoms studies with SIDDHARTA-2 at DAΦNE

Kairo Toho
Research Center for Accelerator and Radioisotope Science (RARiS), Tohoku University, Japan

L. Abbene[1], F. Artibani[1,14], M. Bazzi[1], G. Borghi[4,5], M. Bragadireanu[7], A. Buttacavoli[2], M. Cargnelli[3], M. Carminati[4,5], A. Clozza[1], F. Clozza[1], L. De Paolis[1], R. Del Grande[1,8], K. Dulski[1,11], C. Fiorini[4,5], I. Friščić[6], C. Guaraldo[1†], M. Iliescu[1], M. Iwasaki[9], A. Khreptak[10], S. Manti[1], J. Marton[3], P. Moskal[10,11], F. Napolitano[1], S. Niedzwiecki[10,11], H. Ohnishi[12], K. Piscicchia[13,1], F. Principato[2], A. Scordo[1], F. Sgaramella[1], M. Silarski[10], D. Sirghi[1,7,13], F. Sirghi[1,7], M. Shurzok[10,11], A. Spallone[1], L. Toscano[4,5] M. Tuechler[3], J. Zmeskal[3†] and Catalina Curceanu[1]

[1] Laboratori Nazionali di Frascati, INFN, Via E. Fermi 54, 00044 Frascati, Italy
[2] Dipartimento di Fisica e Chimica - Emilio Segrè, Università di Palermo, Viale Delle Scienze, Edificio 18, Palermo, 90128, Italy
[3] Stefan-Meyer-Institut für ubatomare Physik, Dominikanerbastei 16, Wien, 1010, Austria
[4] Politecnico di Milano - Dipartimento di Elettronica, Informazione e Bioingegneria, Via Giuseppe Ponzio 34, Milano, 20133, Italy
[5] INFN Sezione di Milano, Via Giovanni Celoria 16, Milano, 20133, Italy
[6] Department of Physics, Faculty of Science, University of Zagreb, Bijenička cesta 32, Zagreb, 10000, Croatia
[7] Horia Hulubei National Institute of Physics and Nuclear Engineering (IFIN-HH), No. 30, Reactorului Street, Magurele, Ilfov, 077125, Romania
[8] Physik Department E62, Technische Universität München, James-Franck-Straße 1, Garching, 85748, Germany
[9] Institute of Physical and Chemical Research, RIKEN, 2-1 Hirosawa, Wako, Saitama, 351-0198, Japan
[10] Faculty of Physics, Astronomy, and Applied Computer Science, Jagiellonian University, Łojasiewicza 11, Krakow, 30-348, Poland
[11] Centre for Theranostics, Jagiellonian University , Kopernika 40, Krakow, 31-501, Poland
[12] Research Center for Accelerator and Radioisotope Science (RARiS), Tohoku University, Japan
[13] Centro Ricerche Enrico Fermi - Museo Storico della Fisica e Centro Studi e Ricerche "Enrico Fermi", Via Panisperna 89A, Roma, 00184, Italy
[14] Università degli studi di Roma Tre, Dipartimento di Fisica, Roma, Italy
† Deceased

Abstract

The SIDDHARTA-2 experiment advances the study of kaonic atoms, focusing on kaonic deuterium and other kaonic atoms, such as neon, to explore low-energy Quantum Chromodynamics (QCD). Utilizing Silicon Drift Detectors and sophisticated veto systems, the experiment conducts high-precision X-ray spectroscopy to measure strong interaction-induced shifts and broadenings of atomic energy levels. This enables investigations of both electromagnetic and non-perturbative QCD effects, with high-n transitions facilitating precision tests of Quantum Electrodynamics (QED) and lower-level transitions providing insights into antikaon-nuclei strong interaction. Preliminary observations in kaonic neon highlight the potential for bridging theoretical predictions and experimental results.

1 Scientific case

The strong interaction, one of nature's four fundamental forces known so far, is crucial for understanding the structure and stability of matter. Governed by Quantum Chromodynamics (QCD), it explains quark-gluon interactions, which are the building blocks of protons, neutrons, and hadrons. Despite significant advances, the low-energy behavior of QCD remains poorly understood due to its non-perturbative nature, necessitating innovative experiments to provide data for refining theoretical models.

Kaonic atoms, which involve a negatively charged kaon bound to a nucleus via electromagnetic interaction, serve as a precise probe for low-energy QCD, particularly in the strangeness sector. These systems are significant for several reasons: they enable investigations of low-energy QCD in systems with non-zero strangeness quantum number, provide data to test QED predictions, and facilitate the determination of the charged kaon mass.

2 Kaonic atom formation

In kaonic atoms, a negatively charged kaon replaces one of the orbital electrons, allowing investigations into both the strong interaction and QED. A kaonic atom forms when a kaon, either slowed down or possessing sufficiently low initial momentum, is captured by an atom through electromagnetic interaction after being stopped in a target. This process leads to a highly excited state, with the excitation level dependent on the system's reduced mass; in kaonic hydrogen, this occurs at approximately $n \sim 25$ [1].

High-n energy transitions in kaonic atoms are primarily governed by electromagnetic interactions, with the strong interaction playing a negligible role. This enables the study of purely quantum electrodynamic (QED) effects, addressing fundamental issues such as the charged kaon mass puzzle [2]. By precisely measuring X-ray emissions from these transitions, one can compare observed results with purely QED-calculated values. Following capture, the kaonic atom begins to de-excite towards its fundamental state, emitting radiation in the X-ray domain as shown in Figure 1. However, the de-excitation process is influenced by the Stark effect and other competing mechanisms, particularly in higher-density environments, which significantly impact the yield of kaons fully de-exciting to the ground state.

Conversely, lower-level transitions in kaonic atoms provide critical insights into the non-perturbative regime of QCD. These transitions reflect the complex interplay of the strong interaction between the kaon and the nucleus, inducing an energy shift in the transition to the fundamental 1s level that deviates from the canonical electromagnetic value, $E^{em}_{2p\rightarrow 1s}$. This reveals the isospin-dependent antikaon-nucleon scattering lengths, which are fundamental for understanding low-energy QCD in the strangeness sector [3]. Thus, kaonic atoms serve as an invaluable tool for advancing our understanding of both electromagnetic and hadronic physics, bridging the gap between QED and non-perturbative QCD.

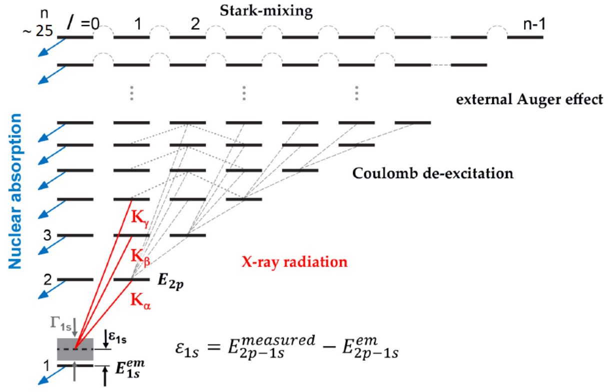

Figure 1: A schematic overview of the de-excitations which take place during the formation of the kaonic atoms. The kaons are captured in a highly excited state and cascade down to the fundamental level. The last transitions are influenced by the strong interaction, leading to a broadening and shift of the 1s level with respect to the case of only electromagnetic interaction. Reproduced from [4].

3 SIDDHARTA-2 Experiment

The SIDDHARTA-2 experiment aims to perform high-precision X-ray spectroscopy of kaonic atoms. Its primary goal is to measure the strong interaction-induced shift and width of the fundamental level in kaonic deuterium. Building on the earlier SIDDHARTA project on kaonic hydrogen, it exploits a new generation of Silicon Drift Detectors [5] [6] and three veto systems to tackle challenges of lower X-ray yield and wider 1s level width, or kaonic deuterium measurement.

The SIDDHARTA-2 setup is shown in Figure 2, installed above the DAΦNE interaction point in 2022. It was developed for high-precision spectroscopy in a high-radiation environment, handling both electromagnetic and hadronic background noise. Electromagnetic background from beam loss particles are reduced through time information from the Kaon Trigger and Silicon Drift Detectors (SDDs), while hadronic background is suppressed using sophisticated veto systems. The apparatus features a cylindrical beam pipe, a high-vacuum system, and a cryogenic target cell surrounded by 384 SDDs and multiple veto systems, with additional detection systems such as the Kaon Trigger [7] and Luminosity Monitor [8].

The Kaon Trigger, with plastic scintillators and Photomultiplier Tubes (PMTs), detects K^+K^- pairs and minimizes accidental triggers. The Luminosity Monitor assesses beam quality using similar scintillator technology. The cryogenic target cell, cooled to 20 K, and the SDDs, cooled to 140 K, optimize kaon stopping efficiency. The setup also includes Veto-1, an outer barrel of plastic scintillators, that reduces kaon backgrounds, while Veto-2 [9], composed of plastic scintillators tiles and Silicon Photomultipliers (SiPMs), addresses background from Minimum Ionising Particles (MIPs).

Calibration is done with two X-ray tubes (Jupiter 5000 Series, 50kV), installed on opposite sides of the vacuum chamber, and titanium-copper foils mounted on the target cell. The X-ray tubes excite fluorescence in these elements, producing characteristic Ti Kα and Cu Kα lines, which are used to calibrate the SDDs. The calibration peaks are fitted using Gaussian and tail functions to enhance accuracy, achieving a precision of 2.0 ± 0.1 eV when compared to the Fe Kα reference value, ensuring the stability required for kaonic deuterium measurements [10].

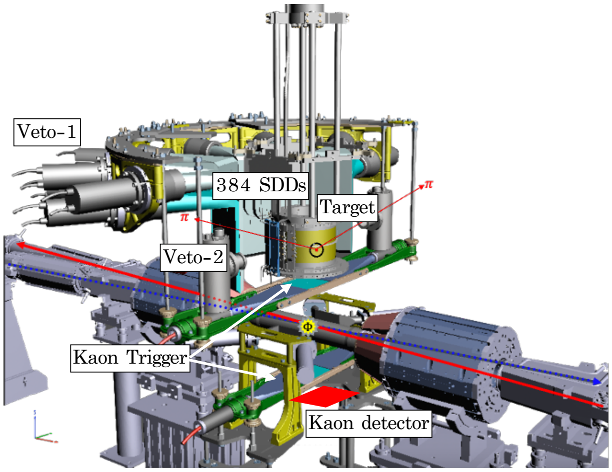

Figure 2: The schematic layout of the SIDDHARTA-2 experimental apparatus is presented, highlighting the main elements integral to the experiment.

4 Energy calibration of the Silicon Drift Detectors

The energy response function of an SDD detector for fluorescence X-ray signals is primarily characterized by a Gaussian function. However, a low-energy component exists due to incomplete charge collection and the electron-hole recombination effect. Consequently, the total peak fitting function is composed of two components:

- Gaussian function: This is the main contributor to the peak shape, with the peak width (σ) described by a function of the Fano Factor (FF), electron-hole pair creation energy (ε), and both electronic and thermal noise($noise$).
  The Gaussian function is expressed as:
  $$G(E) = \frac{A_G}{\sqrt{2\pi}\sigma} \cdot e^{\frac{-(E-E_0)^2}{2\sigma^2}}, \sigma = \sqrt{FF \cdot \epsilon \cdot E + \frac{noise^2}{2.35^2}} \tag{1}$$
- Tail function: An exponential function accounts for incomplete charge collection, expressed as:
  $$T(E) = \frac{A_T}{2\beta\sigma} \cdot e^{\frac{E-E_0}{\beta\sigma} + \frac{1}{2\beta^2}} \cdot erfc(\frac{E-E_0}{\sqrt{2}\sigma} + \frac{1}{\sqrt{2}\beta}) \tag{2}$$

In these equations, A_G and A_T represent the amplitudes of the Gaussian and tail functions, respectively. The parameter β is the slope of the tail, and erfc is the complementary error function. Figure 3 shows a typical energy spectrum obtained from a single SDD in a calibration run. For this analysis, the energy range was selected from 4 keV to 15 keV, encompassing the region of interest (ROI) for SIDDHARTA-2. For each target element, both the K_α and K_β transitions are clearly observed. The fitting function consists of a convolution of a Gaussian and a tail functions for each fluorescence line, while the background is modeled by a combination of a first-degree polynomial and an exponential function. The fitting process was conducted using MINUIT [12], with MIGRAD minimization yielding in this case a reduced chi-square value of 1.18, confirming the overall fit accuracy.

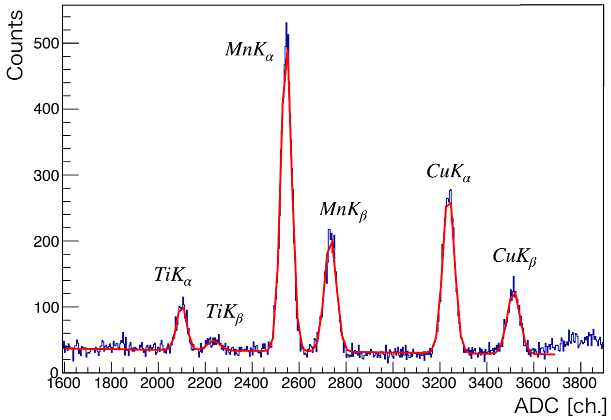

Figure 3: A typical Silicon Drift Detector energy spectrum acquired during a calibration run, in arbitrary ADC units, displays fluorescence emission lines from a multi-element target activated by an X-ray tube.

The K_α lines were selected to investigate the energy response of the SDDs due to their higher signal-to-noise ratio compared to the K_β lines. The energy response of the SDDs is described by a linear function based on the Analog-to-Digital Converter (ADC) response:

$$E = m \cdot ADC(ch.) + q \tag{3}$$

where m is the gain of the detector in eV/ch. Figure 4 illustrates the calibration function for the SDD spectrum in Figure 3. The calibration points are determined by the theoretical energy values of each line and their corresponding measured values in arbitrary ADC units.

The calibration accuracy and validity of the linearity assumption were assessed by calculating the residuals, defined as the difference between each calibrated point E_{meas} and its theoretical value E_{th} [13]:

$$\Delta E = E_{meas} - E_{th} \tag{4}$$

This analysis was applied to all 384 SDDs used in the SIDDHARTA-2 experiment. Figure 5 provides an example of the residuals plot for four SDDs. The residuals are centered around zero, with deviations of no more than 3 eV from the ideal linear case, indicating a linear response ($\Delta E/E$) with an accuracy better than 10^{-3}.

5 Kaonic neon observation: preliminary result

In the spring of 2023, prior to the kaonic deuterium measurement, a kaonic neon measurement was performed as part of the SIDDHARTA-2 optimization phase, with the objective of calibrating and refining the detectors' energy response. The target cell of the setup was filled with neon gas at a density equivalent to 0.36% of the liquid neon density (LNeD), and a total of 125 pb^{-1} of data was collected.

The calibration procedure previously described was applied to obtain the energy spectrum shown in Figure 6 corresponding to about 32 pb^{-1}. Five kaonic neon transitions were observed; these high-n transitions are not influenced by the strong kaon-nucleus interaction. Data analysis is ongoing towards a dedicated publication. This characteristic renders them particularly valuable for precision QED tests, as for determining the mass of charged kaons and exploring de-excitation mechanisms in kaonic atoms which are ongoing within the collaboration.

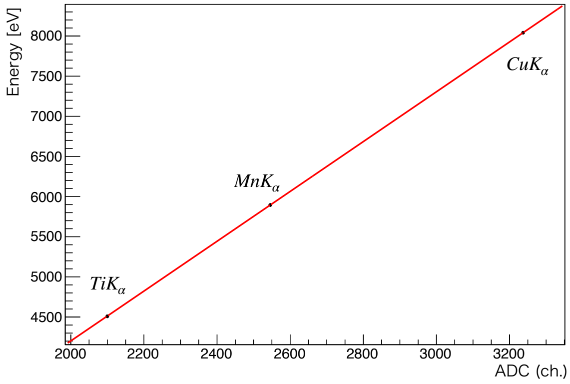

Figure 4: The linear calibration function translates ADC values to energy for the analyzed Silicon Drift Detector (SDD).

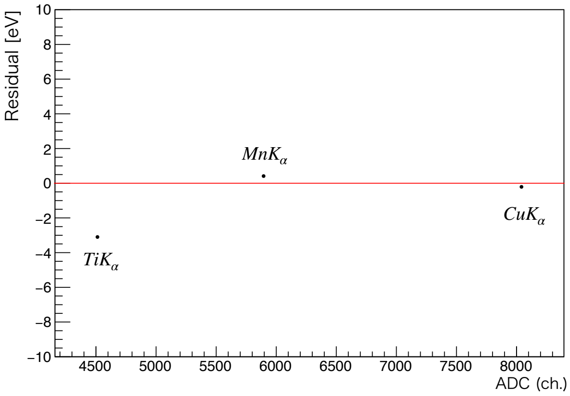

Figure 5: Residuals plot for a single SDD.

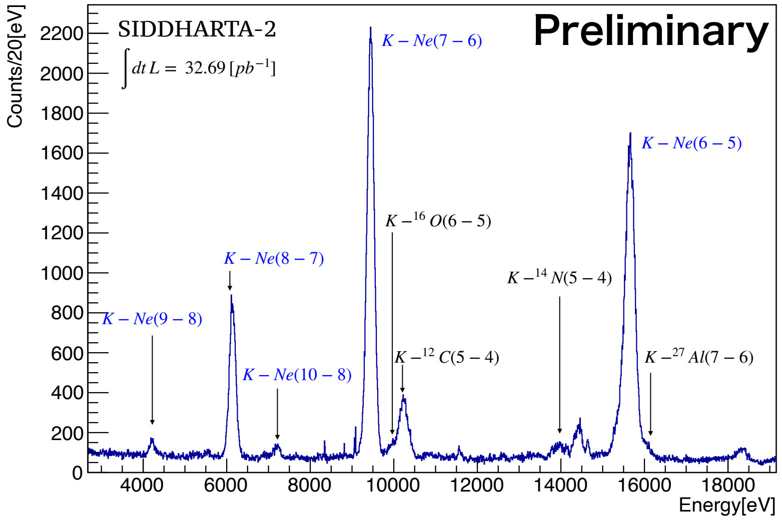

Figure 6: Preliminary kaonic neon energy spectrum, displaying lines for kaonic neon (K-Ne), carbon (K-C), nitrogen (K-N), oxygen (K-O), and aluminium (K-Al). Transitions are identified by the initial (n_i) and final (n_f) principal quantum numbers of the corresponding atomic levels.

6 Conclusions

The SIDDHARTA-2 experiment represents a significant advancement in the study of kaonic atoms, particularly in its efforts to probe the low-energy regime of Quantum Chromodynamics (QCD) and enhance our understanding of fundamental interactions.

The formation of kaonic atoms facilitates unique investigations into both electromagnetic and non-perturbative QCD effects. High-n energy transitions in kaonic systems serve as a platform for precision tests of Quantum Electrodynamics (QED), while lower-level transitions reveal vital information about the strong interaction and its influence on atomic energy levels.

The successful implementation of advanced detection systems, including Silicon Drift Detectors and sophisticated veto mechanisms, has significantly improved the accuracy and efficiency of measurements in a challenging experimental environment. Preliminary observations, such as those in kaonic neon, underline the potential of these systems also for precision QED studies, thereby bridging the gap between theoretical predictions and experimental realities.

Through ongoing research and data analysis, the SIDDHARTA-2 collaboration aims to refine our understanding of the strong interaction and its manifestations in exotic atomic systems. This endeavor not only contributes to the fundamental physics landscape but also opens avenues for future explorations in hadronic physics.

7 Acknowledgements

We thank C. Capoccia from LNF-INFN and H. Schneider, L. Stohwasser, and D. Pristauz-Telsnigg from Stefan Meyer-Institut for their fundamental contribution in designing and building the SIDDHARTA-2 setup. We thank as well the DAΦNE staff for the excellent working conditions and permanent support. Part of this work was supported by the EU STRONG-2020 project (Grant Agreement No. 824093). The authors acknowledge support from the SciMat and qLife Priority Research Areas budget under the program Excellence Initiative—Research University at the Jagiellonian University.

References

1. F. Napolitano *et al.* Phys. Scr. 97 (2022) 084006
2. Bosnar D, Bazzi M, Cargnelli M, Clozza A, Curceanu C, Del Grande R, et al. Revisiting the charged kaon mass. Acta Phys Polon B (2020) 51:115. doi:10.5506/ aphyspolb.51.115
3. Curceanu C et al. 2020 Symmetry 12 ISSN 2073-8994
4. F Napolitano et al 2022 Phys. Scr. 97 084006
5. M. Bazzi *et al.* Condens. Matter 2021, 6(4), 47
6. F. Sgaramella *et al.* 2022 Phys. Scr. 97 114002
7. F. Sirghi *et al.* arXiv:2311.16144 [physics.ins-det]
8. M. Skurzok *et al.* 2020 JINST 15 P10010
9. M. Tüchler et al 2023 JINST 18 P11026
10. F. Sgaramella *et al.* Volume 59, article number 56, (2023)
11. Zyla, P. A. et al. Review of Particle Physics. PTEP 2020, 083C01 (2020).
12. James, F. MINUIT Function Minimization and Error Analysis: Reference Manual Version 94.1 (1994).
13. Vaughan, D. X-ray data booklet. center for x-ray optics. [tables] (1985). URL https://www.osti.gov/biblio/6359890.